Direct and Indirect Imaging of α-synuclein Pathology Using Positron Emission Tomography and Functional Magnetic Resonance Imaging

Dissertation

der Mathematisch-Naturwissenschaftlichen Fakultät

der Eberhard Karls Universität Tübingen

zur Erlangung des Grades eines

Doktors der Naturwissenschaften

(Dr. rer. nat.)

vorgelegt von

Laura Kübler

Stuttgart

Tübingen

2023

Gedruckt mit Genehmigung der Mathematisch-Naturwissenschaftlichen Fakultät der Eberhard Karls Universität Tübingen.

Tag der mündlichen Qualifikation:	11.04.2024
Dekan:	Prof. Dr. Thilo Stehle
1. Berichterstatter/-in:	Prof. Dr. Kristina Herfert
2. Berichterstatter/-in:	Prof. Dr. Steffen Hage

Summary

Neuroimaging is a valuable tool to investigate the brain in a healthy and diseased state. Imaging techniques such as positron emission tomography (PET) and magnetic resonance imaging (MRI) make it possible to structurally visualize the brain and display the brain in action on a molecular and functional level. Functional MRI (fMRI) detects neuronal activity via the hemodynamic response at rest, during a task, or after a pharmacological stimulation. The picomolar sensitivity of PET enables imaging of the distribution of various molecular targets and related biological processes in the brain. The combination of pharmacological MRI and PET offers excellent potential to investigate brain network modulations of different neurotransmitter systems and provides information on molecular neurotransmitter-receptor interactions *in vivo*. Both imaging modalities may provide a deeper insight into the coupling of molecular and macroscopic neural mechanisms underlying specific processes in the healthy and the diseased brain.

This work focuses on imaging synucleinopathies, a group of heterogeneous neurodegenerative diseases characterized by the pathological aggregation of the protein α-synuclein (αSYN) in different cells and regions in the brain. Relevant biomarkers of αSYN aggregation are still missing in the field of neuroimaging. Therefore, there is an unmet need to develop a novel PET tracer to detect αSYN aggregates for diagnosis and therapy control and to develop a multimodal imaging approach to link protein aggregation to functional neuronal changes.

The first part of this work aimed to investigate different chemical derivatives of anle138b, a compound that has been shown to have therapeutic activity in animal models of neurodegenerative diseases, towards their binding affinities to recombinant αSYN fibrils to develop a specific αSYN PET tracer. One compound, MODAG-001, showed a very high affinity towards human recombinant αSYN fibrils. Furthermore, binding selectivity over Aβ in human and mouse Alzheimer's disease (AD) tissue and the binding specificity in human synucleinopathies with αSYN pathology were determined. [^{3}H]MODAG-001 showed specific binding to Aβ-pathology. However, this was between 5- and 14-fold lower compared to the gold standard AD marker, Pittsburgh Compound B. Using [^{3}H]MODAG-001 in autoradiography experiments on human brain sections of different proteinopathies revealed binding of [^{3}H]MODAG-001 in cortical areas of PD and AD brain tissue, with a weak signal to noise ratio. *In vivo* evaluation of [^{11}C]MODAG-001 revealed good pharmacokinetics of the PET tracer with a fast washout of the brain and

one metabolite with 90% of [^{11}C]MODAG-001 present in the brain at 15 minutes after tracer injection. *In vivo*, evaluation of [^{11}C]MODAG-001 in a mouse model of Parkinson's disease showed no specific binding in brain areas with high αSYN pathology. The metabolite observed in the [^{11}C]MODAG-001 metabolite analysis was the demethylated precursor MODAG-005, which was then tritiated for further specificity experiments in human brain sections of different proteinopathies. Autoradiography experiments revealed binding of [^{3}H]MODAG-005 in cortical areas of PD and AD brain tissue.

The second part of this thesis aimed to develop a simultaneous PET/fMRI approach in rats to correlate changes in dopamine availability and presynaptic dysfunction to whole-brain functional changes. For this purpose [^{11}C]raclopride, a widely used PET tracer to measure striatal changes in dopamine release, in combination with BOLD-fMRI, was used in a rat model overexpressing the protein αSYN in the caudate putamen of one brain hemisphere. The reproducibility and reliability of both measures were first evaluated using test-retest experiments in healthy rats. The variability within and between [^{11}C]raclopride-PET scans and the reliability within and between fMRI scans were determined. Between scan variability of [^{11}C]raclopride was 20.8 ± 14.2% at end of the acquisition (time interval T_5 (86-95 minutes)) compared to the baseline, while within scan variability was 11.4 ± 17.1 %. Reliability between fMRI scans was moderate (r = 0.5 ± 0.1), but the correlation within fMRI scans was good (r = 0.7 ± 0.1). In the next step, the [^{11}C]raclopride-PET/fMRI approach was used to investigate alterations in dopamine neurotransmission and its impact on functional connectivity in healthy rats and a rat model of αSYN overexpression by applying *d*-amphetamine as pharmacological stimulation. This study aimed to investigate the modulation of dopamine dynamics since it is involved in several vital central nervous functions such as movement, reward, sleep, attention, and learning. Furthermore, dopamine depletion in the nigrostriatal pathway is a hallmark of Parkinson's disease, which has been reported to be involved in the impaired modulation of frontal cortical activity. Therefore, functional connectivity changes in the dopaminergic network and the default-mode network were assessed after *d*-amphetamine stimulation to delineate the effect of alterations of dopamine release on brain circuitry. Amphetamine-induced dopamine release decreased [^{11}C]raclopride binding in the caudate putamen, as well as functional connectivity in the dopaminergic network and the default-mode network affecting particular frontal cortical regions in healthy rats. Nigrostriatal dopamine depletion increased [^{11}C]raclopride binding in the αSYN overexpressing caudate putamen. Using standard quantification methods with the cerebellum as a reference region, we did not

observe any dopamine release in the αSYN overexpressing caudate putamen after *d*-amphetamine stimulation. Other quantification approaches, independent of a reference region, are currently being tested to determine extrasynaptic dopamine fluctuations. *D*-amphetamine-induced functional connectivity response was decreased after the unilateral nigrostriatal dopamine depletion in both hemispheres.

In summary, the present dissertation provided preliminary evidence that MODAG-001 and its metabolite MODAG-005 are promising lead structures for the future development of a potential PET tracer targeting αSYN aggregation. However, its non-specific binding must be reduced to achieve a higher signal-to-noise ratio in human brain tissue with αSYN pathology. Since no PET tracer is still available for imaging αSYN aggregation, other approaches, such as multimodal imaging to detect pre- and postsynaptic dysfunctions, are very valuable linking molecular changes caused by the aggregation of αSYN to neuronal functional changes. The presented work demonstrated a relationship between dopamine depletion and a decreased frontal cortical response after amphetamine-induced dopamine release using a simultaneous [^{11}C]raclopride-PET/fMRI approach in a rat model of αSYN overexpression.

Zusammenfassung

Die Neurobildgebung ist ein wertvolles Instrument zur Untersuchung des Gehirns in gesundem und krankem Zustand. Bildgebende Verfahren wie die Positronenemissionstomographie (PET) und die Magnetresonanztomographie (MRT) ermöglichen es, das Gehirn nicht nur strukturell zu visualisieren, sondern auch auf molekularer und funktioneller Ebene in Aktion zu zeigen. Die funktionelle MRT (fMRI) erfasst die neuronale Aktivität über die hämodynamische Reaktion in Ruhe, während einer Aufgabe oder nach einer pharmakologischen Stimulation. Die pikomolare Empfindlichkeit der PET ermöglicht die Darstellung der Verteilung verschiedener molekularer Ziele wie Rezeptoren und damit verbundener biologischer Prozesse im Gehirn. Die Kombination von pharmakologischer MRT und PET bietet das große Potenzial, Modulationen von Gehirnnetzwerken verschiedener Neurotransmittersysteme zu untersuchen und liefert Informationen über molekulare Neurotransmitter-Rezeptor-Interaktionen *in vivo*. Beide Bildgebungsmethoden können einen tieferen Einblick in die Kopplung von molekularen und makroskopischen neuronalen Mechanismen geben, die bestimmten Prozessen im gesunden wie auch im kranken Gehirn zugrunde liegen.

Diese Arbeit konzentriert sich auf die Bildgebung von Synucleinopathien, einer Gruppe heterogener neurodegenerativer Erkrankungen, die durch die pathologische Aggregation des Proteins α-Synuclein (αSYN) in verschiedenen Zellen und Regionen des Gehirns charakterisiert sind. Auf dem Gebiet der Neurobildgebung gibt es nach wie vor keine relevante Biomarker für die αSYN-Aggregation. Daher besteht ein Bedarf an der Entwicklung eines neuartigen PET-Tracers zum Nachweis von αSYN-Aggregaten für die Diagnose und Therapiekontrolle, sowie an der Entwicklung eines multimodalen Bildgebungsansatzes zur Verknüpfung der Proteinaggregation mit funktionellen neuronalen Veränderungen.

Das Ziel des ersten Teiles dieser Arbeit war es, verschiedene chemische Derivate von anle138b, einer Verbindung, die sich in Tiermodellen für neurodegenerative Erkrankungen als therapeutisch wirksam erwiesen hat, auf ihre Bindungsaffinität zu rekombinanten αSYN-Fibrillen zu untersuchen, um einen spezifischen αSYN PET-Tracer zu entwickeln. Eine Verbindung, MODAG-001, zeigte eine sehr hohe Affinität zu menschlichen rekombinanten αSYN-Fibrillen. Darüber hinaus wurde die Bindungsselektivität gegenüber Amyloid-β im Gewebe von Menschen und Mäusen mit der Alzheimer-Krankheit und die Bindungsspezifität bei menschlichen Proteinopathien mit αSYN-Pathologie bestimmt.

[^{3}H]MODAG-001 zeigte eine spezifische Bindung an Amyloid-β-Pathologie. Diese war jedoch 5 bis 14-mal schwacher als der Goldstandard Alzheimer Marker, Pittsburgh Compound B. Die Verwendung von [^{3}H]MODAG-001 in Autoradiographie-Experimenten an menschlichen Hirngewebe verschiedener Proteinopathien ergab eine Bindung von [^{3}H]MODAG-001 in kortikalen Bereichen von Parkinson und Alzheimer-Gehirngewebe mit einem schwachen Signal-Rausch-Verhältnis. Die *in vivo* Untersuchung von [^{11}C]MODAG-001 ergab eine gute Pharmakokinetik des PET-Tracers mit einer schnellen Ausschwemmung aus dem Gehirn und einem Metaboliten, der 15 Minuten nach der Traceinjektion zu 90 % im Gehirn vorhanden war. In einem Mausmodell der Parkinson-Krankheit zeigte [^{11}C]MODAG-001 keine spezifische Bindung in Hirnbereichen mit hoher αSYN-Pathologie. Bei der Metabolitenanalyse von [^{11}C]MODAG-001 wurde ein Metabolit gefunden, bei welchem es sich um den demethylierten Precursor MODAG-005 handelt. Dieser wurde dann tritiert und für weitere Experimente zur Untersuchung der Spezifität in menschlichem Hirngewebe verschiedener Proteinopathien getestet. Autoradiographie-Experimente ergaben eine Bindung von [^{3}H]MODAG-005 in kortikalen Bereichen von Parkinson und Alzheimer Gehirngewebe.

Der zweite Teil dieser Arbeit zielte darauf ab, einen simultanen PET/fMRI-Ansatz in Ratten zu entwickeln, um Veränderungen der Dopaminkonzentration und der präsynaptischen Dysfunktion mit funktionellen Veränderungen im gesamten Gehirn zu korrelieren. Zu diesem Zweck wurde [^{11}C]Racloprid, ein weit verbreiteter PET-Tracer zur Messung striataler Veränderungen der Dopaminfreisetzung, in Kombination mit BOLD-fMRI in einem Rattenmodell verwendet, welches das Protein αSYN im Caudate Putamen einer Gehirnhälfte überexprimiert. Reproduzierbarkeit und Zuverlässigkeit beider Messungen wurden zunächst anhand von Test-Retest-Experimenten an gesunden Ratten getestet. Die Variabilität innerhalb und zwischen [^{11}C]Racloprid-PET-Scans und die Zuverlässigkeit innerhalb und zwischen fMRI-Scans wurden bestimmt. Die Variabilität zwischen den Scans von [^{11}C]Racloprid betrug 20,8 ± 14,2 % am Ende der Akquisition (Zeitintervall T_5 (86-95 Minuten)) im Vergleich zum Ausgangswert, während die Variabilität innerhalb der Scans 11,4 ± 17,1 % betrug. Die Reliabilität zwischen den fMRI-Scans war mäßig ($r = 0,5 \pm 0,1$), aber die Korrelation innerhalb der fMRI-Scans war gut ($r = 0,7 \pm 0,1$). In einem nächsten Schritt wurde der [^{11}C]Racloprid-PET/fMRT-Ansatz verwendet, um Veränderungen der Dopamin-Neurotransmission und ihre Auswirkungen auf die funktionelle Konnektivität bei gesunden Ratten und einem Rattenmodell mit αSYN-Überexpression zu untersuchen, indem *d*-Amphetamin als pharmakologische Stimulation eingesetzt

wurde. Ziel dieser Studie war es, die Modulation der Dopamindynamik zu untersuchen, da Dopamin an mehreren lebenswichtigen Funktionen des Zentralnervensystems wie Bewegung, Belohnung, Schlaf, Aufmerksamkeit und Lernen beteiligt ist. Darüber hinaus ist die Dopaminverarmung im nigrostriatalen Signalweg ein Kennzeichen der Parkinson-Krankheit, von der berichtet wurde, dass sie an der gestörten Modulation der frontalen kortikalen Aktivität beteiligt ist. Daher wurden die Veränderungen der funktionellen Konnektivität im dopaminergischen Netzwerk und im Default-Mode-Netzwerk nach *d*-Amphetamin Stimulation untersucht, um die Auswirkungen von Veränderungen der Dopaminfreisetzung auf die Schaltkreise des Gehirns zu beschreiben. Die *d*-Amphetamin-induzierte Dopaminfreisetzung verringerte die [^{11}C]Racloprid-Bindung im Caudate Putamen, sowie die funktionelle Konnektivität im dopaminergen Netzwerk und im Default-Mode-Netzwerk, insbesondere die frontalen kortikalen Regionen bei gesunden Ratten. Der Mangel an nigrostriatalem Dopamin führte zu einem Anstieg der [^{11}C]Rcloprid-Bindung im αSYN-überexprimierenden Caudate Putamen. Unter Verwendung von Standard-Quantifizierungsmethoden mit dem Cerebellum als Referenzregion konnten wir keine Dopaminfreisetzung im αSYN-überexprimierenden Caudate Putamen nach der *d*-Amphetamin Stimulation beobachten. Andere Quantifizierungsmethoden, die unabhängig von einer Referenzregion sind, werden derzeit getestet, um extrasynaptische Dopaminfreisetzungen zu bestimmen. Die durch *d*-Amphetamin induzierte Reaktion auf die funktionelle Konnektivität war nach einseitigem nigrostriatalem Dopaminmangel in beiden Hemisphären vermindert.

Zusammenfassend lässt sich sagen, dass die vorliegende Dissertation erste Hinweise liefert, dass MODAG-001 und sein Metabolit MODAG-005 vielversprechende Leitstrukturen für die künftige Entwicklung eines potenziellen αSYN PET-Tracers sind. Allerdings muss die unspezifische Bindung reduziert werden, um ein höheres Signal-Rausch-Verhältnis in menschlichem Hirngewebe mit αSYN-Pathologie zu erreichen. Da es noch keinen PET-Tracer für die Bildgebung der αSYN-Aggregation gibt, sind andere Ansätze wie die multimodale Bildgebung zum Nachweis von prä- und postsynaptischen Dysfunktionen sehr wertvoll, um die durch die αSYN-Aggregation verursachten molekularen Veränderungen mit neuronalen Funktionsänderungen zu verknüpfen. In der vorgestellten Arbeit wurde ein Zusammenhang zwischen Dopaminmangel und einer verringerten frontalen kortikalen Reaktion nach *d*-Amphetamin-induzierter Dopaminfreisetzung mit Hilfe eines simultanen [^{11}C]Racloprid-PET/fMRT-Ansatzes in einem Rattenmodell mit αSYN-Überexpression nachgewiesen.

Contents

List of Figures

List of Tables

Abbreviations

AAV	Adeno-associated virus
Aβ	Abeta
AD	Alzheimer's diseases
ADHD	Attention deficit hyperactivity disorder
AFNI	Analysis of functional neuro images
Amyg	Amygdala
αSYN	α-synuclein
ATP	Adenosine triphosphate
BBB	Blood-brain barrier
BOLD	Blood oxygen level-dependent
BP_{ND}	Binding potential non-displaceable
BSA	Bovine serum albumin
CA1	Anterodorsal hippocampus
cAMP	Cyclic adenosine monophosphate
Cer	Cerebellum
Cg	Cingulate Cortex
CNS	Central nervous system
CPu	Caudate Putamen
[^{11}C]RAC	[^{11}C]Raclopride
CT	Computed tomography
D-AMPH	*D*-amphetamine
DVR	Distribution volume ratio
EPI	Echo-planar imaging
[^{18}F]FDG	[^{18}F]Fluordeoxyglucose
FID	Free induction decay

fMRI	Functional magnetic resonance imaging
FOV	Field of view
FWHM	Full-width-half-maximum
GABA	Gamma-aminobutyric acid
GCI	Glial cytoplasmic inclusion
GFP	Green fluorescent protein
GPe	Globus pallidus external
GPi	Globus pallidus internal
GPCR	G protein-coupled receptors
HPLC	High-performance liquid chromatography
Hyp	Hypothalamus
ICC	Intraclass correlation coefficient
LB	Lewy body
LBD	Dementia with Lewy bodies
L-DOPA	L-dihydroxyphenylalanine
LN	Lewy neurite
LOR	Line of response
MarsBaR	MARseille Boite À Région d'Intéret
MB	Midbrain
MDMA	3,4-methylenedioxymethamphetamine
mPFC	Medial prefrontal cortex
MRI	Magnetic resonance imaging
MSA	Multiple system atrophy
NAc	Nucleus Accumbens
Nifti	Neuroinformatics technology initiative
OFC	Orbitofrontal cortex

6-OHDA	6-Hydroxydopamine
OSEM	Ordered subsets expectation-maximization
PaC	Parietal cortex
PD	Parkinson’s disease
PDD	Parkinson’s disease dementia
PET	Positron emission tomography
phMRI	Pharmacological magnet resonance imaging
PIB	Pittsburgh Compound B
PSP	Progressive supranuclear palsy
RF	Radiofrequency
ROI	Region of interest
RS	Retrosplenial Cortex
SNARE	N-ethylmaleeimide sensitive factor attachment protein receptor
SNc	Substantia nigra pars compacta
SNr	Substantia nigra pars reticulata
SPM	Statistical parametric mapping
SRTM	Simplified reference tissue model
STN	Subthalamic nucleus
SUV	Standard uptake value
SUVR	Standard uptake value ratio
TAC	Time activity curve
TE	Echo time
TR	Repetition time
VTA	Ventral tegmental area

1 Introduction

The brain and its complexity have been the research focus for many decades. It is the body's central control system responsible for motor control, thought processing, behavior, and memory formation, to name only a few functions (1).

One of the motor control and voluntary movement circuits is the basal ganglia circuit. The *substantia nigra pars compacta* is connected with the caudate putamen via dopaminergic neurons synthesizing and releasing the neurotransmitter dopamine. The dopaminergic system is the most extensively studied neurotransmitter system of the brain, and its dysfunction is involved in different neurodegenerative diseases, including Parkinson's disease (PD) (2). The progressive loss of dopaminergic neurons arising from the s*ubstantia nigra pars compacta* and small intracytoplasmatic inclusions in different cell types, known as Lewy bodies (LB), are characteristics of PD. The misfolded protein α-synuclein (αSYN) is the main component of LBs, and ascending evidence suggests that αSYN aggregation is a possible perpetrator of synaptic dysfunction and dopaminergic neurodegeneration in PD (3). Aggregation of αSYN is also involved in other neurodegenerative diseases such as multiple system atrophy (MSA) and dementia with Lewy bodies (LBD) (4). However, pathogenically relevant biomarkers of αSYN aggregation are still missing.

Noninvasive imaging technologies such as magnetic resonance imaging (MRI) and positron emission tomography (PET) are promising tools for an early diagnosis, monitoring of disease progression, and evaluation of disease-modifying therapies. However, despite intensive research, PET tracers to detect pathologically aggregated αSYN are still unavailable.

The following introduction will give an overview of the brain's functions, including the basal ganglia circuits, the dopaminergic system, and the synaptic neurotransmission, as well as a description of the involvement of αSYN in the different proteinopathies. Furthermore, it will describe direct and indirect imaging methods used to detect αSYN aggregation in this work. The characteristics of an ideal central nervous system PET tracer are discussed, including its challenges.

1.1 Functions of the Brain

The brain is the most complex organ in the human body, and it is the control center of many different functions, such as voluntary movements and involuntary activities like breathing and heartbeat. Furthermore, it allows us to feel emotions, to treasure memories, and makes us who we are. To perform all these functions, various chemical reactions are ongoing simultaneously, demanding an excessive amount of energy compared to the brain's weight. In short, through its complexity, the brain keeps us alive (1).

The brain consists of approximately 10^{11} neurons, which are the basic units of the brain. These neurons can be classified into thousands of various types which are then organized into circuits with precise functions. Neurons consist of four morphologically different regions: (i) a cell body being the metabolic center and containing the genetic information, (ii) dendrites receiving incoming signals from other nerve cells, (iii) an axon carrying electrical signals, called action potentials, to the (iv) presynaptic terminals, which then transmit signals to the postsynaptic cell. The pre- and postsynaptic terminals are separated by a narrow gap called synaptic cleft (1).

The brain uses the action potentials to receive, analyze, and convey information. An incoming action potential at the presynapse leads to the release of a neurotransmitter into the synaptic cleft. The released neurotransmitter binds to receptors on the postsynaptic membrane, regulating ion channels or intracellular signaling in the postsynaptic cell. This can lead to firing or exhibiting an action potential (1).

The following subchapters introduce the basal ganglia circuits, which are responsible for motor, cognitive, and limbic functions in the brain. Further, the focus lies on the dopaminergic system and its neurotransmission. Last, the onset of different proteinoopathies is discussed.

1.1.1 Basal Ganglia Circuits

The basal ganglia are a network consisting of mainly four different nuclei for each cerebral hemisphere, including the caudate (caudate nucleus and putamen), also called striatum, the *globus pallidus* (GP, *internal* (i) and *external* (e)), the *subthalamic nucleus* (STN) and the *substantia nigra* (SN, *pars reticulata* (r) and *pars compacta* (c)). It receives input from the cortex and communicates via the thalamus to the cortex and the brainstem. The basal ganglia are involved in motor control, planning, learning, cognition, and emotions. Depending on the movement, the basal ganglia can choose different pathways

(direct and indirect) to initiate and terminate the movement using the excitatory neurotransmitter glutamate and the inhibitory neurotransmitter gamma-aminobutyric acid (GABA) (5).

The direct pathway leads to the excitation of the motor cortex, thereby promoting motor activity. Therefore, the cortex projects via excitatory neurons to the caudate (caudate nucleus and putamen). Inhibitory neurons of the caudate rise to the *GPi* and the *SNr*. Since both *GPi* and *SNr* send inhibitory input to the thalamus, their inhibition leads to disinhibition of the thalamus, which sends excitatory projections to the motor cortex (6) (Figure 1 a).

The indirect pathway causes a decrease in the activity of the cortical motor neurons, leading to a suppression of unprepared movement. From the cortex via the striatum, neurons project to the *GPe*. Inhibitory neurons rise to the *STN*, exciting the *GPi* and the *SNr* (6) (Figure 1 b). Since, as explained above, the *GPi* and *SNr* inhibit the thalamus, this leads to disinhibition of the excitatory output from the thalamus to the motor cortex.

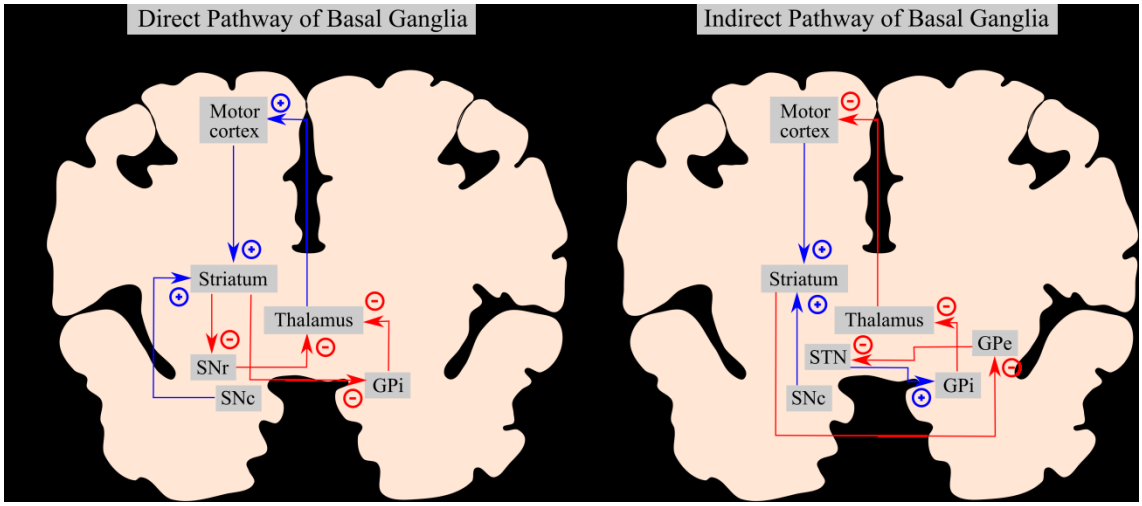

Figure 1: Direct and indirect pathway of the basal ganglia circuit

The direct pathway (a) initiates and executes voluntary movement. The cortex sends excitatory projections to the striatum, which sends then inhibitory projections to the internal globus pallidus. The internal globus pallidus inhibits the thalamus; therefore, its own inhibition leads to an excitation of the motor cortex through the thalamus. In the indirect pathway (b), the striatum inhibits the external globus pallidus followed by inhibitory projections to the subthalamic nucleus. From there, excitatory projections are forwarded to the internal globus pallidus inhibiting the thalamus leading to a decrease in motor activity (6) (image adapted from https://www.kenhub.com/en/library/anatomy/basal-ganglia, last visited 16.10.2023). Abbreviations: SNr = *substantia nigra pars reticulata*, SNc = *substantia nigra pars compacta*, GPi = *internal globus pallidus*, GPe = *external globus pallidus*, STN = *subthalamic nucleus*.

The nigrostriatal pathway and the thalamostriatal pathway control the functions of the basal ganglia circuit. The nigrostriatal pathway connects the *substantia nigra pars compacta* with the caudate and uses the neurotransmitter dopamine for modulation (2).

1.1.2 Dopaminergic System

Carlsson *et al.* discovered dopamine (3-hydroxytyramine), a catecholaminergic neurotransmitter, more than 50 years ago (7). Since then, it has become a well-studied neurotransmitter. Four dopaminergic pathways are known: nigrostriatal, mesolimbic, mesocortical, and tuberoinfundibular. These pathways involve several vital central nervous functions such as movement, reward, sleep, attention, and learning (8).

The biosynthesis of dopamine starts with the amino acid tyrosine, which is taken up from the blood into the brain and introduced into dopaminergic neurons via high- and low-affinity amino acid transporters. Subsequently, it is hydroxylated into dihydroxyphenylalanine (L-DOPA) (25) by the enzyme tyrosine hydroxylase. Dopamine is then synthesized by the DOPA decarboxylase. It is transported from the cytoplasm into specialized storage vesicles, which have a 10-1000 times higher dopamine concentration compared to the cytosol (9).

Upon the arrival of an action potential, calcium channels release Ca^{2+} ions, leading to the fusion of the vesicles with the neuronal membrane and dopamine being released from the presynaptic terminal into the synaptic cleft (9). It subsequently activates members of the G protein-coupled dopamine receptors on the postsynapse (8). Five dopamine receptors are closely related G-protein-coupled receptors (GPCRs) and are divided into two major groups: D1-like (D_1, D_5) and D2-like receptors (D_2, D_3, D_4). D1-like receptors are found in the direct pathway. They are coupled to a stimulating G protein, activating the adenylate cyclase. This enzyme converts the intracellular adenosine triphosphate (ATP) into cyclic adenosine monophosphate (cAMP), leading to a positive stimulus in the cell. D2-like receptors, expressed in the indirect pathway, induce inhibition of adenylate cyclase by coupling to an inhibitory G protein, resulting in less cAMP production and an inhibitory cell stimulus. D_2 receptors and D3 receptors are also expressed presynaptically on dopaminergic neurons (8). D_2 receptors are expressed in the caudate, nucleus accumbens, and olfactory tubercle, as well as in the SN, ventral tegmental area, hypothalamus, cortical area, septum, amygdala, and hippocampus (10). An illustrative overview of the dopamine release process is displayed in Figure 2.

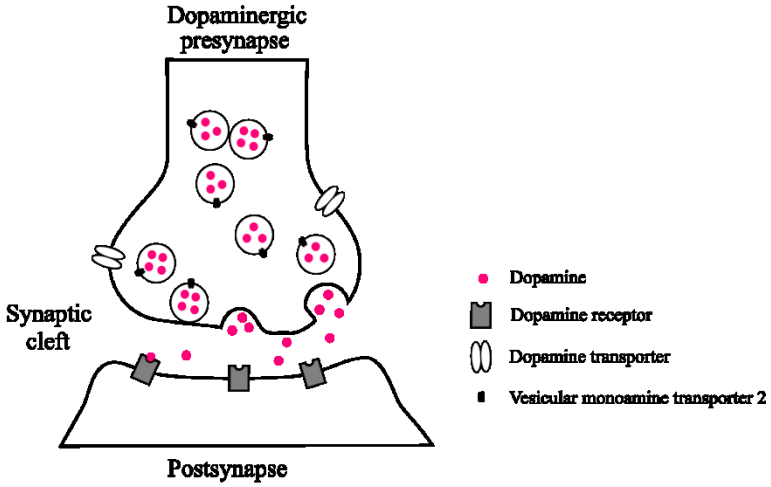

Figure 2: Dopamine release process in the synaptic cleft

Dopamine is synthesized in the presynapse and packed in vesicles via the vesicular amine transporter 2. The vesicles fuse with the membrane of the presynapse and release dopamine into the synaptic cleft. There it binds to dopamine receptors on the postsynapse to start signaling cascades (11) (image adapted from (11)).

The dopamine transporter plays a role in terminating dopaminergic signaling by regulating the dopamine concentration in the synaptic cleft through the reuptake of dopamine into the presynaptic neuron. It is a sodium symporter and uses the Na^+ gradient for the transport of dopamine across the plasma membrane (12).

1.1.3 Proteinopathies

Over 200 years ago, PD was mentioned by James Parkinson in his "Essay on the Shaking Palsy" for the first time (13). Since then, much research has been conducted regarding diagnosis and therapy. However, the symptoms he reported are still common indicators occurring in PD. The disease is characterized as a movement disorder, including motor symptoms such as rigidity, postural instability, and tremor, as well as non-motor indications including sleep disorder, constipation, and hyposmia. PD patients suffer from a loss of the dopaminergic neurons in the SN, leading to a dysregulation of the basal ganglia activity, resulting in the mentioned motor symptoms (14). During disease progression, 80% of PD patients develop cognitive decline, leading to PD dementia (PDD), a disease difficult to distinguish from LBD. The only way to differentiate between those two diseases is through the initial symptoms developed by the patient – motor symptoms indicating PDD and cognitive symptoms indicating DLB (15, 16). These neurodegenerative

diseases bear one common neuropathological feature, the so-called LB, which Friedrich Lewy first described in 1912 (17). LBs and Lewy neurites (LNs) contain the protein αSYN as one major component found in striatal and cortical neurons in PD and LBD patients in the brainstem, limbic system, and cerebral cortex (18). In contrast, in MSA, another synucleinopathie, αSYN, is mainly found as glial cytoplasmic inclusions (GCIs) in the cerebellum (19, 20).

In addition to synucleinopathies, other diseases such as AD, Progressive Supranuclear Palsy (PSP), and Frontotemporal Dementia, to name but a few, also belong to proteinopathies. AD patients show gradual cognitive decline resulting in dementia caused by the increased deposition in soluble protein aggregates, mainly amyloid-β plaques and intracellular neurofibrillary tangles/tau lesions in the temporal and frontal lobe and in the limbic system. Further, the protein αSYN is also involved in the pathophysiology of AD (21). PSP and Frontotemporal Dementia are also neurodegenerative diseases, which aggregate mainly Tau proteins within neurons or glia cells but also show co-occurrence of αSYN (22, 23).

The protein αSYN is an intracellular protein located in the presynaptic terminals of healthy humans (24). αSYN is involved in the early stages of vesicle formation and repeated neurotransmitter release and recycling of vesicles by interacting with the N-ethylmaleimide-sensitive factor attachment protein receptor (SNARE)-complex (25). αSYN exists as a 14 kDa unfolded or a membrane-bound helically folded monomer. During the αSYN aggregation process, these monomers undergo several structural changes (Figure 3), forming different types of small oligomeric species, which are then stabilized by β-sheet interactions. In the next step, protofibrils are formed, which assemble into β-sheet structures called amyloid fibrils found in LBs (24).

Many causes are investigated to be responsible for the aggregation of αSYN, such as disease-related mutations and post-translational modifications. Furthermore, phosphorylation of αSYN, oxidative stress, metal ions, biological membranes, pH environment, and molecular crowding can modulate the αSYN structure and oligomerization (24). Oligomeric forms are considered the most toxic species (26), whereas LBs have been proposed to be less toxic and may be a protection form to trap oligomeric forms (27).

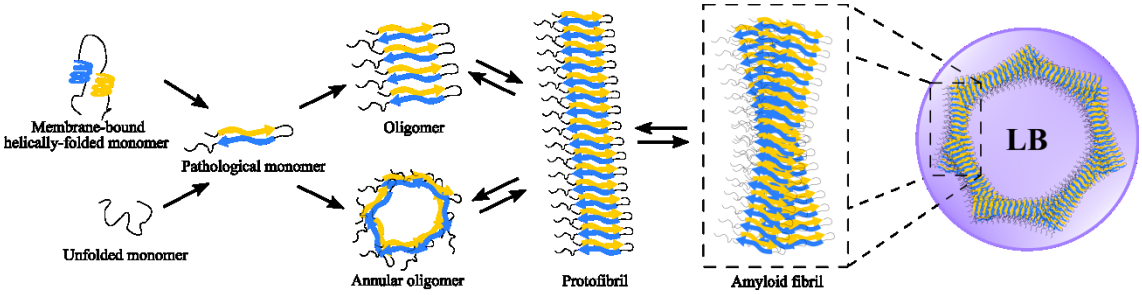

Figure 3: Aggregation process of α-synuclein

In the physiological state, αSYN exists as an unfolded monomer or as a membrane-bound helically-folded monomer. After structural changes, αSYN forms β-sheet accumulations resulting in insoluble protofibrils, which assemble into amyloid fibrils. These amyloid fibrils are then found aggregated in Lewy bodies (24) (image adapted from (24)). Abbreviations: LB = Lewy bodies.

However, not only αSYN fibrils can be found in LBs, but also vesicular structures and dysmorphic organelles. This aggregate protein-lipid compartmentalization makes it challening to detect αSYN due to the massive amount of lipids and proteins as a major component of LB (28). Further, many neurodegenerative diseases do not have a pure pathology but are also characterized by co-pathologies. 30-40% of PD patients also show Aβ plaques and Tau neurofibrillary tangles (16). All these fibrils share a very similar β-sheet structure, leading to compounds not selective for one type of fibril. Therefore, it is essential to look at crossreactivity to Aβ and Tau while screening compounds that target and bind to αSYN.

Animal models of Parkinson's Disease

Many animal models exist to model different neurodegenerative diseases, such as pharmacological-based models (6-hydroxydopmine (6-OHDA)), transgenic mouse models, virus overexpressing animal models, and seeding models.

In familial PD, three missense mutations (A30P (29), A53T (30), E46K (31) were identified and linked to αSYN pathology. Therefore, several transgenic mouse models have been developed, including αSYN knockout or overexpression of αSYN (32-34). The (Thy1)-h[A30P] (A30P) αSYN transgenic mouse model overexpresses a human mutant of αSYN and develops age-dependent movement abnormalities. The transgenic mice show depositions of pathological αSYN fibrils in the midbrain, spinal cord, and brainstem (35, 36). Further, 12-month-old transgenic mice displayed αSYN pathology in the amygdala, an area also involved in human patients. Comparing young (four months) transgenic mice with controls, no differences in behavioral tests such as open field or rotarod were

observed. Mid-age mice become hyperactive, and 70 weeks old αSYN transgenic mice develop significant movement abnormalities (35, 36).

Another model, which develops αSYN positive cytoplasmic inclusions, is the adeno-associated virus (AAV) αSYN overexpressing rat model from Deniz Kirik *et al.* (37). In their study, they used recombinant AAV vectors to overexpress αSYN at high levels in nigrostriatal dopamine neurons in rats by injecting the AAV vector in the *substantia nigra* of one hemisphere up to six months. The other hemisphere serves as internal control, an advantage of this animal model. They observed a progressive neurodegenerative pathology in the nigrostriatal dopamine neurons, displaying αSYN positive inclusions and cell death. Further, the rat model shows pathological alterations in the nigral dopamine neurons accompanied by a loss of 30-80% and 40-50% reduction of striatal dopamine. Significant motor impairments were observed in rats showing a dopamine neuron cell loss above 50-60%. As a control virus, they used an AAV vector overexpressing the green fluorescent protein (GFP), revealing no significant changes in striatal dopamine levels or cell death. However, GFP is known to be toxic at high titers ($>10^{12}$ gene copies per ml), causing cell death up to around 40% (38). Kirik *et al.* also tested this AAV αSYN vector in adult marmosets, revealing αSYN-positive cytoplasmic inclusion in transduced neurons. Further, the marmosets developed motor impairment, which correlates with nigrostriatal damage (39). Using AAV vectors in the nigrostriatal system overexpressing αSYN provides a good model of PD, revealing more neuropathology and cell death in the nigrostriatal dopamine system compared to transgenic mice. This technique offers several advantages: (i) vectors can be applied during any life span of the animal and in any region of interest, (ii) internal control by applying the vector in only one hemisphere, and (iii) vectors applicable in rats, a species which is more beneficial for imaging studies due to their size (37). However, since the control vector GFP also reveals toxicity, another control vector must be considered.

In addition, other animal models, which study the cell-to-cell propagation of αSYN, a mechanism through which αSYN aggregates spread in the brain, use the injection of either brain extracts containing αSYN aggregates or preformed fibrils into brains. The pathology of these brains shows LB-like structures with increased phosphor-αSYN staining, loss of neurons, and some behavioral deficits (40).

Therapeutic approaches in Parkinson's Disease

Several different therapeutic approaches are available to treat PD (see review (41)). This section briefly overviews the most common treatment approaches using various medications and one surgical procedure. Since the lack of dopamine in the caudate putamen is the leading cause of motor symptoms treatments focus most on improving the dopaminergic deficit (42). The "gold standard" for many years has been using L-DOPA to treat the motor symptoms of PD. L-DOPA is a dopamine precursor substance converted into dopamine in the brain. One drawback of long-term use of L-DOPA is that it leads to motor fluctuations and drug-induced dyskinesias (43). Another major role in the treatment of PD is dopamine agonists. These agonists stimulate and activate the postsynaptic receptors in the caudate putamen to imitate the effect of dopamine. Agonists are primarily used in patients who experience motor fluctuations and drug-induced dyskinesia after L-DOPA treatment. In 1997, another treatment strategy was introduced using catechol-o-methyltransferase inhibitors to prevent the metabolism of L-DOPA, leading to an increased bioavailability of L-DOPA in the brain. The combination of catechol-o-methyltransferase inhibitors and L-DOPA allows more L-DOPA to cross the blood-brain-barrier since catechol-o-methyltransferase inhibitors prevent the reaction L-DOPA to 3-O-methyldopa. Using monoamine oxidase inhibitors as another treatment for PD leads to inhibiting of the enzyme monoamine oxidase B, which breaks down dopamine, resulting in an increased amount of dopamine in the basal ganglia (43). A surgical intervention is also available for treating PD called deep brain stimulation. An implanted neurostimulator delivers high-frequency electrical impulses to the brain, typically in the thalamus, globus pallidus, or subthalamic nucleus—patients who are intolerant to the medication benefit from this treatment approach (44).

Despite the many different pharmacological and surgical therapy approaches, PD is still a progressive disease, and therefore, the interest in new potential disease-modifying therapies is tremendous. One disease-modifying strategy is targeting the protein αSYN, which accumulates into pathological aggregates in PD. One approach is the extracellular degradation of aggregated αSYN using active or passive immunization. AFFITOPEs, short immunogenic peptides, actively stimulate the immune system to create antibodies against the target protein αSYN. One example of active immunization is AFF1, which was tested in mouse models, resulting in decreased cerebral αSYN, improved degeneration, dopaminergic loss, and αSYN clearance by microglia (45). A passive immunization strategy with the monoclonal antibody 9E4 in preclinical studies showed, as a passive

immunization strategy, an improvement in αSYN pathology and in motor deficits in a mouse model (46).

Another disease-modifying approach is inhibiting αSYN aggregation using small molecules (47). This thesis focused on the small molecule anle138b and its chemical derivatives for the development of a potential PET tracer, and thus, it will be introduced in more detail here. Anle138b (Figure 4) has been extensively studied (48-54). It is a small molecule characterized by excellent bioavailability and good blood-brain barrier penetration. It does not show any signs of toxicity at therapeutic doses when administered to animals (53). Furthermore, it interferes with the pathological aggregation of αSYN, but there is no indication of binding to monomers (53). Further, the compound showed a reduction in disease progression in a human αSYN mouse model, even when started in the symptomatic disease phase, prolonging the survival of the mice (51). Anle138b application was also shown to partially improve motor function (49) and to reduce αSYN accumulation in PLP-hαSYN mice, a mouse model of MSA (50). Also, anle138b is currently being tested in a Phase 1 b study in patients with mild to moderate Parkinson's disease (NCT04685265).

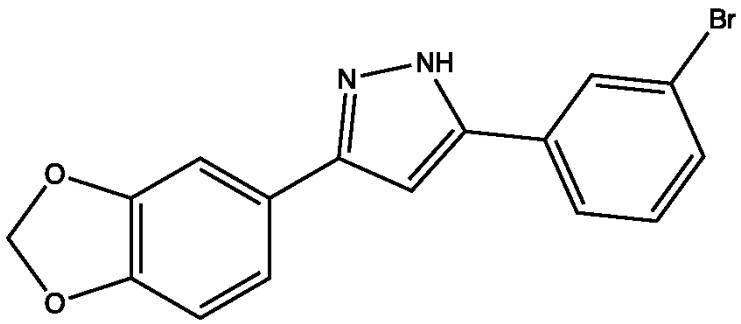

Figure 4: Chemical structure of anle138b

Deeg *et al.* reported a high binding affinity of anle138b (K_d = 190 ± 120 nM) to fibrillar structures *in vitro* (55). Due to its therapeutic characteristics, anle138b was radiolabeled with fluorine-18 and was chosen as the chemical lead for developing new potential PET tracers (56).

1.2 From *In Vitro* Detection to *In Vivo* Imaging Methods

By using different *in vivo* methods, such as PET and MRI, it is possible to gain insight into the complexity of the brain and pathologically altered brain structures. In the first step, *in vitro* methods investigate potential chemical structures as PET tracers that interact with and detect pathological structures. After successful implementation, it is then possible in a second step to use these new potential PET tracers to investigate subjects' brains *in vivo* on a molecular level. However, it is possible to examine brain changes on a molecular and functional level using MRI, allowing us to longitudinally investigate the brain in the diseased state to make progress toward understanding the causes of the disease, the disease progression, and the improvement during therapy.

In the following chapter, *in vitro* detection methods to examine new chemical structures as potential PET tracers and *in vivo* imaging technologies used in this thesis will be described in detail.

1.2.1 *In Vitro* Radioligand Binding Methods

In vitro Binding Assays using liquid scintillation counting

Novel compounds can be screened using *in vitro* binding assays to investigate their binding affinities and selectivity towards a target of interest. In the first step, recombinant proteins are incubated on the scintillator-coated plates. Then, the plate is blocked with a non-reactive protein such as bovine serum albumin (BSA) to block non-specific binding sites of the tracer to the plate. In the case of tracer binding to the protein, the tracer is located close to the bottom of the scintillator-coated plates (57).

Two different kinds of binding assays exist to determine the affinity of a compound for a target of interest. Saturation binding assays determine a radiolabeled compound's affinity ($1/K_d$) for a target protein and the number of binding sites. Competition binding assays are performed to assess the inhibition of a non-radioactive compound to the target of interest (K_i) that binds to the same binding site as the radioactive compound.

Saturation binding assays involve the addition of increasing concentrations of a tracer to a constant concentration of the target of interest to determine the total binding. The maximum concentration should be at least ten times the K_d. Non-specific binding is obtained in a second set of binding reactions by adding an excess (1000-fold) of the non-radioactive compound. Non-linear regression analysis estimates B_{max} (number of binding sites) and K_d (dissociation rate constant). To calculate the specific binding of the tracer, the non-

specific binding is subtracted from the total binding. The affinity of a tracer is defined by $1/K_d$, meaning the lower the K_d, the higher the affinity of the tracer. Competition binding assays are performed by adding increasing concentrations of the non-radioactive competitor (0-100% occupancy) to a constant concentration of the tracer and target of interest. Herewith, the affinity of a non-radioactively labeled competitor of the radioligand can be determined (57).

In vitro Autoradiography

In vitro, AR is used to investigate the specific binding of a radiolabeled compound in animal or human tissue sections. It gives direct and spatial information about the binding specificity of the tracer toward its target, as it can be directly compared to the immunohistochemical identification of the target of interest (58).

Tissue sections are incubated with a predefined concentration of the radioactive tracer in an appropriate incubation buffer to obtain binding of the tracer to the tissue sections with a high target-to-background ratio. To determine the non-specific binding of the tracer in tissue, consecutive tissue sections are incubated with ~1000-fold excess of the non-radioactive compound or a competitor targeting the same binding site. A tissue standard is and the dried tissue sections are added to the imaging plate to quantify the AR. Tissue standards consist of defined increasing activity concentrations, which correlate linearly with different grey values on the plate after readout and are used to determine the radioactivity concentration of the samples (57).

Imaging plates used for tritium AR are either phosphor screens or radiosensitive films. Both have their advantages and disadvantages, which have to be considered. Phosphor screens have no protective coating to allow the low energy of tritium to reach the phosphor crystals. Therefore, they are susceptible to contamination and are not reusable. However, the exposure time of phosphor screens is much shorter (days) compared to the radiosensitive films (weeks) due to their higher sensitivity. Radiosensitive films are susceptible to light and must be developed using hazardous chemicals in a dark room. However, these films have a higher spatial resolution of <1 µm compared to phosphor screens (50 µm) and are less expensive (57, 59).

1.2.2 Positron Emission Tomography

PET is a nuclear imaging technique based on the β^+ decay of radionuclides, creating 3-dimensional images to investigate metabolic processes and receptor interactions *in vivo*. The compound is labeled with a radionuclide, introduced into the body by intravenous injection, and distributed according to the linked biomolecule. Based on the radionuclide's decay, a positron is emitted from the nucleus to reach a steady state. The positron travels through the surrounding tissue until it hits an electron. Since the positron and electron are oppositely charged, they annihilate (positron/electron annihilation), producing two 511 keV photons traveling in opposite directions at an angle of ~180°. They are subsequently detected by a detector ring surrounding the subject. The scanner detectors can convert these high-energy photons into electrical signals, which are then reconstructed into a 3-dimensional image displaying the distribution of the radiolabeled compound in the tissue.

The following chapter will explain the essential PET physics, acquisition, correction methods, and reconstruction algorithms and describe the quantitative analysis of the PET signal in the brain.

Basic Physics

The atom's nucleus contains positively charged protons and neutral neutrons, surrounded by electrons. Uncharged atoms hold the same number of electrons and protons, resulting in a stable state. Atoms become unstable if a nucleus has excess protons or neutrons, which induces radioactive decay. Based on the decay, the number of protons or neutrons changes and can lead to a more stable nucleus configuration. Nuclei with excess protons, which decay through positron emission, are called β+ emitters. The proton is converted into a neutron and a positron, an antiparticle to an electron. Following β+ decay, the positron is ejected from the nucleus and loses its kinetic energy by interaction with other electrons in the surrounding tissue until it links with an electron, resulting in a positronium. This process is called annihilation. The energy is subsequently released in the form of two high-energy 511 keV photons, which are emitted simultaneously in roughly opposite directions (180°) (60). This fundamental principle of PET is illustrated in Figure 5 a.

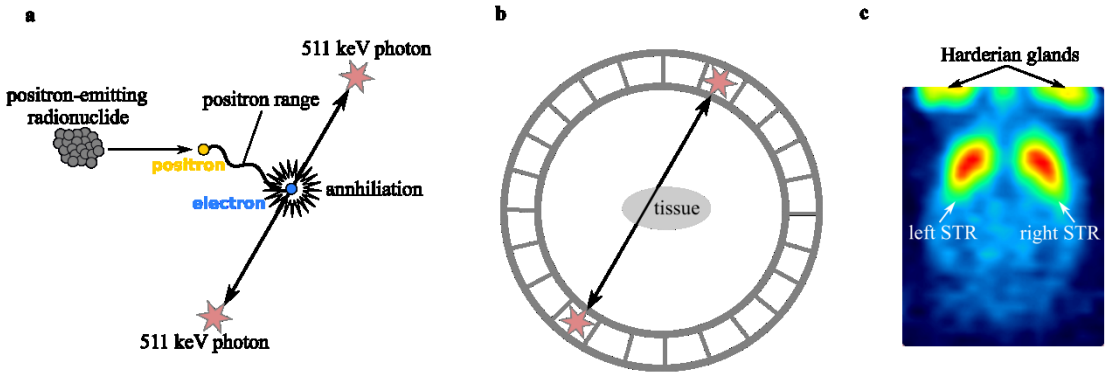

Figure 5: Basic principle of Positron Emission Tomography.

An emitted positron travels a short distance in the surrounding tissue (positron range) and annihilates with an electron. The positron and electron are annihilating and two photons with an energy of 511 keV are created (a). The detector ring surrounding the tissue detects on two opposite detectors both photons within a certain time and energy window (b) (Images adapted from (61)). Exemplary PET image summed up over 60 minutes of a [^{11}C]raclopride scan indicating the left and right caudate of a rat brain (c).

The annihilation process is projected along a line between two opposite detectors, referred to as line of response (LOR). Several detectors are arranged in a ring design surrounding the object of interest. A detector consists of a special crystal (also called a scintillator) coupled to a light detector. The scintillator material captures high-energy photons and converts them into light. The coupled light detector transforms and amplifies the light pulse into an electrical signal. A large number of LORs are collected at different angles, covering the field of view (FOV) (60).

Ideally, the scanner only detects true coincidences, which are two detected annihilation photons originating from the same radioactive decay with no change in direction or no loss in energy (Figure 6 a). However, undesired events such as scattered, random, or multiple coincidences are recorded as well (Figure 6 b-d) (60).

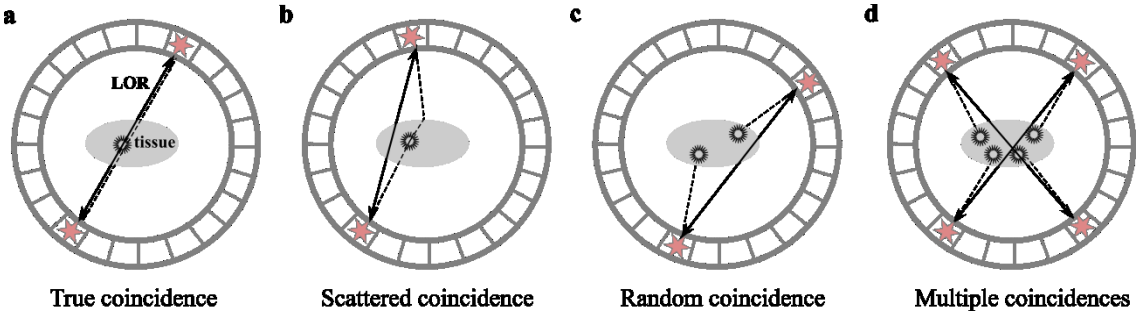

Figure 6: Different types of coincidences.

In the case of true coincidences (a), two opposite detectors identify both photons without being scattered. Scattered coincidences (b) occur if one or both photons are deflected by the surrounding tissue leading to incorrect information of the distribution of activity. Photons of random coincidences (c) originate from two different annihilations but are detected in the same time and energy window resulting in an incorrect line of response. The fourth possible type of coincidence is that of multiple coincidences (d). Four photons are detected in the same energy and time window. As a result, it is not possible to distinguish between the photon pairs which resulted from the same annihilation. Scattered and random events can be corrected (60) (Image adapted from (60)).

In scattered coincidences, one or both photons change direction due to interaction with the surrounding tissue before they reach the detector pair. Hence, the assigned LOR to this coincidence event is incorrect. Scattered coincidences reduce the image contrast, resulting in inaccurate image quantification (60). Random coincidences occur when two unrelated photons from different annihilations are detected, causing an increased background signal (60). If three or more coincidences are detected, multiple coincidences emerge (60). Scattered and random coincidences can be corrected using sophisticated algorithms to avoid influences on image quantification (60).

Correction Methods

Before the image reconstruction, several correction methods must be applied to the raw data so that each voxel represents the actual PET tracer activity concentration (60).

Detector inefficiencies, geometrical variations, or variations in detector electronics can result in inaccurate coincidence detection efficiencies. Therefore, a normalization of the system corrects each measured LOR by a multiplication factor compensating for the before mentioned variations (60).

The annihilated photons are attenuated in the surrounding tissue, which can influence the quantification. Attenuation correction can be measured in two ways: either with a transmission source (e. g., Co57) rotating around the tissue or with a computed tomography

(CT) scan. The measured attenuation map represents the spatial distribution of tissue attenuation coefficients within the PET FOV (60).

Scattered events differ from true events in their energies. Scattered events would be ignored if a detector only detected the annihilated events with an energy of 511 keV. However, commercially available detectors have only an energy resolution between 10% and 20%, hence an energy window around the 511 keV peak. Scatter correction can be performed using analytical, simulation, and dual-energy methods (60).

Another method is the correction of the detector dead time. After a pair of detectors record an event, the detectors cannot detect another photon due to the processing time. This dead time depends on the detector's electronics, the scintillation crystals, and the injected activity amount (60). To correct for the dead time of the detectors, various methods can be used. The easiest method is based on phantom measurements of different activity levels, which are stored in so-called “look-up” tables. During the emission, the actual activity is determined based on the decay and corrected for dead time using the value from the “look-up” table. The disadvantage of this method is that the inhomogeneity of the activity distribution is not considered. More complicated methods are based on analytical methods, which simulate the dead time based on the scanner geometry and compare these results with phantom measurements (62).

Histogram and Reconstruction

The acquired events are stored in a list-mode file containing all information collected during the acquisition, such as energy, event time, and detector position. All acquired events are histogrammed into a sinogram by sorting all LORs according to their orientation in the scanner FOV. Static or dynamic histograms can be executed. In the static mode, all coincidences are used to create one sinogram with no information about the temporal distribution of the PET tracer. Several time frames are defined in the dynamic mode, and coincidences in the respective time frames are histogrammed in separate sinograms. For each time frame, the distribution of the tracer can be evaluated.

The resulting sinogram can be reconstructed into an image using different reconstruction algorithms (62). In general, two reconstruction methods (analytical and iterative reconstruction algorithms) are used for PET. Filtered back projection (FBP) is an analytical approach that reconstructs the image fast, however, with an increase in noise. Iterative approaches, such as the ordered subset expectation maximization (OSEM) algorithm, can

be more time-consuming since detector-specific parameters and correction methods can be included. However, image quality is improved (63).

PET Quantification

Dynamic PET measurements are used to investigate the temporal distribution of the PET tracer in an organ of interest, such as the brain. The PET scan is divided into different time frames to follow the accumulation of the radioactivity over time.

The most frequently used parameter for the description of receptor-ligand interaction is the binding potential (BP). It is defined as the density of the available receptors (B_{avail}) times the affinity of the ligand ($1/K_d$) with K_d being the equilibrium dissociation constant and is described by the following equation:

$$BP = \frac{B_{max}}{K_d} = \frac{B_{avail}}{K_d} \quad (1)$$

where B_{max} stands for the total density or concentration of the receptors in a sample of tissue. For *in vivo* imaging, the term B_{avail} is used because not all receptors are available for radioligand binding due to the occupancy with the endogeneous neurotransmitter (64).

The specific binding describes the binding of the tracer to the target receptor. The non-specific binding is defined as the binding of the tracer to other proteins in tissue than the target molecule. Non-displaceable binding is the sum of non-specific and free tracer concentrations in the tissue. BP_{ND} is defined as the ratio of specific binding to non-displaceable tracer binding (64). It can be calculated with the following equation:

$$BP_{ND} = \frac{V_T - V_{ND}}{V_{ND}} = \frac{V_T}{V_{ND}} - 1 = DVR - 1 \quad (2)$$

where V_T is the volume of distribution in the region of interest and V_{ND} is the volume of distribution in the reference region. The term V_T/V_{ND} is referred to as distribution volume ratio (DVR) (64, 65).

PET Imaging of Neurotransmitter Release

To measure concentrations of a neurotransmitter in the brain, it is possible to use imaging modalities such as PET. Therefore, dynamic measurements of neurotransmission are conducted by competition between the endogenous neurotransmitter and the used imaging radioligand for a defined neuroreceptor. The neurotransmitter competes with the radioligand for the occupation of the binding site at the receptor. A typical way to study neurotransmitters with PET is to either apply an agonist to activate neurotransmitter release and

increase the concentration of the neurotransmitter in the synaptic cleft or to apply an antagonist to block the activity of a receptor to increase the neurotransmitter concentration in the synaptic cleft. Increasing the neurotransmitter concentration in the synaptic cleft results in a lower radioligand binding and *vice versa* (66).

This approach has often been applied to measure changes in dopamine concentration using [^{11}C]raclopride, an antagonist-radioligand binding to the D_2 receptor. It is the most extensively studied radioligand for indirectly measuring dopamine availability and release changes. In various rodents, monkeys, and human studies, a pharmacological stimulation with amphetamine was used to modify the endogenous dopamine concentration, which can be tracked by a change in [^{11}C]raclopride binding (66). Amphetamine reallocates dopamine from the synaptic vesicles to the cytosol, quickly released by reverse transport of the dopamine transporter (67).

Changes in [^{11}C]raclopride binding due to dopamine neurotransmission can be explained by two theoretical approaches: the competition or occupancy model and the internalization model (Figure 7). The occupancy model (Figure 7 a) describes that by using a stimulation, which increases the synaptic dopamine concentration, the occupancy of the D_2 receptor increases, and the availability of the D_2 receptor for the radioligand decreases. Decreasing the synaptic dopamine concentration induces a decrease in the D_2 receptor occupancy and increases the D_2 receptor availability for the radioligand. The internalization model (Figure 7 b) states that the increase in dopamine distribution leads to an internalization of the D_2 receptor after high levels of dopamine release. The receptor is internalized into the endosomal compartment, causing some receptors to be externalized or internalized on the plasma membrane. Under stimulated conditions, the neurotransmitter release will lead to receptor internalization. Therefore, the binding of the radioligand decreases due to the reduced affinity for the internalized receptor, reduced available binding sites, or both. A decrease in neurotransmitter release could, in turn, retrieve the internalized receptors back to the cell surface, resulting in increased available binding sites or increased affinity, leading to increased binding of the radioligand (66, 68).

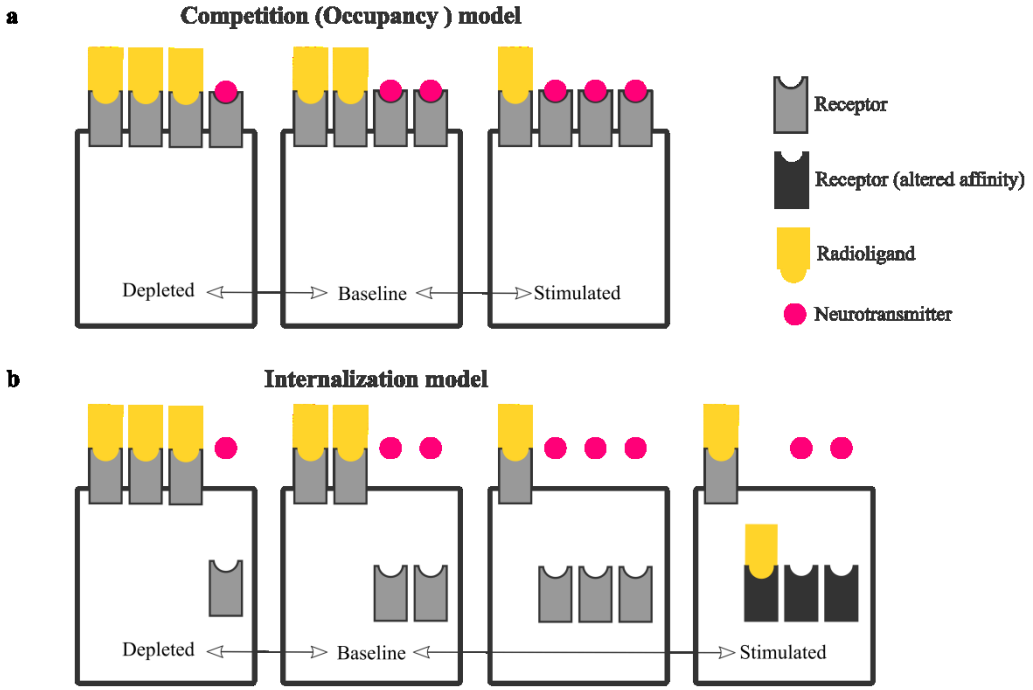

Figure 7: Competition and internalization model for imaging neurotransmission.
In the competition or occupancy model (a), the radioligand as well as the neurotransmitter bind to the receptor at baseline condition. Stimulating neurotransmitter release results in increased occupancy of the receptor by the neurotransmitter and decreased radioligand binding. Likewise, if the neurotransmitter is depleted, the binding of the radioligand increases, whereas the neurotransmitter binding decreases. The internalization model (b) emphasizes the theory that the receptors are distributed externally and internally on the plasma membrane depending on the stimulation. More internalization occurs through increased neurotransmitter release. Depletion of neurotransmitters leads to receptor externalization (66) (image adapted from (66)).

Two methods are used for measuring dopamine in the synaptic cleft: the bolus and the bolus plus constant infusion method. For the bolus method, a baseline measurement is conducted before the blocking experiment in the same animal. To change the receptor occupancy, blocking with a pharmacological stimulation is applied before the radioligand application. The receptor changes are compared to the baseline measurement. Another method to measure dopamine concentration is displacement experiments during a bolus infusion of the radioligand. To reach a fast equilibrium state of the radioligand, a bolus followed by a constant infusion is applied. After recording the baseline, a pharmacological stimulation is injected during the equilibrium period in the same measurement, leading to a displacement of the PET ligand. The advantage of this method is that the pharmacological stimulation is applied in the same measurement and under the same physiological conditions (66, 68).

1.2.3 Properties of a Central Nervous System PET Tracer

A CNS PET tracer must fulfill several properties and characteristics compared to a therapeutic compound (Figure 8). First, the chemical structure must be accessible to incorporate a radionuclide such as carbon-11 or fluorine-18. The advantage of carbon-11 is that there are several ways to label a compound with carbon-11 without changing its chemical structure. However, carbon-11 ($T_{1/2}$ = 20.4 minutes) has a much shorter half-life than fluorine 18 ($T_{1/2}$ = 109.7 minutes). Regarding fluorine-18 labeling, defluorination can be an issue, particularly in the skull, resulting in spillover into the adjacent brain regions. Next, the CNS PET tracer has to be potent and selective towards its target protein. The affinity $1/K_d$ of a tracer is determined by its maximum concentration of target binding sites B_{max}. Generally successfully used PET tracers show an *in vitro* binding potential of $(B_{max}/K_d) \geq 10$ (69). In the case of a low target availability (such as αSYN), the desired affinity needs to be in the picomolar range.

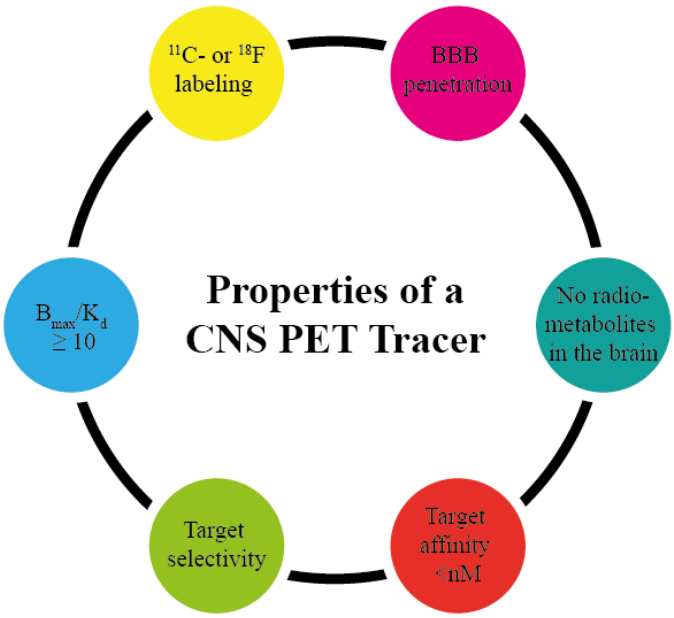

Figure 8: Properties for an ideal central nervous system PET tracer.

Several criteria need to be fulfilled for an ideal PET tracer for the central nervous system. First, the chemical compound should offer the possibility for ^{11}C- or ^{18}F-labelling. Second, the PET tracer needs to cross the blood-brain barrier, while radio-metabolites should not enter the brain as they are indistinguishable from the parent compound in tissue. It should have high target specificity, a good target affinity in the subnanomolar range as well as 30 to 100-fold higher target selectivity. The *in vitro* binding potential calculated as B_{max}/K_d should be higher than ten (70).

Furthermore, a CNS PET tracer must penetrate the blood-brain barrier and exhibit a low non-specific binding in the brain for a good target-to-background ratio. The pharmacokinetic profile of a suitable CNS PET tracer shows a fast brain uptake and a fast washout

from the brain with low or no off-target and non-specific binding. To reduce the non-specific binding, the log*P* value, which is a measure of lipophilicity or hydrophobicity, should be in a range of 1.5-2.5, resulting in low non-specific binding but reasonable brain uptake. Additionally, a CNS PET tracer needs to have low to no brain penetrating radioactive metabolites, since it is not possible to distinguish the parent PET tracer and its radioactive metabolites in tissue influencing the quantification of the PET data (70). No promising αSYN PET tracers were published at the beginning of this thesis. However, over the years more and more research has been done and there are now a number of potential PET tracers available, which are described in more detail in the discussion.

1.2.4 Magnetic Resonance Tomography

MRI is an imaging technique used in medical diagnostics to obtain anatomical images and several different functional parameters. MRI contrasts are generated through the manipulation of protons by a strong magnetic field (71).

Basic Physics

MRI utilizes the nucleus of hydrogen atoms ($_1$H) for imaging. The whole atom is composed of one proton and one electron circling around the nucleus. The proton is spinning around itself, producing an angular magnetic momentum. Without an external magnetic field, the spins are randomly oriented in space, and the total magnetization is zero. By applying a strong magnetic field B_0, the spins line up along the field and are oriented parallel or antiparallel. A measurable net magnetization is created as more protons align in the antiparallel direction of the static field (71).

Protons have a spin or an angular momentum and precess around the direction of the applied magnetic field. This precession frequency is described as Lamor frequency ω_0:

$$\omega_0 = \gamma * B_0 \quad (3)$$

γ is a function of the nucleus specific constant known as gyromagnetic ratio

B_0 is the magnetic field

There is a longitudinal magnetization M_Z under stable conditions. If a radiofrequency (RF) pulse of 90° is applied, the whole magnetization goes from z-axis to x-y-axis and induces an MR-signal in the receiving coil, called free induction decay (FID). The MR signal can only be detected during a short time due to signal decay called relaxation (71).

Relaxation

There are two different relaxation processes (Figure 9): T1 (longitudinal relaxation), also called spin-lattice relaxation, and T2 relaxation (transversal relaxation), called spin-spin-relaxation. T2* is a relaxation described by the T2 relaxation influenced by inhomogeneities of the static magnetic field (71).

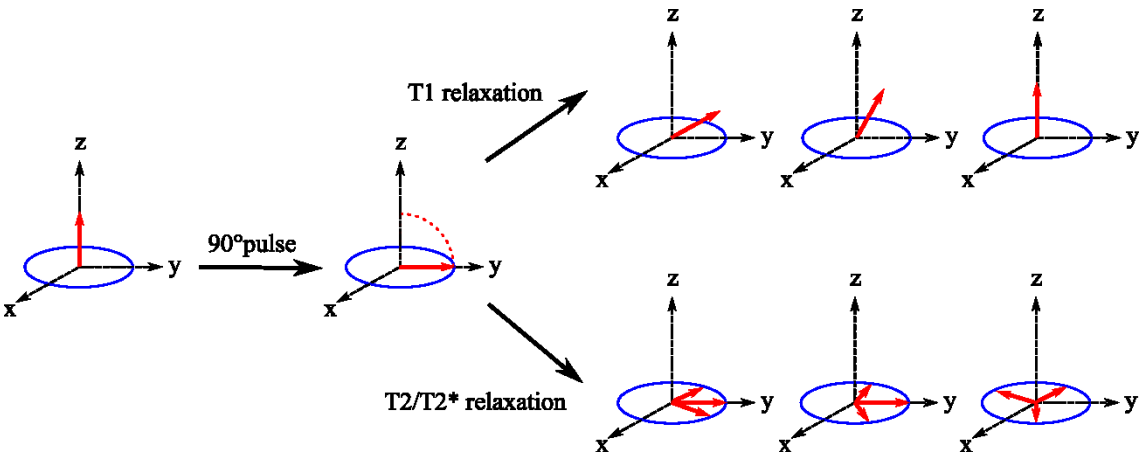

Figure 9: Schematic representation of T1 and T2 relaxation processes.

After applying a 90° radiofrequency pulse, the spins flip into the x-y-axis. During the T1 relaxation process (top row), the spins tilt back into the z-axis releasing energy into the surrounding. In the T2 and T2* relaxation process, the spins dephase without releasing energy to the surrounding. Both relaxation processes occur at the same time (71) (image adapted from (71)).

T1 relaxation: After the 90° RF pulse, all the spins are excited to an energetically higher level and in transversal magnetization. This magnetization decreases over time, and the spins return back to a lower energetic level M_Z. The measurable MR signal decreases as well (71).

T2 relaxation: After the excitation, all spins are in phase having the same angle. Over time the phase coherence is lost, and all the spins have different angles spinning faster and slower. Here, the transversal magnetization is decreasing by dephasing of the spins, and the MR signal is vanishing. Since the spins are little magnets, they exchange energy and start to dephase, which changes the magnetic field. Another reason for dephasing is the inhomogeneity of the magnetic field B_0 caused by the machine itself or the investigated object. Both T2 relaxation and field inhomogeneities are responsible for the T2* relaxation (71).

Both relaxation processes are independent of each other and appear at the same time. However, the T2 relaxation is a lot faster (100-300 ms) than the transversal magnetization (0.5-5 s) (71).

Relaxation times differ between tissue types, which can be used to generate various contrasts. Contrasts are obtained by adjusting repetition time (TR) and echo time (TE). TR is the time between two RF-pulses and impacts the T1 contrast. TE is the time between the RF-pulse and the receipt of an echo signal. Choosing TR short (<600 ms), tissue with a short T1 appears bright since the spins relax quicker, and more transversal magnetization is available at the subsequent excitation. Tissue with a long T1 appears dark because the spins need more time to relax and produce a weaker signal. TE influences T2 in the image contrast. By choosing a long TE (>60 ms), tissue with short T2 appears dark because the spins have already lost most of their magnetization and produce, therefore, a weak signal, whereas tissue with long T2 appears bright (71).

The gradient echo sequence (GRE), applied in this work, is commonly used for functional MRI to correlate it with neural activity since it allows acquiring images fast due to a short TR. The sequence consists of a single RF pulse in combination with a readout gradient of opposite polarity. After the excitation, a dephasing gradient is applied across the subject, causing a change in the local field and a variation in the resonance frequencies (72).

Functional Magnetic Resonance Imaging

Ogawa *et al.* were the first researchers to describe the Blood Oxygen Level-Dependent (BOLD) contrast. They discovered that it is possible to visualize the blood vessels when the deoxyhemoglobin in the red cells increases using a gradient echo pulse sequence at high magnetic field strength. In other words, the authors revealed the contrast mechanism reflecting the blood oxygen level today called the BOLD effect (73-75).

Functional magnetic resonance imaging (fMRI) provides a non-invasive method to image brain activity with good spatial and temporal resolution. The contrast of a BOLD-fMRI measurement results from the different magnetic properties of deoxygenated and oxygenated hemoglobin in the blood. Deoxygenated hemoglobin is paramagnetic, and oxygenated hemoglobin is diamagnetic. More oxygen is used through the activation of the neurons, resulting in more deoxygenated hemoglobin. Since deoxygenated hemoglobin is strongly paramagnetic, a decrease in the T2 and T2* relaxation times is caused, and therefore, the BOLD-fMRI signal is decreased (76). Physiologically, the BOLD signal is composed of changes in cerebral blood flow, cerebral blood volume, and metabolic rate of oxygen consumption. By applying neuronal stimulation, the characteristic BOLD signal curve called the hemodynamic response function, can be obtained (Figure 10). It is described by a first initial signal dip due to increased oxygen extraction. Next, the signal

increases, indicating an increase in regional blood flow, delivering oxygen in excess. The peak is reached after 4-6 s. The response ends with a post-stimulus undershoot before the signal returns to baseline. This undershoot occurs due to different cerebral blood flow dynamics and cerebral blood volume, indicating higher deoxygenated hemoglobin than oxygenated hemoglobin (77).

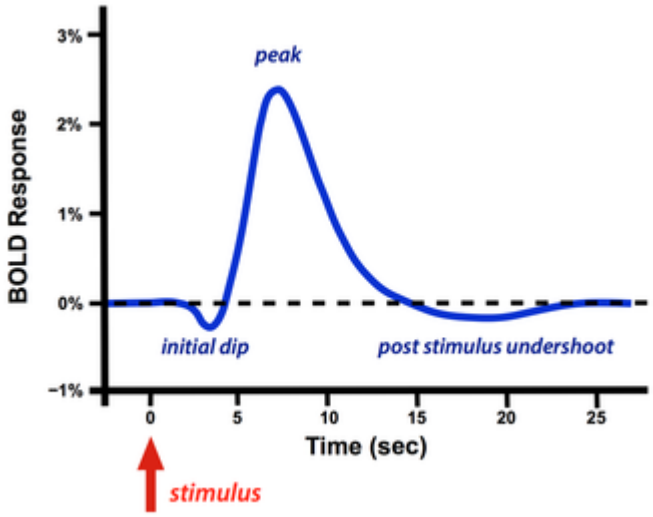

Figure 10: BOLD Hemodynamic response function after an applied single stimulus.
The curve typically illustrates an initial dip due to either increased oxygen in the blood or increased cerebral blood flow followed by a peak resulting from an increased cerebral blood flow to provide nutrients. The curve ends with a post-stimulus undershoot induced by a higher proportion of deoxygenated and oxygenated hemoglobin (77) (Image from https://mriquestions.com/does-boldbrain-activity.html, last visited 28.10.2023)

Neuronal activation can be detected using the BOLD effect. Two different stimulation methods exist (78):

1. Stimulus-evoked BOLD uses either a task or a non-pharmacological stimulation to study brain activation patterns.
2. Pharmacological BOLD uses pharmacological agents to investigate the influence of the agent on the brain.

Functional connectivity

After the discovery of the BOLD contrast, the field of neuroimaging started to evolve. Researchers began to investigate the source of the BOLD signal, which was relatively small compared to the noise surrounding it, such as the scanner noise, and also noise from physiological sources from the investigated subject, such as respiration and pulsation of

the blood in the brain. In 1995, Biswal *et al.* examined the physiological source of noise by scanning subjects carrying out a task and at rest. After regressing the physiological noise sources, he observed a high temporal correlation between different brain regions, such as the left and right motor cortex at rest. He identified time courses of low frequency (<0.1 Hz) fluctuations in the resting brain and concluded: *"... that correlation of low frequency fluctuations, which may arise form fluctuations in blood oxygenation of flow, is a manifestation of functional connectivity of the brain."*(79).

Since the discovery of resting state functional connectivity, although still debated, it has been used in many neurodegenerative diseases such as PD to give an insight into the pathophysiology, treatment effects, and compensatory mechanism (80). For example, the default-mode network, reported by Raichle *et al*. in 2001 as the baseline state of the brain (81), revealed a malfunction of the default-mode network during an executive task due to dopamine depletion (82). Further, the effect of L-DOPA has been investigated in PD patients and compared to a placebo group, showing an effect on the default-mode network improving the physical state of PD patients (83). Another study revealed an effect on the default-mode integrity and task-related brain activations in PD patients without cognitive impairment in a dose-dependent manner (84).

There are several different resting-state analysis approaches available. However, before analyzing the fMRI data, the acquired images must undergo several preprocessing steps. The preprocessing includes (i) realignment to correct for motion artifacts, (ii) coregistration of the fMRI images to an anatomical reference image, (iii) normalization to a standard template to ensure a precise overlap of the brain areas among the subjects since brains can differ in size and shape, (iv) spatial smoothing and (v) nuisance regression. There are multiple techniques available to study the functional connectivity between different regions of the brain. Seed-based analysis and independent component analysis are the most common methods to investigate functional connectivity.

For seed-based analysis, time-series of regions are extracted based on an atlas and pair-wise correlations are calculated for the different brain regions. As a result, a whole brain connectivity map is generated to display correlations for every region (Figure 1).

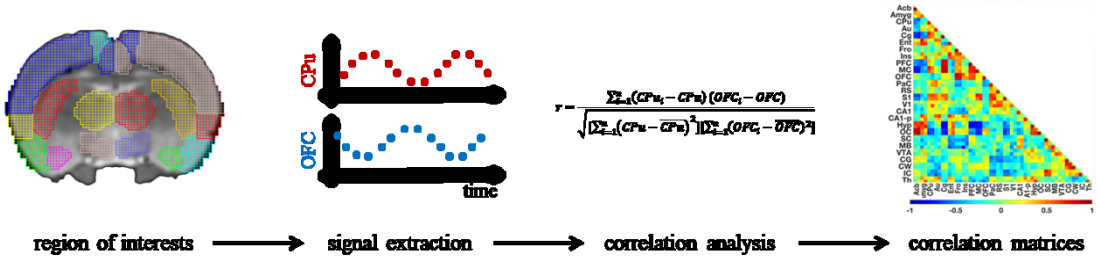

Figure 11: Overview of the steps for functional connectivity analysis.

The signal of different region of interests are extracted and then used for correlation analysis. The results for each region are illustrated in correlation matrices

For example, the BOLD signal of each voxel over time is extracted to statistically test the BOLD signal during stimulation against the BOLD signal during resting-state. The statistical test can indicate the lack or presence of activations. The functional connectivity is calculated between two regions of interest (ROIs). Therefore, the BOLD signal is extracted for both ROIs and then a temporal correlation using Pearson's correlation coefficients is performed. These pair-wise coefficients for each pair of regions can be illustrated as a correlation matrix indicating the functional connectivity. These correlation matrices show color-coded correlation coefficients between different brain areas, revealing positive or negative correlations (85).

The Pearson's correlation coefficient r is calculated using the following equation:

$$r = \frac{\sum_{i=1}^{n}(x_i - x)(y_i - y)}{\sqrt{[\sum_{i=1}^{n}(x_i - \overline{x})^2][\sum_{i=1}^{n}(y_i - \overline{y})^2]}} \quad (4)$$

where n is the number of time-points, x and y are the BOLD values of two regions over a period of time, x_i and y_i are the BOLD values at time-point i, $\bar{x}$ and $\bar{y}$ are the arithmetical sample means of the respective values at all time-points.

Another way to analyze functional networks is the independent component analysis. For this analysis, no *a priori-defined* region is necessary. It is a data-driven approach in which the complete signal of the brain is separated into independent components. The independent component analysis can identify signal fluctuations by their spatial and temporal profiles regarding the BOLD signal. Each voxel can contribute to every component, creating a resting state network (86).

As an alternative to the two fMRI analysis methods, a graph theory approach can assess the global and local organization in the healthy or diseased brain. This analysis method considers the brain as a complex network containing nodes (anatomical regions of interest) connected by edges, representing relationships between the nodes (connectivity). Several properties of the brain regions can be evaluated, such as the degree of a node revealing the number of edges linked to one node (connectivity of one node in one network) or nodal centrality, which quantifies the importance of a node in a network (87).

2 Objectives

Non-invasive imaging methods such as PET and fMRI are valuable tools for the diagnosis of neurodegenerative diseases. They enable the differential diagnosis and monitoring of disease progression or disease-modifying treatments. However, for proteinopathies, specific PET tracers to detect the underlying cellular pathology, which would allow to determine therapeutic efficiencies or treatment strategies, are still missing. Moreover, no systematic *in vivo* work has been performed to link synaptic dysfunctions induced by the pathology to functional changes. Therefore, there is an unmet need to develop novel imaging tools and protocols for the early detection of proteinopathies.

For this reason, the aims of the present thesis were:

1. The establishment of *in vitro* radioligand binding experiments and subsequent evaluation of the binding affinity and selectivity of four anle138b derivatives, as well as the *in vivo* evaluation of one compound, MODAG-001, to αSYN aggregates towards developing a novel PET tracer targeting αSYN pathology in the human brain (direct imaging of αSYN pathology).
2. To develop a multimodal imaging approach to link protein aggregation to molecular and functional neuronal changes in an animal model of αSYN overexpression (indirect imaging of αSYN pathology).

2.1 Part I: *In vitro* and *in vivo* evaluation of the binding affinity and selectivity of anle138b derivatives to α-synuclein aggregates

In the first project, chemical derivatives of the lead compound anle138b, a compound known to have an inhibitory effect on the aggregation of αSYN, were tested in binding experiments. To determine target selectivity and binding affinity (K_d) *in vitro*, we established an αSYN fibril binding assay. Furthermore, the selectivity of the compounds was tested on brain sections of different mouse models of AD, as well as in human AD tissue, to evaluate the binding to Aβ aggregates and further compared to the amyloid PET tracer Pittsburgh Compound B (PIB). MODAG-001 was further examined towards its binding specificity on human brain tissue of different proteinopathy cases, including PD, AD, PSP, MSA, and corresponding controls. In addition, after carbon-11 labeling of MODAG-001, the pharmacokinetic and metabolite profile was examined *in vivo* in healthy mice, and its binding to αSYN in the A30P transgenic mouse model. The found radiometabolite in the brain was the demethylated precursor of [^{11}C]MODAG-001, MODAG-005. After titration of MODAG-005, the compounds binding specificity was further tested in brain tissue of different proteinopathies.

2.2 Part II: A multimodal imaging approach to link protein aggregation to molecular and functional neuronal changes in an animal model of α-synuclein overexpression

In the second project, a simultaneous [^{11}C]raclopride-PET/fMRI protocol was developed and applied to measure dopamine release after a pharmacological stimulation *in vivo* in an αSYN overexpression rat model. To reach this goal, this project was divided into two subchapters.

2.2.1 Evaluation of the Variability and Reliability of a Simultaneous [^{11}C]Raclopride-PET/BOLD-fMRI Approach

Imaging technologies such as hybrid PET/fMRI provide the great potential to study molecular and functional changes simultaneously *in vivo*. However, before molecular and functional changes can be quantitatively measured in animal models, the readouts' reproducibility and reliability must be determined. Therefore, test-retest experiments were performed, and the variability and reliability within and between subjects were determined for both [^{11}C]raclopride-PET and BOLD-fMRI scans.

2.2.2 Investigation of Molecular and Functional Changes in an α-synuclein Rat Model of Parkinson's disease

Combining pharmacological MRI (phMRI) with PET offers excellent potential to investigate brain network modulations through different neurotransmitter systems, providing a deeper insight into the coupling of molecular and functional neural mechanisms underlying specific processes in the healthy and the diseased brain. In this study, a simultaneous [^{11}C]raclopride-PET/phMRI protocol was used to investigate neurotransmitter-receptor interactions with functional connectivity in healthy rats and in a rat model of PD after applying *d*-amphetamine as pharmacological stimulation. The focus of this study was the investigation of the modulation of dopamine dynamics since it is involved in several vital central nervous functions such as movement, reward, sleep, attention, and learning. Furthermore, dopamine depletion in the nigrostriatal pathway is a hallmark of PD, which has been reported to be involved in the impaired modulation of frontal cortical activity. For the rat model used in this study, dopamine neurons in the substantia nigra pars compacta are reduced by 30-80% after the overexpression of the protein αSYN (37). Therefore, the

dopaminergic network, including the four different dopaminergic pathways (nigrostriatal, mesolimbic, mesocortical, and tuberoinfundibular) and the default-mode network, which is partially modulated by dopamine (88), were investigated. The overall aim of the study was to assess changes in functional connectivity of the dopaminergic network and the default-mode network after *d*-amphetamine stimulation using this powerful multimodal imaging approach to accurately delineate the effect of a drug on the dopaminergic neurotransmitter system in both the healthy and diseased brain. The gained insight into molecular and neural mechanisms underlying the asymmetric dopamine depletion in a preclinical PD model can have essential implications on a clinical level for diagnosing and treating of this pathology.

3 Material and Methods

3.1 Part I: *In vitro* and *in vivo* evaluation of the binding affinity and selectivity of anle138b derivatives to α-synuclein aggregates

3.1.1 *In vitro* evaluation of anle138b derivatives to α-synuclein aggregates

Since the logP value of anle138b (logP >5.54) was too high, four additional chemical derivatives of anle138b were selected for the *in vitro* saturation binding assays and autoradiography to determine binding specificity and selectivity. The selection was based on the logP value (< 4) to avoid high unspecific binding and blood-brain barrier permeability. In addition, all selected compounds have the chemical properties to be labeled with carbon-11 or fluorine-18 in the next step.

3.1.1.1 Tritiation of Chemical Compounds

All used compounds (anle138b, anle2F4CP, sery383, sery512a, MODAG-001, and MODAG-005) were tritiated from RC Tritec (Teufen, Switzerland), dissolved in ethanol and stored at -80°C until further usage. [^{3}H]PIB was purchased from Vitrax (CA, USA). Table 1 displays each compound's chemical structure, molar activity, and corresponding radiochemical purity determined by high-performance liquid chromatography (HPLC).

Table 1: Overview of the chemical compounds including chemical structures, molar activities, radiochemical purities and logP value

Compound	Chemical structure of unlabeled compound	Molar Activity [GB/µmol]	Radiochemical purity [%]	logP
[^{3}H]anle2F4CP	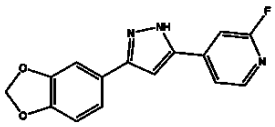	2.8	>98	3.88
[^{3}H]sery512a	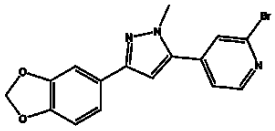	1.17	>99	3.96
[^{3}H]MODAG-005	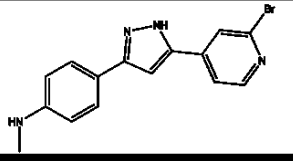	2.96	>98	3.38

3.1.1.2 Fibril Binding Assays

Saturation binding experiments were performed to determine the binding specificity to human recombinant αSYN fibrils. The preparation and characterization of recombinant human αSYN fibrils were performed as described in (89) and kindly provided by our cooperation partner Dr. Felix Schmidt from MODAG GmbH. Recombinant human αSYN fibrils [1 µM/well] were immobilized overnight at 4 °C on 96-well scintillator plates (PerkinElmer, Waltham (MA), USA). Total binding was obtained after incubation with different concentrations of the radiolabeled compound (0.02 nM-48 nM) diluted in buffer (50 mM TrizmaBase, Sigma Aldrich, St. Louis (MO); USA), 10% EtOH, 0.05% Tween20 (Carl Roth, Karlsruhe, Germany), pH 7.4 for one hour. Non-specific binding was determined after adding 10 µM of the corresponding nonradioactive compound to

the tracer solution. Further, increasing concentrations of the radiolabeled compound alone and increasing concentrations of the radiolabeled compound plus 10 µM of the corresponding nonradioactive compound were added together with PBS in separate rows for a later background correction.

The scintillator plates were read out using a Microbeta Scintillation Counter (Perkin Elmer, Waltham (MA), USA). Radioactivity was plotted against the ^{3}H-labeled compound concentration. Data points were fitted using nonlinear regression analysis in GraphPad Prism by fitting total and non-specific binding curves (GraphPad Software, Inc., version 7.03, La Jolla (CA), USA).

3.1.1.3 APPPS1 and APP23 – Mouse Models of cerebral β-amyloidosis

APPPS1 transgenic mice co-express a mutated form of the human APP (*App751* (*KM670/671NL*), the so-called "Swedish mutation") and mutant *Psen1* (*Psen1*(*L166P*)) under the control of *Thy1* promoter. It leads to a suppressed expression of the two transgenes in the cerebellum and, therefore, no amyloid depositions before the 19th month of life. The expression of both transgenes occurs in the rest of the brain. The first amyloid deposits start to appear at two months of age and are only parenchymal amyloid plaques that do not influence cerebral blood flow (90, 91).

Transgenic APP23 mice express a mutated form of the human *APP* (*App751* (*KM670/671NL*)) under the control of murine *Thy1* promoter. First, amyloid deposits appear in the brain parenchyma at around 6 months of age, and the amyloidosis progresses with impaired cerebral blood flow (90, 92).

3.1.1.4 Mouse and Human Brain Tissue

Paraffin-embedded 5 µm mouse brain sections from APPPS1 and APP23 mice were used for autoradiography experiments to test for compound selectivity. In addition, fresh frozen 10 µm slices of one AD case (Braak & Braak 5 or 6, CERAD C) were kindly provided by the Neurobiobank, Munich, and stored at -80 °C until further usage. The Human Research Ethics Committee of the University of Tübingen approved the use of the human tissue samples (Ethics approval number 813/2018BO2).

For the test of compound specificity, fresh frozen 10 µm brain sections of the cortices from one AD case, one PD case, one PSP case, and one control case as well as from the cerebellum of one MSA case and one corresponding control case were kindly provided by Neurobiobank Munich. The human sections were previously characterized by Dr.

Victoria Ruf (Center for Neuropathology and Prion Research, LMU Munich), and tau, Aβ, and αSYN pathology were determined by immunohistochemistry. Relevant information about the sections is illustrated in Table 2. All tissues were stored at -80°C until use.

Table 2: Information of the human sections used in this work for autoradiography experiments.

Disease	Region	Age	Sex	Tau	Aβ	αSYN
Progressive supranuclear palsy	Frontal cortex and marrow camp	66	M	++-+++	-	-
Control	Frontal cortex and marrow camp	64	F	-	-	-
Multiple system atrophy Control	Cerebellum	76	F	-	-	-

3.1.1.5 *In vitro* Autoradiography

Test of compound selectivity

For the comparison of [^{3}H]anle138b, [^{3}H]anle2F4CP, [^{3}H]sery383, [^{3}H]sery512a, [^{3}H]MODAG-001 to the gold standard of amyloid plaques [^{3}H]PIB, mouse brain sections of APPPS1, APP23, and one human AD case were tested in autoradiography studies. Paraffin-embedded 5 µm APPPS1 and APP23 mouse brain sections were first deparaffinized using the following protocol:

1. Xylene 1 – 3 minutes
2. Xylene 2 – 6 minutes
3. 100% ethanol – 3 minutes
4. 100% ethanol – 6 minutes
5. 90% ethanol – 6 minutes
6. 80% ethanol – 6 minutes
7. 70% ethanol – 3 minutes
8. 90% ethanol – 3 minutes
9. Aqua distilled – 3 minutes

The hydrated mouse brain sections and the fresh frozen 10 µm AD brain sections were preincubated for 20 minutes in a buffer containing 50 mM TrizmaBaze (Sigma Aldrich, St. Louis (MO); USA), 10 % Ethanol and 0.05% Tween20 (Carl Roth, Karlsruhe, Germany), pH 7.4. For total binding, sections were incubated in a buffer containing 3 nM of the tritiated compound for one hour. For non-specific binding, consecutive brain sections were incubated in the tracer solution containing a 10 µM excess of the respective unlabeled compound.

Washing was performed thrice for ten minutes each in an ice-cold buffer, and slices were dipped in deionized water for three seconds. After the sections were dried, they were exposed to tritium-sensitive phosphor screens (FUJIFILM Holdings America Corporation, Valhalla (NY), USA) for seven days. Image readout was performed using the phosphor imager Storm 840 Molecular Imager (Molecular Dynamics, Sunnyvale, CA, USA), and the images were displayed and analyzed with ImageJ open source software (US National Institutes of Health, Bethesda (MD), USA).

Test of compound specificity

Autoradiography was performed on different proteinopathy cases to evaluate the specificity of MODAG-001 and MODAG-005 towards αSYN. Fresh frozen brain sections of human PD, PSP, AD, control, as well as MSA and MSA control were preincubated for 20 minutes with 30 mM TrisHCl (Sigma Aldrich, St. Louis (MO); USA), 0.1% BSA (Sigma Aldrich, St. Louis (MO); USA), pH 7.4. For total binding, sections were incubated for one hour in a 3 nM solution of [^{3}H]MODAG-001 and [^{3}H]MODAG-005. For non-specific binding, consecutive brain sections were incubated in the tracer solution containing a 3 µM excess of the respective unlabeled compound.

Washing was performed thrice for ten minutes each in an ice-cold buffer, and slices were dipped in deionized water for three seconds. After the sections were dried, they were exposed to tritium-sensitive phosphor screens (FUJIFILM Holdings America Corporation, Valhalla (NY), USA) for seven days. Image readout was performed using the phosphor imager Storm 840 Molecular Imager (Molecular Dynamics, Sunnyvale, CA, USA), and the images were displayed and analyzed with ImageJ open source software (US National Institutes of Health, Bethesda (MD), USA).

Data quantification

For data quantification, rectangular regions of interest (ROIs) were placed over the tritium standards to obtain a standard curve for quantifying radioactivity concentrations. For the analysis of the mouse and human AD brain sections, ROIs outlined the cortices of the brain sections to calculate total binding and non-specific binding (see Figure 12). Specific binding values were calculated by subtracting non-specific binding values from the total binding values from the total binding values interpolated from the standard curve and converted to pmol/mg.

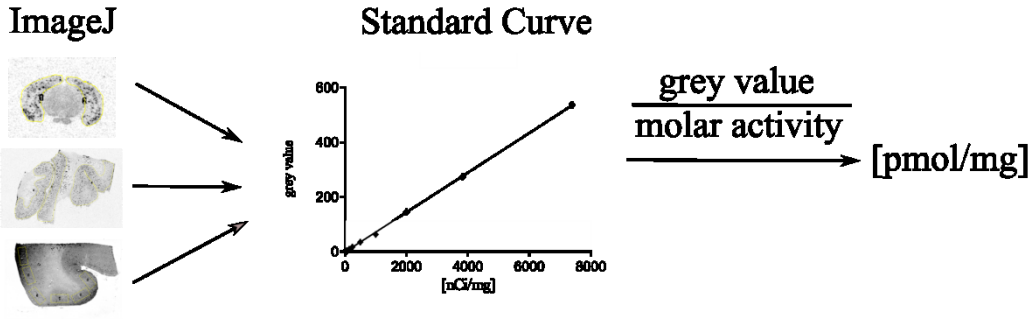

Figure 12: Quantification of autoradiography experiments using ImageJ.

Regions of interest were drawn in pathology-rich regions, interpolated from the generated standard curve, and converted to pmol/mg tissue.

To evaluate MODAG-001 and MODAG-005, five rectangular ROIs per human section (PD, PSP, AD, controls) were placed into the cortex for PD, PSP, AD, and controls to calculate total binding and non-specific binding. In MSA and MSA controls, four rectangular ROIs were placed in the white matter (Figure 13). One rectangular ROI was placed next to the section for background correction.

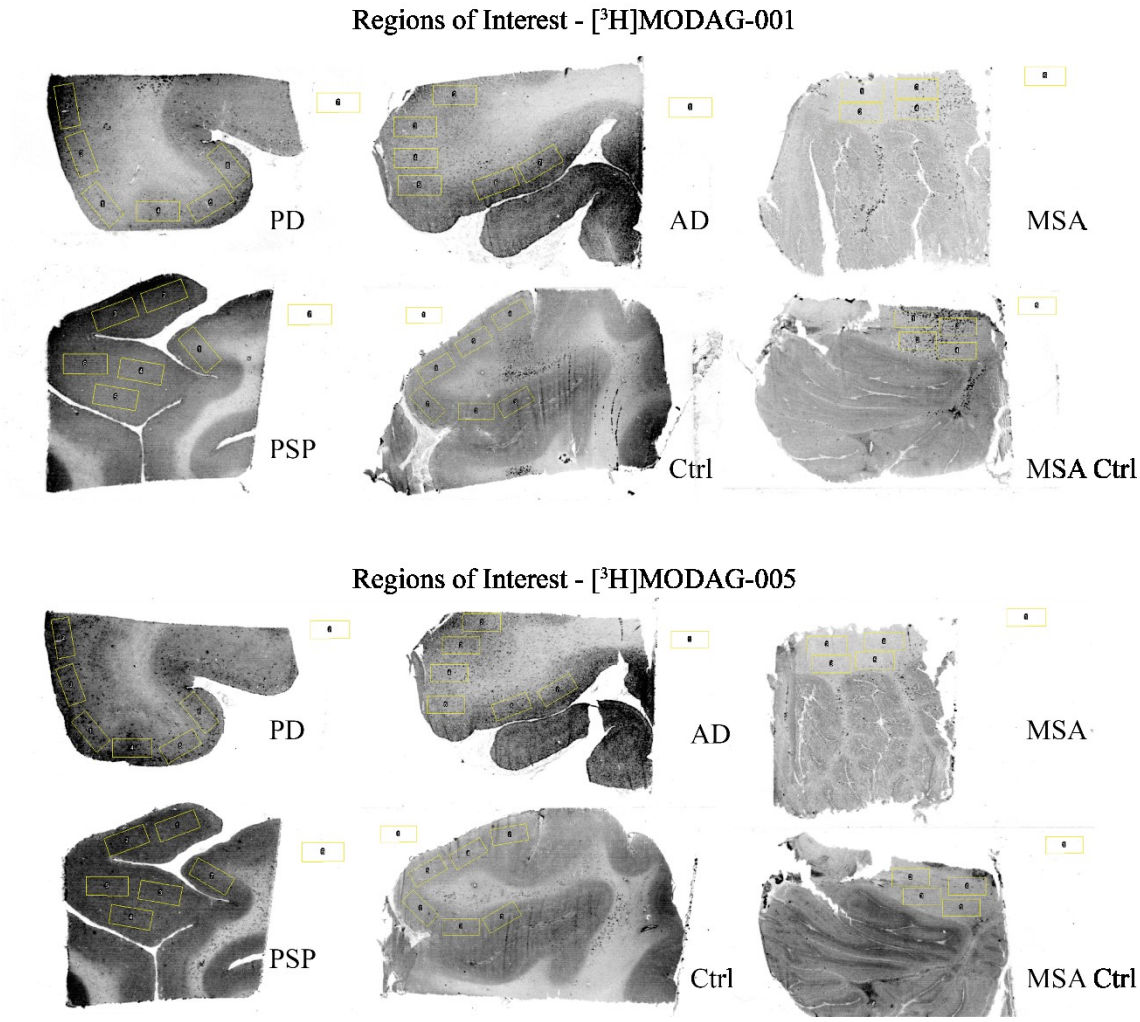

Figure 13: Overview of regions of interest for autoradiography analysis.

For the analysis of MODAG-001 (top two rows) and MODAG-005 (bottom two rows) autoradiography, five rectangular regions of interest per human section were placed into the cortex for PD, PSP, AD and controls. In MSA and MSA controls, four rectangular regions of interest were placed in the white matter. One rectangular region of interest was placed next to the section for background correction. Abbreviations: PD = Parkinson's disease, AD = Alzheimer disease, MSA = Multiple system atrophy, PSP = Progressive supranuclear palsy, Ctrl = Control, MSA Ctrl = Multiple system atrophy control.

3.1.2 *In vivo* evaluation of [^{11}C]MODAG-001 to α-synuclein aggregates

3.1.2.1 Synthesis of [^{11}C]MODAG-001

[^{11}C]MODAG-001 radiolabeling was performed and kindly provided by the Imaging Probe Development Group (Dr. Andreas Maurer) of the Werner Siemens Imaging Center as described in (89).

3.1.2.2 Animals

All animal experiments were conducted in compliance with the European directives on the protection and use of laboratory animals (Council Directive 2010/63/UE) and in addition to the German animal protection law and with the approval (R 2/14 and R 3/19 G) of the local authorities (Regierungspräsidium Tübingen). All mice were maintained in a vivarium on a 12:12 hour light-dark cycle at a temperature of 22°C with 40-60% humidity and given free access to a standard diet and tap water.

Table 3 displays an overview of the age and weight of the mice and the injected and molar activities at the time of injection for the pharmacokinetic and metabolite experiment.

Table 3: Overview of the groups, n-number, age, weight, injected activity and molar activity (mean ± sd) of each group of the pharmacokinetic and metabolite experiment.

Group	N	Age	Weight [g]	Injected activity [MBq]	Molar activity [GBq/µmol]
Metabolite experiment	2	12	19.7 ± 1.3	40.5 ± 13.1	23

A30P mice and corresponding wildtype (WT) mice were kindly provided by Prof. Armin Giese (MODAG GmbH). Table 4 displays an overview of the age and weight of the mice and the injected and molar activities at the time of injection.

Table 4: Overview of the groups, n-number, age, weight, injected activity and molar activity (mean ± sd) of each group of the A30P mice and the age-matched wildtype (WT) mice.

Group	N	Age	Weight [g]	Injected activity [MBq]	Molar activity [GBq/µmol]
$A30P_{young}$	1	23	28.1	13.5	18.4

3.1.2.3 *In vivo* PET imaging and data analysis

All PET experiments were performed on dedicated small animal Inveon PET scanners (Siemens Healthcare, Knoxville (TN), USA). The mice were anesthetized using 1.5-1.7% isoflurane evaporated in 100% oxygen at a flow rate of 0.8 L/min, which was maintained

during the entire experiment. All mice received a tail vein catheter for the [^{11}C]MODAG-001 injection.

For the pharmacokinetic experiment, the mouse was placed on a MR-compatible bed on the PET scanner, which was coupled to a feedback temperature control system keeping the temperature at 37°C, and a whole-body PET scan was performed. For the A30P mice and the age-matched WT mice, two animals were placed head-to-head on a water-heated mouse double bed with an integrated feedback temperature control system, keeping the temperature at 37°C. To minimize motion during the experiment, the mice's heads were secured with ear bars.

Sixty minutes of dynamic PET data were acquired and sinogrammed into 39-time frames (12 × 5 s, 6 × 10 s, 6 × 30 s, 5 × 60 s, and 10 × 300 s). After PET acquisition, an attenuation correction measurement using a cobalt-57 source was performed for 13 minutes. Data were reconstructed into dynamic PET images using OSEM3D for the whole-body scan and FBP for the A30P mice.

For data analysis, the whole-body mouse PET scan was coregistered to the whole-body MR scan, and the volumes of interest of brain, liver, lung, heart, and kidneys were manually drawn using the PMOD software (version 3.2; PMOD Technologies, Zürich, Switzerland). For the A30P mice and the age-matched WT mice, different brain regions (hippocampus, cerebellum, brainstem, cortex, striatum, and thalamus) were extracted using the mouse brain atlas by PMOD (93). Time activity curves (TACs) of each volume of interest are expressed as standard uptake values (SUVs) according to the following equation:

$$SUV = \frac{radioactivity\ concentration}{\frac{injected\ dose}{body\ weight}} \tag{5}$$

Additionally, for the A30P mice and the age-matched wildtype mice, the SUV ratio (SUVR) was calculated using the cortex as the reference region with the following equation:

$$SUVR = \frac{radioactivity\ in\ target\ region}{radioactivity\ in\ reference\ region} \tag{6}$$

3.1.2.4 MR imaging

For the pharmacokinetic experiment, a whole-body anatomical MR scan was performed for coregistration on a 7T Clinscan MR system (Bruker BioSpin GmbH, Ettlingen, Germany). After the PET acquisition, the mouse was kept anesthetized with 1.5 % isoflurane evaporated in 100 % oxygen at a flow rate of 0.8 L/min and placed in the MR system. A whole-body coil was used to obtain the mouse's anatomical MR image, and a TURBO-RARE T2 sequence was carried out.

3.1.2.5 Metabolite analysis

For the metabolite experiments, mice were anesthetized using 1.5-1.7% isoflurane evaporated in 100% oxygen at a flow rate of 0.8 L/min and placed on a heating mat. After placing a tail vein catheter, 40.5 ± 13.1 MBq [^{11}C]MODAG-001 and 25 µL of saline were injected for flushing of the catheter. A blood sample (0.5 mL) was collected by heart puncture at five and 15 minutes after [^{11}C]MODAG-001 injection. Plasma was obtained through centrifugation (17,300 x g at 4°C for 2 minutes) and placed in a 1.5 mL reaction tube on ice for further analysis. In parallel, mice were transcardially perfused (30 mL/min) using 30 mL ice-cold PBS. After surgically removing the brain, one hemisphere was homogenized using a disperser (2 mL Dounce tissue grinder set, Sigma Aldrich Chemie GmbH) together with 1 mL ice-cold PBS and transferred to a 1.5 mL reaction tube on ice for further analysis.

Plasma and brain homogenates were then diluted 1:1 with acetonitrile, mixed, and centrifugated, removing precipitated proteins. The supernatants were analyzed using HPLC.

Data analysis was carried out using GraphPad Prism (GraphPad Software, Inc., Version 7.03, La Jolla, CA, USA). To remove noise, the median of 5 consecutive data points was calculated as a first step. Then, radioactivity (milli-Arbitrary Units (mAU)) was plotted over time, and the data were analyzed by integration analysis (Area Under Curve (AUC) function in GraphPad).

3.2 Part II: A multimodal imaging approach to link protein aggregation to molecular and functional neuronal changes in an animal model of α-synuclein overexpression

3.2.1 Evaluation of the Variability and Reliability of a Simultaneous [^{11}C]Raclopride-PET/BOLD-fMRI Approach

3.2.1.1 Synthesis of [^{11}C]raclopride

[^{11}C]Raclopride synthesis was performed at the Radiopharmacy of the Werner Siemens Imaging Center as described in (94) with the optimized HPLC conditions of van Laeken et al. (95). The tracer was diluted with water, and the isolated fraction was trapped on a conditioned Strata-X cartridge (Phenomenex, Aschaffenburg, Germany). Then, [^{11}C]raclopride was eluted with 0.5 ml ethanol and further diluted with 5 ml phosphate-buffered saline.

Table 5 displays the mean with standard deviation of the molar activities in GBq/µmol for [^{11}C]raclopride at the start of the acquisition during the test-retest study. Further, the mean plus standard deviation of the injected activity at the start of the acquisition is shown in MBq.

Table 5: Injected activity and molar activity at the start of the acquisition during the test-retest study.

Study	Injected activity [MBq]	Molar activity [GBq/µmol]
Retest	387.3 ± 31.3	86.5 ± 25.5

3.2.1.2 Animals

All animal experiments were conducted in compliance with the European directives on the protection and use of laboratory animals (Council Directive 2010/63/UE) and, following the German animal protection law and with the approval (R 11/20 G) of the local authorities (Regierungspräsidium Tübingen). For the test-retest experiments, eight healthy female Sprague Dawley rats were obtained from Charles River Laboratories

(Sulzfeld, Germany) and scanned twice, four months apart (test: 302.6 ± 13.6 g, retest: 331.1 ± 18.4 g). All animals were maintained in a vivarium on a 12:12 hour light-dark cycle at a temperature of 22°C with 40-60% humidity and given free access to a standard diet and tap water.

3.2.1.3 Animal Preparation

The rats were placed in a knock-out box, and 3% isoflurane evaporated in regular air was delivered for anesthesia induction. Then, all rats were weighed, and the isoflurane concentration was reduced to 2% for further preparation.

Two catheters using 30 G needles were placed into the tail veins: one for the [^{11}C]raclopride bolus plus constant infusion injection and the second for the NaCl injection. Rats were placed on a dedicated small-animal water-heated bed in the PET/MR system. The temperatures of the rats were constantly monitored using a rectal probe and maintained at about 37°C by a feedback-temperature control system. Thirty minutes before the PET/MR acquisition started, the isoflurane level was reduced to 1.3% in regular air and kept constant during the whole experiment.

3.2.1.4 Simultaneous [^{11}C]raclopride-PET/BOLD-fMRI

Simultaneous [^{11}C]raclopride-PET/BOLD-fMRI measurements were acquired on a small animal 7T Clinscan MR system (Bruker BioSpin GmbH, Ettlingen, Germany) with an in-house developed small animal PET insert, the second generation with similar specifications of a PET insert described elsewhere (96). For the MR acquisition, an RF coil (Bruker BioSpin GmbH, Ettlingen, Germany) with an inner diameter of 72 mm for signal transmission and a four-channel rat brain coil (Bruker BioSpin GmbH, Ettlingen, Germany) for signal reception was used. After placing the rat brain in the center FOV using a localizer sequence, magnetic field maps were acquired for local magnetic field homogeneity optimization. Subsequently, a T2* weighted gradient-echo EPI sequence (TR = 2500 ms, TE = 18 ms, 0.25 mm isotropic in-plane resolution, FOV 25 × 23 mm, image size: 92 × 85 × 20 px, slice thickness: 0.8 mm, 20 slices) covering the whole brain was acquired over 100 minutes. Afterward, a T2 TurboRARE sequence (TE = 67.11 ms, TR = 1800 ms, FOV: 40 × 32 × 32 mm, image size: 160 × 128 × 128 px, rare factor: 28, averages: 1) was acquired as an anatomical reference. [^{11}C]raclopride was injected intravenously as a fast bolus (30 s), followed by a constant infusion for 100 minutes. A constant infusion rate of 15 µL/min was programmed with a K_{bol} of 38.7 minutes using an

initial bolus of 84.9 ± 9.3 MBq (test scans) and 96.8 ± 7.8 MBq (retest scans). In total, 339.5 ± 37.2 MBq were injected as an infusion for the test scans and 387.3 ± 31.3 MBq for the retest scans. After 40 minutes, the rats were challenged with 150 µL NaCl (Braun, Melsungen, Germany). An overview of the study setup is illustrated in Figure 14.

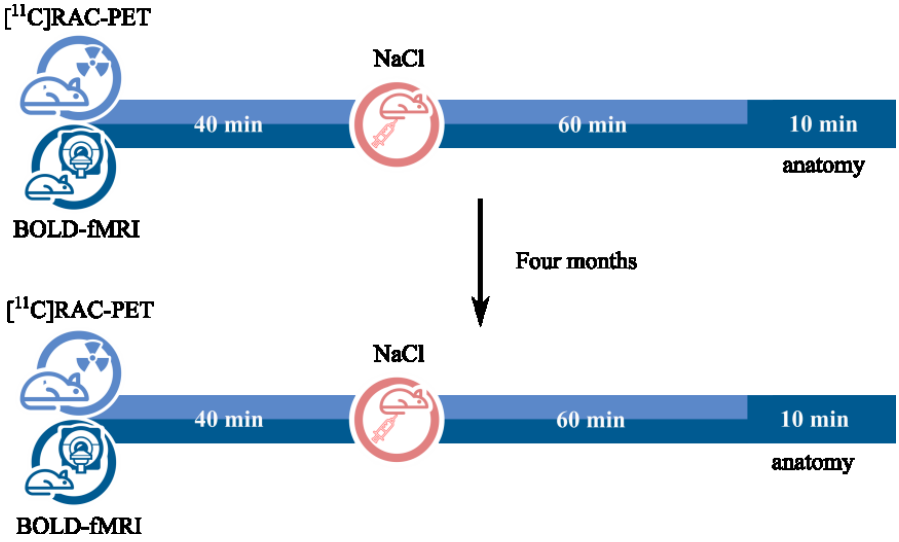

Figure 14: Overview of the study setup of the test-retest experiments.

All rats were scanned with a simultaneous [^{11}C]raclopride-PET/BOLD-fMRI approach applying a NaCl stimulation after 40 minutes. Anatomical images were acquired for every single animal after the fMRI acquisition. The same experiment was repeated four months later. Abbreviations: [^{11}C]RAC = [^{11}C]raclopride, PET = positron emission tomography, BOLD = blood oxygenation level-dependent, fMRI = functional magnetic resonance imaging, min = minutes, NaCl = sodium chloride

3.2.1.5 Preprocessing of [^{11}C]raclopride -PET/BOLD-fMRI Data

Preprocessing was performed as previously described (97). All [^{11}C]raclopride-PET scans were stored as list-mode files and reconstructed dynamically into one-minute frames using an ordered subsets expectation-maximization 2D (OSEM2D) algorithm. PET and fMRI images were converted into the Neuroinformatics Technology Initiative (Nifti) format before preprocessing. The PET and BOLD-fMRI data were preprocessed using Statistical Parametric Mapping (SPM12, Wellcome Trust Centre for Neuroimaging, University College London, London, United Kingdom) in Matlab (Mathworks, Natick, Massachusetts, USA). First, all the PET and fMRI images were realigned, and the corresponding six motion parameters were stored for subsequent motion correction in fMRI. Then, skull stripping was performed on each rat's fMRI and anatomical reference images using binary masks generated in AFNI (Analysis of Functional Neuro Images, Medical College of Wisconsin, USA). Additionally, images containing only extra-cerebral tissues were generated for each fMRI scan, and the first ten principal components of the extra-cerebral

BOLD signal were extracted using AFNI and stored for nuisance regression as described previously (98). Next, each rat's PET and fMRI images were coregistered to their respective anatomical images using SPM12. The anatomical scans were then used to normalize the PET and fMRI datasets to the Schiffer rat brain atlas using the OldNorm algorithm in SPM12 (99). Nuisance regression was performed on the fMRI datasets using the six motion parameters stored after the realignment step and the principal components extracted from the extra-cerebral tissues as described previously (98). Finally, a $1.5 \times 1.5 \times 1.5$ mm^3 full-width-half-maximum (FWHM) Gaussian kernel corresponding to the spatial resolution of the PET insert was applied to all PET and fMRI images for spatial smoothing (100).

3.2.1.6 PET Data Analysis

For the quantification of [^{11}C]raclopride binding of all PET images, the time activity curves (TACs) of 52 brain regions (Table 6) from the Schiffer rat brain atlas were extracted using MarsBaR (MARseille Boite À Région d'Intéret, toolbox for SPM) (101).

The BP_{ND} values of the right and left caudate putamen (CPu) were calculated using equation (7) and the cerebellum as reference region for all rats.

$$BP_{ND} = \frac{V_T(t') - V(t')}{V_{ND}(t')} = \frac{V_T}{V_{ND}} = DVR - 1 = \frac{CPu}{Cer} - 1 \quad (7)$$

V_T/V_{ND} refers to the distribution volume ratio (DVR). The Cer was used as reference region as previous studies have shown that the number of D2 receptors in the cerebellum is negligible and thus is suitable as a reference region for quantifying [^{11}C]raclopride binding in the rat brain (102).

The percent changes in the BP_{ND} of five time intervals T_1 (46-55 min), T_2 (56-65 min), T_3 (66-75 min), T_4 (76-85 min), and T_5 (86-95 min) compared to T_{base} (31-40 min) were calculated using the following equation (8):

$$\%change\_to\_baseline = 100 - (\frac{100}{BP_{ND_{Tbase}}}) * BP_{ND_{T_n}} \quad (8)$$

where $BP_{NDTbase}$ represents the mean BP_{ND} value of the CPu of T_{base} and BP_{NDTn} represents the mean BP_{ND} value of the CPu of T_1, T_2, T_3, T_4 or T_5. The five minutes after the NaCl stimulation were discarded to avoid flow effects. One sample t-test to zero was performed for the CPu percent change of T_1, T_2, T_3, T_4 or T_5 for the test and the retest group.

Furthermore, paired t-tests of the CPu percent changes between the test and the retest group were performed.

Between and Within PET Scan Variability

The variability, which is a measure of the reproducibility of the data, between the test and retest PET scans was calculated with the following equation (9) according to (103):

$$VAR = \frac{|BP_{ND}(CPu)_{retest} - BP_{ND}(CPu)_{test}|}{0.5 * (BP_{ND}(CPu)_{test} + BP_{ND}(CPu)_{retest})} \quad (9)$$

where $BP_{ND}(\mathrm{CPu})_{\mathrm{test}}$ and $BP_{ND}(\mathrm{CPu})_{\mathrm{retest}}$ represent the mean BP_{ND} values of six different time intervals for the CPu between the test and retest scan: T_{base} (31-40 min), T_1 (46-55 min), T_2 (56- 65 min), T_3 (66-75 min), T_4 (76-85 min) and T_5 (86-95 min).

For the variability within the scans, eight test and eight retest scans were combined resulting in a total of 16 scans. The calculation was performed using the following equation (10):

$$VAR = \frac{\left|BP_{ND}(CPu)_{T_n} - BP_{ND}(CPu)_{T_{Base}}\right|}{0.5 * (BP_{ND}(CPu)_{T_{Base}} + BP_{ND}(CPu)_{T_n})} \quad (10)$$

where $BP_{ND}(CPu)_{Tbase}$ and $BP_{ND}(CPu)_{Tn}$ represent the mean BP_{ND} values of the respective time interval from the CPu within the scans. For the within-scan variability, the CPu BP_{ND} values in five time intervals after NaCl stimulation (T_1 (46-55 min), T_2 (56-65 min), T_3 (66-75 min), T_4 (76-85 min), and T_5 (86-95 min)) were compared to CPu BP_{ND} values at baseline T_{base} (31-40 min). The five-minute interval after the NaCl stimulation was discarded from the analysis due to potential flow effects.

PET reliability

The test-retest reliability of the PET scans, indicating the comparability between the results of consecutive measurements, was calculated using one-way ANOVA using the following equation (11) according to (103):

$$RL = \frac{STDB^2}{(STDB^2 + STDW^2)} \quad (11)$$

where *STDB* is the standard deviation between the scans of the mean CPu BP_{ND} values and STDW is the standard deviation within the scans of the mean CPu BP_{ND} values.

3.2.1.7 fMRI Data Analysis

Between and Within Scan Reliability

The analysis of PET always results in quantitative values, which then can be compared between two measurements. With BOLD-fMRI, signal fluctuations are measured, which are not quantifiable. Therefore, only changes can be compared, not quantitative values, using Pearson's r.

For all fMRI images, the time courses of 52 brain regions (Table 6) from the Schiffer rat brain atlas were extracted using MarsBaR (MARseille Boite À Région d'Intéret, toolbox for SPM) (101).

To assess between-scan reliability, pairwise Pearson's r correlations were calculated between all 52 regions, resulting in a 52 x 52 matrix for six different time intervals: T_{base} (31-40 min), T_1 (46-55 min), T_2 (56-65 min), T_3 (66-75 min), T_4 (76-85 min) and T_5 (86-95 min). This was performed separately for the test and the retest scans. In a second step, Pearson's r was calculated between the test and retest time intervals to determine the reliability.

For the within-scan reliability calculations, the eight test and the eight retest scans were combined in one group resulting in a total of 16 scans. First, the Pearson's r correlation coefficients were evaluated for 52 brain regions of six-time intervals: T_{base} (31-40 min), T_1 (46-55 min), T_2 (56-65 min), T_3 (66-75 min), T_4 (76-85 min) and T_5 (86-95 min). Second, Pearson's r was calculated within the scans comparing T_{base} with T_1, T_2, T_3, T_4, and T_5. The five minutes after the NaCl stimulation were rejected.

The Pearson's r was calculated using equation (12):

$$r = \frac{\sum_{i=1}^{n}(x_i - x)\,(y_i - y)}{\sqrt{[\sum_{i=1}^{n}(x_i - \bar{x})^2][\sum_{i=1}^{n}(y_i - \bar{y})^2]}} \qquad (12)$$

where x_i and y_i represent the values of the scans for the i^{th} animal. It takes the value in the range of -1 and 1 and can be interpreted as the following:

1. 0.90 to 1.00: Very high positive correlation
2. 0.70 to 0.90: High positive correlation
3. 0.50 to 0.70: Moderate positive correlation
4. 0.30 to 0.50: Low positive correlation
5. 0.30 to -0.30: negligible correlation
6. -0.30 to -0.50: low negative correlation

7. -0.50 to -0.70: moderate negative correlation
8. -0.70 to -0.90: high negative correlation
9. -0.90 to -1.00: very high negative correlation

Table 6: 52 brain regions of interest listed from the Schiffer rat brain atlas including their respective volumes and abbreviations.

Brain region (ROI)	Hemisphere	ROI volume [mm³]	Position on correlation matrix	Abbreviation
	right		2	
	right		4	
	right		6	
	right		8	
	right		10	
	right		12	
	right		14	
	right		16	
	right		18	
	right		20	
	right		22	
	right		24	
	right		26	
	right		28	
	right		30	
	right		32	
	right		34	
	right		36	
	right		38	
	right		40	
	right		42	
	right		44	
	right		46	
	right		48	
	right		50	
	right		52	

3.2.2 Investigation of Molecular and Functional Changes in an α-synuclein Rat Model of Parkinson's disease

3.2.2.1 Synthesis of [^{11}C]raclopride

[^{11}C]raclopride synthesis was performed as described in 3.2.1.1.

Table 7 displays the mean with standard deviation of the molar activities in GBq/µmol for [^{11}C]raclopride at the start of the acquisition for each group of the study. Further, the mean plus standard deviation of the injected activity is shown in MBq.

3.2.2.2 Animals

All animal experiments were conducted in compliance with the European directives on the protection and use of laboratory animals (Council Directive 2010/63/UE) and in addition to the German animal protection law and with the approval (R 11/20 G) of the local authorities (Regierungspräsidium Tübingen). For the AAV-study, 80 healthy female Sprague Dawley rats were obtained from Charles River Laboratories (Sulzfeld, Germany). These rats were assigned to four different groups (Table 7). All rats were maintained in a vivarium on a 12:12 hour light-dark cycle at a temperature of 22°C with 40-60% humidity and given free access to a standard diet and tap water.

Table 7: Overview of the group names, applied challenge, n-number, weight injected and molar activity (mean ± sd) of each group.

Group	Challenge	N	Weight [g]	Injected activity [MBq]	Molar activity [GBq/µmol]
Control	*d*-AMPH	20	320.0 ± 20.6	427.8 ± 14.5	75.3 ± 19.8
AAV-αSYN	*d*-AMPH	22	333.2 ±27.3	404.5 ± 30.7	144.7 ± 52.3

3.2.2.3 Surgical Procedure of Viral Vector Injections

AAV-αSYN and AAV-GFP ($5.8 \times 10^{13} – 6.6 \times 10^{13}$ genome copies per µL) were kindly provided by Deniz Kirik (Lund University, Sweden). The viral vectors were injected five months before the simultaneous PET/fMRI measurements. The rats were anesthetized by i.p. injection of 1 mL/kg of a mixture of fentanyl (0.005 mg/kg), midazolam (2 mg/kg), and medetomidine (0.15 mg/kg) and placed into a stereotaxic frame. An incision was made to expose bregma and lambda. The needle of a 5 µL Hamilton syringe (Hamilton

Company, Reno (NV), USA) was covered with a small glass capillary (inner diameter: 50 µm). A total volume of 2 µL AAV was injected (0.1 µL/15 s) into the right substantia nigra pars compacta via a drill-hole at the following coordinates according to Paxinos and Watson (104): mediolateral = -2.0 mm, anterior-posterior -5.0 mm, dorsoventral = 7.2 mm. Subsequently, the needle was left in position for five minutes before being slowly withdrawn by 0.2 mm and kept in place for another two minutes. Then, the needle was slowly retracted from the brain (3.5 mm/min), and the incision was closed. After the surgery, an antidote containing atipamezole (0.75 mg/kg) and flumazenil (0.2 mg/kg) was injected subcutaneously to wake the rats from anesthesia. During the procedure, the rats were warmed by a heating pad.

3.2.2.4 Animal Preparation

The rats were placed in a knock-out box, and 3% isoflurane evaporated in regular air was delivered for anesthesia induction. Then, all rats were weighed, and the isoflurane level was reduced to 2% isoflurane evaporated in regular air for further preparation steps.

In the AAV study, three catheters using 30 G needles were placed into the tail veins: one for the [^{11}C]raclopride bolus with constant infusion injection, the second for the *d*-amphetamine injection, and the third for the infusion of the muscle relaxant pancuronium bromide (1 mg/kg/h). The rats were endotracheally intubated using a 16 G plastic tube and connected to a small animal ventilator. The respiration rate was set to 60 breaths per minute. Before positioning the rats in the PET/MR system, a bolus of the pancuronium bromide (2 mg/kg) was injected. The rats were placed on a dedicated small-animal water-heated bed in the PET/MR system. The temperatures of the rats were constantly monitored using a rectal probe and maintained at about 37°C by a feedback-temperature control system. Thirty minutes before the PET/MR acquisition, the isoflurane level was reduced to 1.3% in regular air and kept constant during the experiment. A constant infusion of 1 mg/kg/h pancuronium bromide was started simultaneously with the acquisition. The experimental setup is shown in Figure 15.

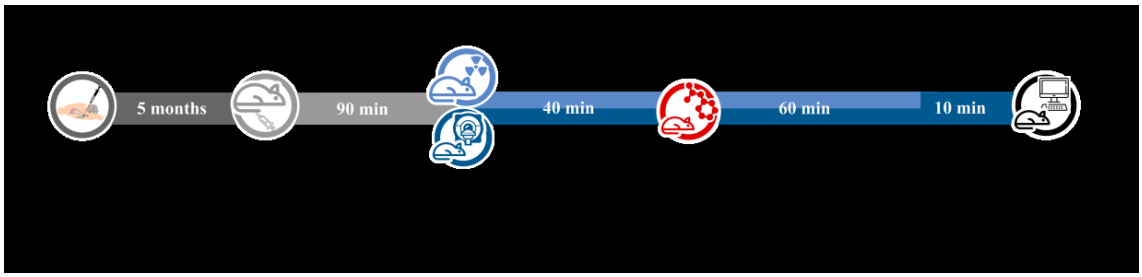

Figure 15: Experimental setup.

Five months after virus injection, the animals were scanned with a simultaneous [^{11}C]raclopride-PET/BOLD-fMRI approach applying either a NaCl or *d*-amphetamine (0.5 mg/kg) stimulation at 40 minutes after injection. Anatomical images were acquired for every single animal after the PET/fMRI acquisition. Abbreviations: AAV = adeno-associated virus, αSYN = α-synuclein, GFP = green fluorescent protein, Co = control, AMPH = *d*-amphetamine, [^{11}C]RAC = [^{11}C]raclopride, PET = positron emission tomography, BOLD = blood oxygenation level-dependent, fMRI = functional magnetic resonance imaging

3.2.2.5 Simultaneous [^{11}C]raclopride-PET/BOLD-fMRI

Simultaneous [^{11}C]raclopride -PET/BOLD-fMRI measurements were acquired as described in 3.2.1.4. After 40 minutes, the rats were challenged with either 150 µL saline (Braun, Melsungen, Germany) for the CoNaCl cohort or *d*-amphetamine (0.5 mg/kg) for the Control, AAV-αSYN, and AAV-GFP cohorts via a bolus injection using a computer-controlled infusion pump.

3.2.2.6 Preprocessing of [^{11}C]raclopride-PET/BOLD-fMRI Data

Quality control led to the exclusion of several rats in the AAV-study due to

1. Motion during the scan (n = 5)
2. Insufficient change between injected and non-injected CPu (<10%) in the AAV-αSYN group (calculated as CPu_{right} BP_{ND}/CPu_{left} BP_{ND} -1) (n = 2),
3. Failure to reach [^{11}C]raclopride tracer equilibrium in the 30-40 minute interval (n = 25) in the caudate putamen (CPu),
4. Died during data acquisition (n = 4),
5. Technical issues (n = 1)
6. Abscess from surgery (n = 2) (Figure 15).

Preprocessing was of the remaining animals was performed as described in 3.2.1.5.

3.2.2.7 PET Data Analysis

The binding potential and the percent change to the baseline of the acquired PET data were calculated as described in 3.2.1.6.

The five minutes after the *d*-amphetamine stimulation were discarded to avoid flow effects. One sample t-test to zero was performed for the CPu percent change of T_1, T_2, and T_3 for CoNaCl, Control, and the AAV-GFP group. Furthermore, paired t-test of the CPu percent change between the CoNaCl and the Control group as well as between the left non-injected and right injected CPu of the AAV-GFP group were performed.

3.2.2.8 fMRI Data Analysis

For all fMRI scans, the time courses of eight ROIs of the dopaminergic network (Table 8) and six ROIs of the default-mode network (Table 9) defined by the Schiffer rat brain atlas were extracted using MarsBaR (MARseille Boite À Région d'Intéret, toolbox for SPM) (101).

Table 8: Brain regions of the dopaminergic network listed from the Schiffer rat brain atlas including their respective volumes and abbreviations.

Brain region (ROI)	Hemisphere	ROI volume [mm³]	Position on correlation matrix	Abbreviation
	right		2	
	right		4	
	right		6	
	right		8	
	right		10	
	right		12	
	right		14	
	right		16	

Functional connectivity was evaluated for each subject by computing Pearson's r correlation coefficients pairwise between all regions, resulting in a 6 × 6 correlation matrix for the default-mode network and an 8 × 8 correlation matrix for the dopaminergic network. After setting self-correlations to zero, the single-subject Pearson's r values were transformed to Fischer's z-scores and averaged to derive group-level mean correlation matrices.

Table 9: Brain regions of the default-mode network listed from the Schiffer rat brain atlas, including their respective volumes and abbreviations.

Brain region (ROI)	Hemisphere	ROI volume [mm³]	Position on correlation matrix	Abbreviation
	right		2	
	right		4	
	right		6	
	right		8	
	right		10	
	right		12	

For all four groups, functional connectivity alterations were investigated using paired t-tests to compare all correlations at T_{base} (31-40 min) with the respective values at the three time intervals: T_1 (46-55 min), T_2 (56-65 min), and T_3 (66-75 min) after *d*-amphetamine stimulation. All multiple comparison corrections presented as red circles in the figures were performed using Bonferroni-Holm. Dynamic functional connectivity was also computed using a sliding window approach (105). Briefly, baseline functional connectivity was calculated for the interval comprising the last ten minutes before *d*-amphetamine stimulation. The five minutes following *d*-amphetamine stimulation were discarded due to potential flow effects. Therefore, starting at five minutes following the *d*-amphetamine challenge, ten-minute windows (240 TRs,) were slid in one-minute steps until the end of the scan (50-time windows), and functional connectivity was calculated for each time window to evaluate the temporal dynamics of the effects induced by the *d*-amphetamine challenge. To inspect alterations on node and network levels, nodal and network functional connectivity strengths were computed for each time window as the sum of all edges comprising the respective node or network during the interval. Paired t-tests were then calculated to detect significant changes in node and network strengths between the baseline functional connectivity T_{base} and the respective time windows T_1, T_2, and T_3 after the stimulation. Significant edge alterations were depicted using the BrainNet Viewer toolbox (106).

4 Results

4.1 Part I: *In vitro* and *in vivo* evaluation of the binding affinity and selectivity of anle138b derivatives to α-synuclein aggregates

Results described in the following subsection have been partially incorporated into the following publication:

Kuebler L[*], Buss S[*], Leonov A[*], Ryazanov S[*], Schmidt F[*], Maurer A, Weckbecker D, Landau AM, Lillethorup TP, Bleher D, Saw RS, Pichler BJ, Griesinger C, Giese A, Herfert K. [^{11}C]MODAG-001-towards a PET tracer targeting α-synuclein aggregates. Eur J Nucl Med Mol Imaging. 2021 Jun;48(6):1759-1772. doi: 10.1007/s00259-020-05133-x. Epub 2020 Dec 28. PMID: 33369690; PMCID: PMC8113290.

[*] contributed equally

4.1.1 Fibril Binding Assay

Saturation binding assays were performed to determine the binding affinity of [^{3}H]anle138b and its structural derivatives to human recombinant αSYN fibrils. The saturation binding curves are shown until a concentration of 24 nM in Figure 16. At higher concentrations of 48 nM, the values fluctuated strongly and were excluded from the fit for all compounds.

We observed the highest binding affinity for [^{3}H]MODAG-001 (K_d = 5.5 ± 2.1 nM) and [^{3}H]anle2F4CP (K_d = 8.9 ± 2.1 nM), moderate binding affinity for [^{3}H]sery383 (K_d = 12.4 ± 3.9 nM) and [^{3}H]anle138b (K_d = 18.6 ± 8.1 nM) and a low binding affinity for [^{3}H]sery512a (K_d = 35.2 ± 12.2 nM) towards αSYN fibrils (Figure 16). B_{max} values of all five compounds were very low in this study, revealing a low number of binding sites at the αSYN fibrils.

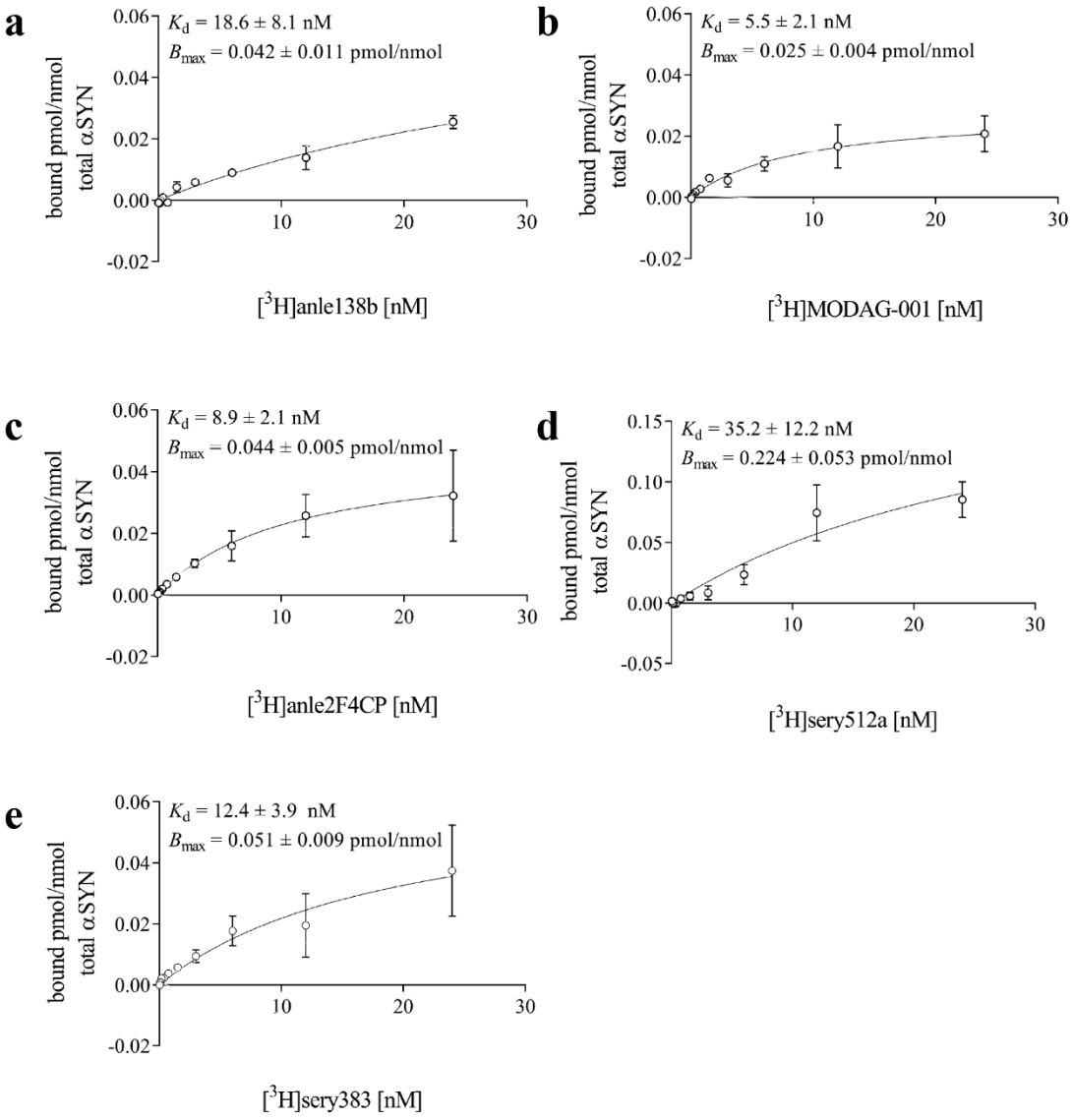

Figure 16: Determination of the binding affinity to human recombinant α-synuclein fibrils using saturation binding experiments.

The graphs show specific binding as well as the corresponding K_d and B_{max} values for (a) [^{3}H]anle138b, (b) [^{3}H]MODAG-001, (c) [^{3}H]anle2F4CP, (d) [^{3}H]sery383 and (e) [^{3}H]sery512a. For all the experiments a concentration of 1 µM α-synuclein fibrils was used. Non-specific binding was determined in the presence of 10 µM of the corresponding nonradioactive compound.

4.1.2 [^{3}H]MODAG-001 – Autoradiography

The selectivity of [^{3}H]anle138b and its structural derivatives for αSYN over Aβ aggregates was determined in brain tissue of two amyloidosis mouse models (APP23, APPPS1) and brain tissue from one human AD case and compared to [^{3}H]PIB, the gold standard amyloid tracer. The results of the autoradiography experiments reveal [^{3}H]PIB binding values of 34.4 ± 6.1 pmol/mg in the APPPS1 mouse model (Figure 17),

30.0 ± 6.5 pmol/mg in the APP23 mouse model (Figure 18) and 14.9 ± 3.7 pmol/mg in tissue sections of human AD (Figure 19). Specific binding was also observed for all five compounds tested. However, the values were between 5 to 14-fold lower than [^{3}H]PIB. The highest target-to-background ratios (low non-specific binding) were obtained for [^{3}H]MODAG-001 and [^{3}H]anle2F4CP. [^{3}H]sery512a showed the lowest binding to Aβ plaques in AD mice models and human AD brain sections.

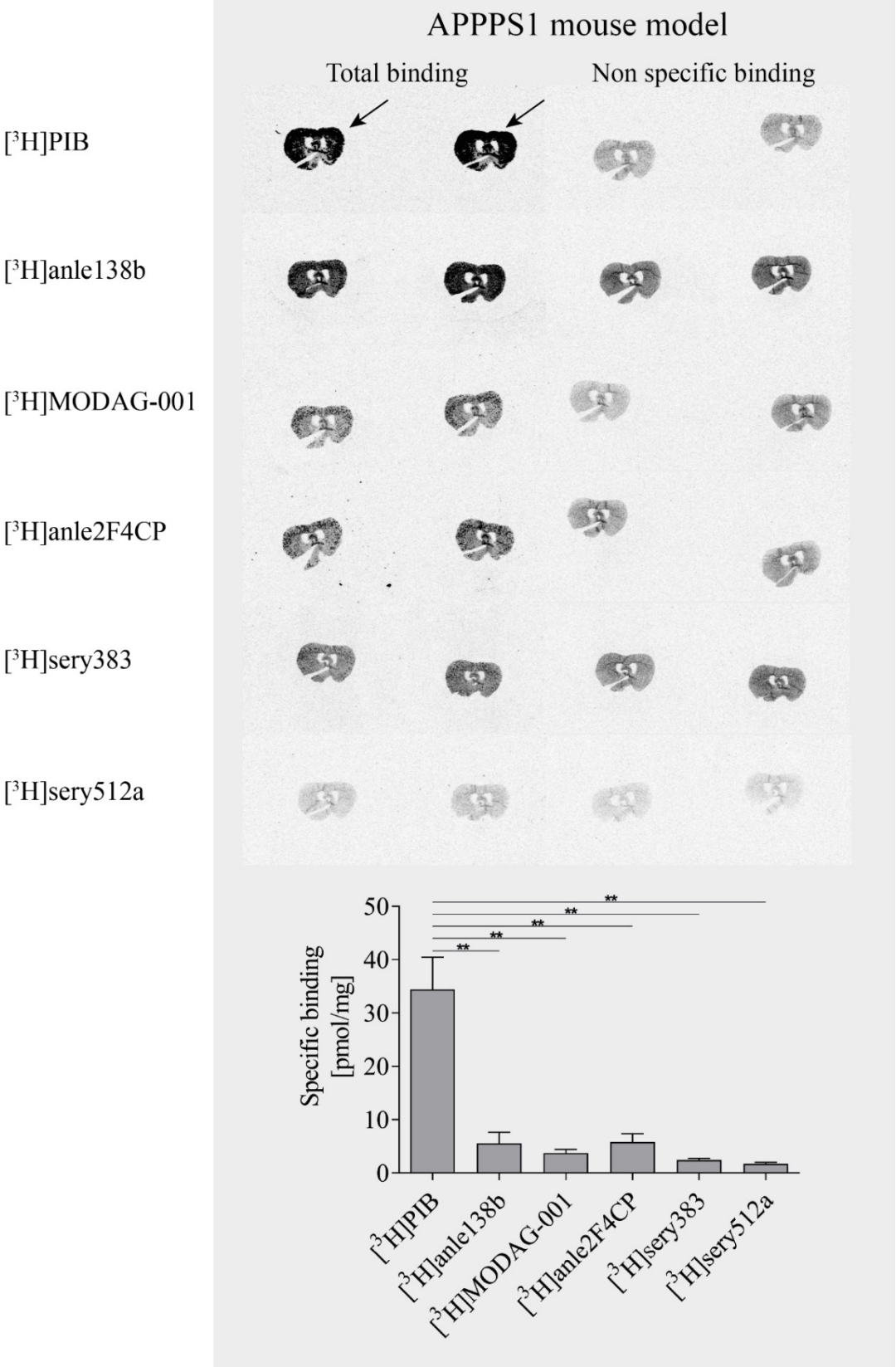

Figure 17: *In vitro* autoradiography on APPPS1 mice brain tissue sections to determine binding to Aβ aggregates.

Images show total and non-specific binding of [^{3}H]PIB, [^{3}H]anle138b, [^{3}H]MODAG-001, [^{3}H]anle2F4CP, [^{3}H]sery383 and [^{3}H]sery512a to brain sections The bar graphs illustrate the quantification of the specific tracer binding in respective brain sections in pmol/mg. ** = $p<0.001$

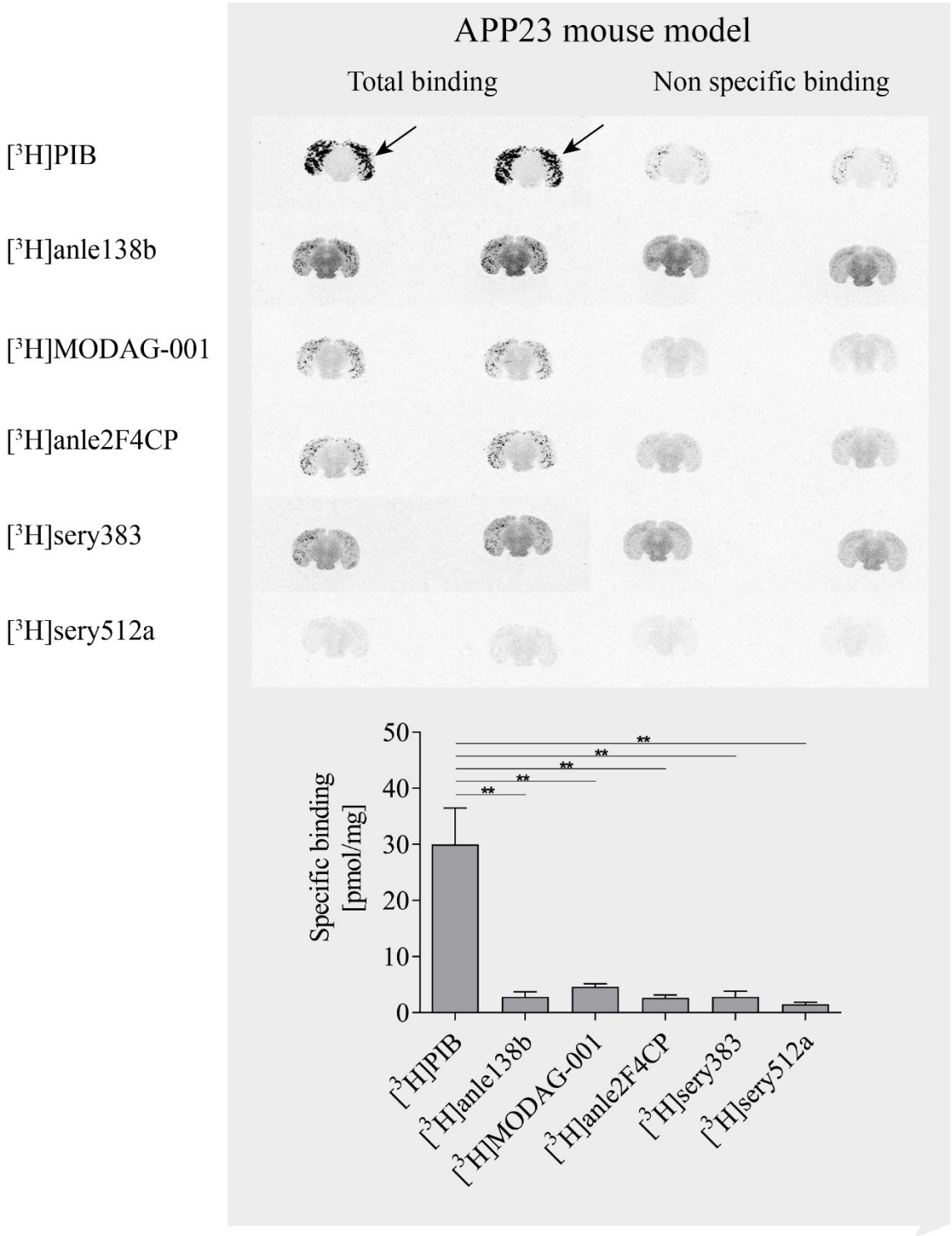

Figure 18: *In vitro* autoradiography on APP23 mice brain tissue sections to determine binding to Aβ aggregates.

Images show total and non-specific binding of [^{3}H]PIB, [^{3}H]anle138b, [^{3}H]MODAG-001, [^{3}H]anle2F4CP, [^{3}H]sery383 and [^{3}H]sery512a to brain sections The bar graphs illustrate the quantification of the specific tracer binding in respective brain sections in pmol/mg. ** = $p<0.001$

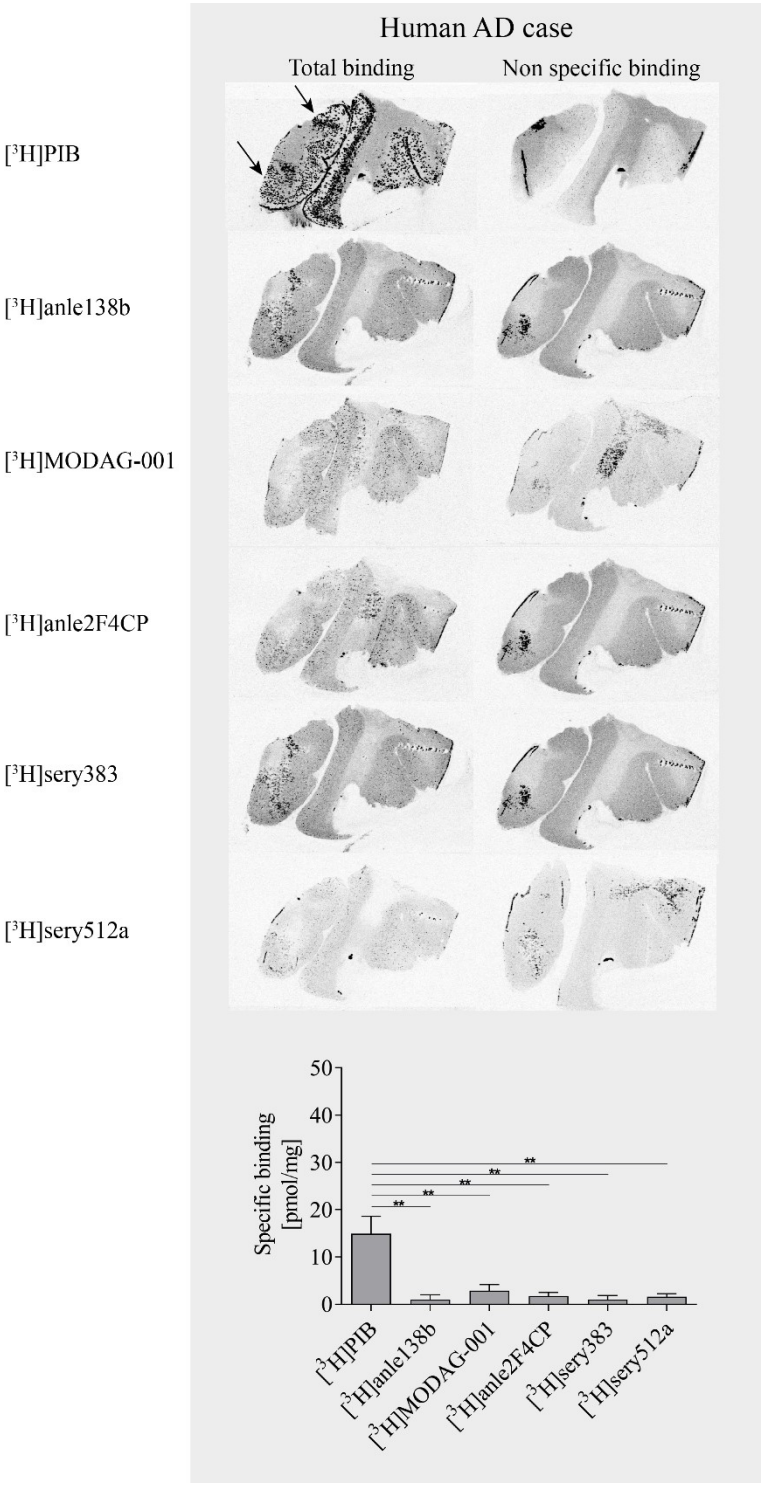

Figure 19: *In vitro* autoradiography on human brain tissue sections of a Alzheimer's disease case to determine binding to Aβ aggregates.

Images show total and non-specific binding of [^{3}H]PIB, [^{3}H]anle138b, [^{3}H]MODAG-001, [^{3}H]anle2F4CP, [^{3}H]sery383 and [^{3}H]sery512a to brain sections The bar graphs illustrate the quantification of the specific tracer binding in respective brain sections in pmol/mg. ** = $p<0.001$

Since [^{3}H]MODAG-001 showed the highest binding affinity towards human recombinant αSYN fibrils, it was further tested on human brain sections of different proteinopathies containing αSYN pathology. Figure 20 shows the total and non-specific binding of [^{3}H]MODAG-001 in brain tissue sections of a PD, PSP, AD, and MSA case and respective control cases. The calculated specific binding showed no significant difference between PD and AD to healthy control cases. Significant differences were observed between the PSP case and the healthy control. However, we observed binding of [^{3}H]MODAG-001 to PD and AD pathology, which could be blocked in the non-specific binding sections (see small boxes in Figure 20 displaying magnifications of black boxes of the PD and AD sections). Further, the MSA control case revealed significant higher [^{3}H]MODAG-001 binding compared to the MSA case.

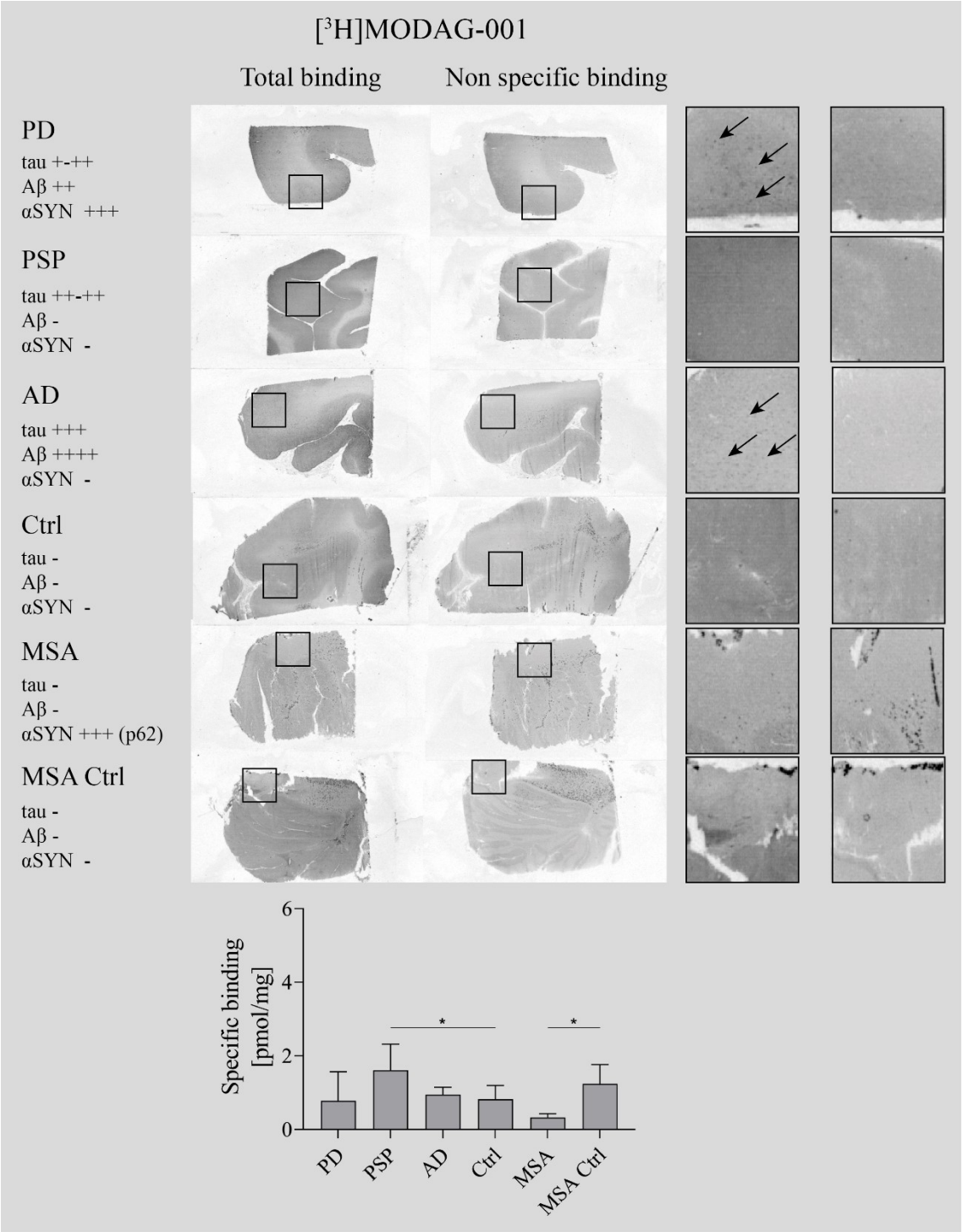

Figure 20: ***In vitro*** **autoradiography on human brain sections of different proteinopathy cases for [^{3}H]MODAG-001.**

Images show total and non-specific binding of [^{3}H]MODAG-001 in brain sections of Parkinson's disease (PD), progressive supranuclear palsy (PSP), Alzheimer's disease (AD), multiple system atrophy (MSA), and respective healthy controls (Ctrl). The bar graph illustrates the quantification of specific tracer binding in respective brain sections in pmol/mg. * = $p<0.05$, black arrows indicate plaques

4.1.3 [^{11}C]MODAG-001 – PET Pharmacokinetics

In vivo, [^{11}C]MODAG-001 PET experiments in healthy mice to determine the pharmacokinetics and biodistribution in different organs were part of the Master thesis of Sabrina Haas, which she performed under my supervision and experimental support. The results are shown in Figure 21.

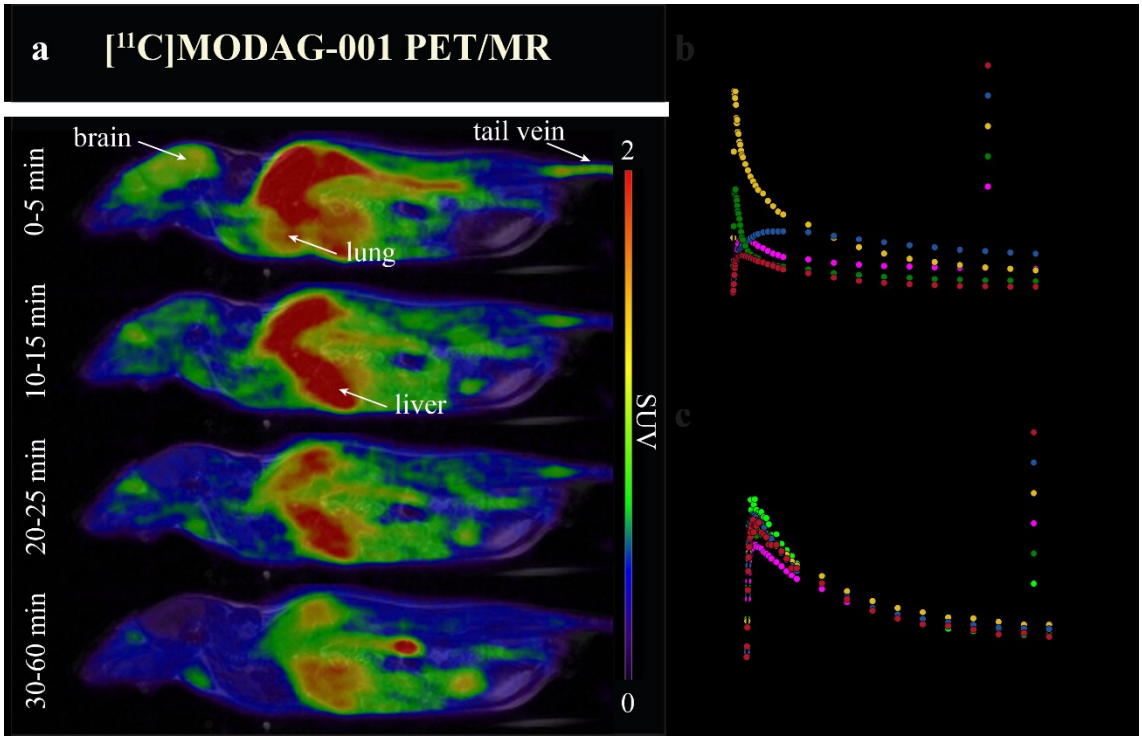

Figure 21: Pharmacokinetic profile of [^{11}C]MODAG-001.
Whole-body sagittal PET/MR images of one mouse summed up at different time points after [^{11}C]MODAG-001 injection (a). The corresponding time activity curves are displayed of different organs (b) and different brain regions (c) indicated as standard uptake value (SUV). Abbreviations: HIP = hippocampus, Cer = cerebellum, BS = brainstem, CTX = cortex, CPu = caudate putamen, THA = thalamus

[^{11}C]MODAG-001 showed an initial tracer peak and fast washout in the lung (SUV = 7.2), the heart (SUV = 3.6), the kidneys (SUV = 1.9), and the brain (SUV = 1.3). The liver showed a slow tracer accumulation over time. Good and rapid brain uptake with an SUV of 1.3 was shown with small regional differences across different brain regions.

4.1.4 [^{11}C]MODAG-001 - Metabolite Analysis

Another experiment investigated the metabolite profile of [^{11}C]MODAG-001 in the mouse brain and plasma. This experiment was also part of the Master thesis of Sabrina Haas performed under my supervision. HPLC of brain homogenates and plasma was performed to determine radio-metabolite formation. The resulting chromatograms of the

metabolite analysis in the brain and the plasma at five and 15 minutes after [^{11}C]MODAG-001 injection are displayed in Figure 22.

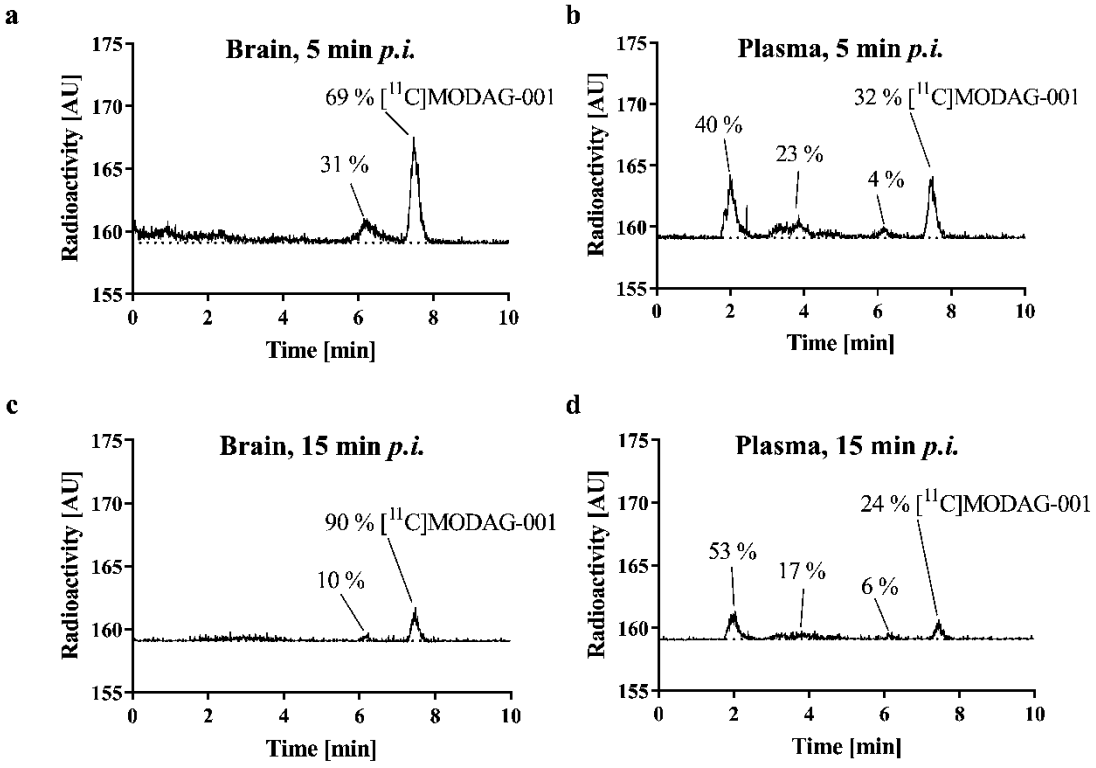

Figure 22: Metabolite profile of [^{11}C]MODAG-001.

Images show the metabolite profiles of the brain five minutes (a) and 15 minutes (b) as well as the metabolite profiles of the plasma five minutes (c) and 15 minutes (d) after [^{11}C]MODAG-001 injection. Abbreviations: AU = arbitrary units; p.i. = post injectio

The quantitative analysis of the mice revealed one metabolite in the brain with 70% and 90% of [^{11}C]MODAG-001 present in the brain at five and 15 minutes after tracer injection. The metabolite corresponds to the demethylated precursor MODAG-005. Three metabolites were detectable in the plasma, with 32% and 24% of [^{11}C]MODAG-001 present five and 15 minutes after tracer injection.

4.1.5 [^{11}C]MODAG-001 – A30P mouse model

To study the binding of [^{11}C]MODAG-001, PET imaging experiments were conducted in A30P mice with intracellular α-synuclein pathology. Figure 23 shows sagittal brain images (sum of the first 5 minutes) and their corresponding time activity curves for various brain regions of an old A30P mouse (Figure 23 a, b), young A30P mouse (Figure 23 c, d), and an old age-matched WT mouse (Figure 23 e, f). All mice show a fast initial tracer

peak in the brain: old A30P mouse SUV = 1.1-1.6, young A30P mouse SUV = 0.7-1.0, and age-matched WT SUV = 1.4-1.9.

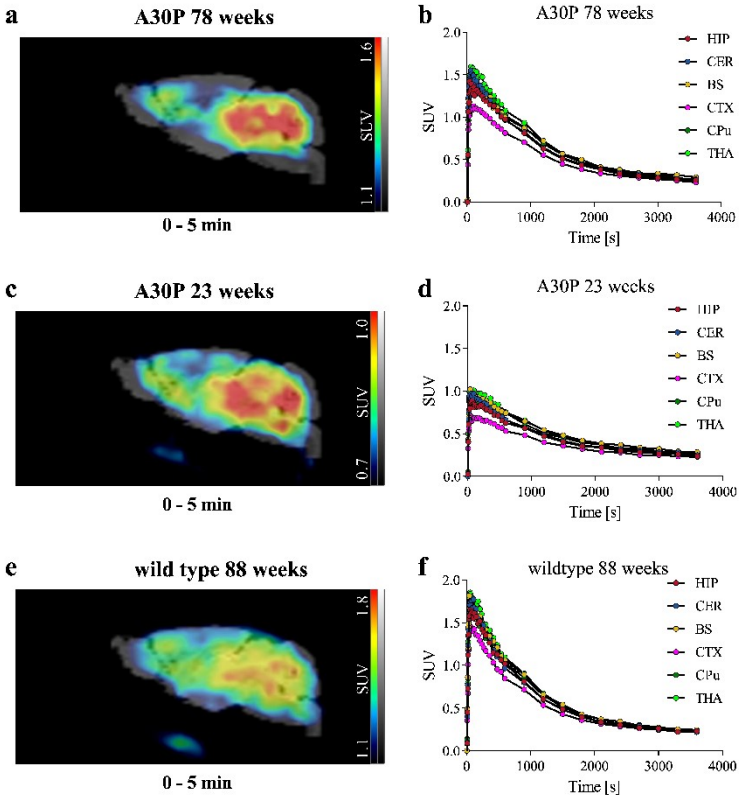

Figure 23: [^{11}C]MODAG-001 brain PET images and time-activity curves in A30P mice and wild type controls.

Tracer distribution is displayed for one old A30P mouse (a, b), one young A30P mouse (c, d) and one old age-matched wildtype mouse (e, f). Abbreviations: HIP= hippocampus; CER = cerebellum, BS = brain-stem, CTX = cortex, CPu = caudate putamen, THA = thalamus

In the old A30P mice, high pathology is expected in the midbrain and brainstem. However, no difference in the SUVR of [^{11}C]MODAG-001 binding could be observed between the old A30P mice, the young A30P mouse, and the age-matched wildtype mice in the brainstem, thalamus, and hippocampus over time (Figure 24 a, b, c). The average SUVR from ten to 60 minutes displayed no significant difference in the brainstem, thalamus, and hippocampus between the old A30P mice, the young A30P mouse, and the age-matched wildtype mice (Figure 24 d, e, f).

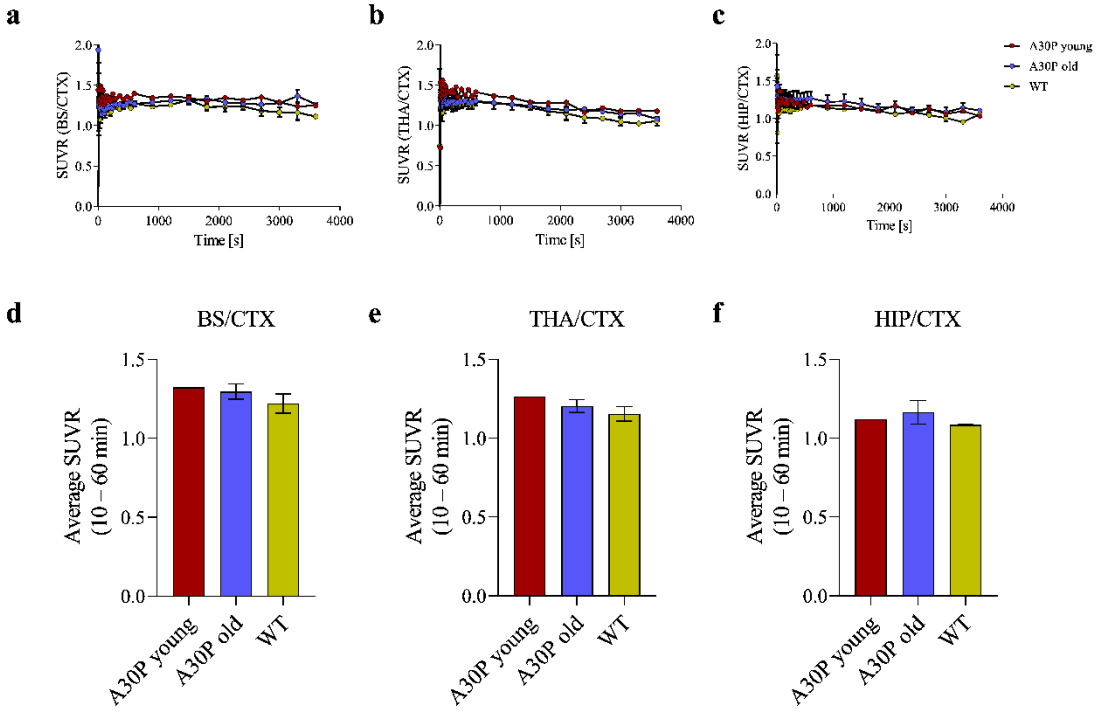

Figure 24: *In vivo* characterization of [^{11}C]MODAG-001 in A30P mice.

Standard uptake value ratio over time for the young and old A30P mice as well as the age-matched wildtype mice in the brainstem (a), thalamus (b) and hippocampus (c) using the cortex as reference region are plotted. Comparison of the average standard uptake value ratio (10-60 minutes) for the young, old A30P mice, and the age-matched wildtype mice between the brainstem (d), thalamus (e) and hippocampus are shown. Abbreviations: SUVR = standard uptake value ratios, BS = brainstem, CTX = cortex, THA = thalamus, HIP= hippocampus, WT = wiltype mice

4.1.6 [^{3}H]MODAG-005 - Autoradiography

As mentioned in 4.1.4, we observed one radio-metabolite crossing the blood-brain barrier, the demethylated precursor MODAG-005. The compound was further labeled with tritium, and its affinity towards human recombinant αSYN fibrils was determined, revealing a very high affinity of < 1 nM towards human recombinant αSYN fibrils. Therefore, autoradiography experiments were repeated with [^{3}H]MODAG-005 in consecutive brain sections of the same proteinopathy cases used for [^{3}H]MODAG-001.

[^{3}H]MODAG-005 (Figure 25) showed an overall higher binding in the PD, PSP, AD, and control case compared to [^{3}H]MODAG-001. [^{3}H]MODAG-005 also showed significant higher binding to the PSP case compared to the healthy control case with 3.6 ± 0.3 pmol/mg. The lowest binding values were revealed for the MSA case (0.02 ± 0.03 pmol/mg). Having a closer look at the PD and AD cases, a binding of [^{3}H]MODAG-005 could be observed in the grey matter being the pathological area of

these diseases. This binding could be blocked for both cases in the non-specific binding sections (see small boxes in Figure 25 displaying magnifications of black boxes of the PD and AD sections).

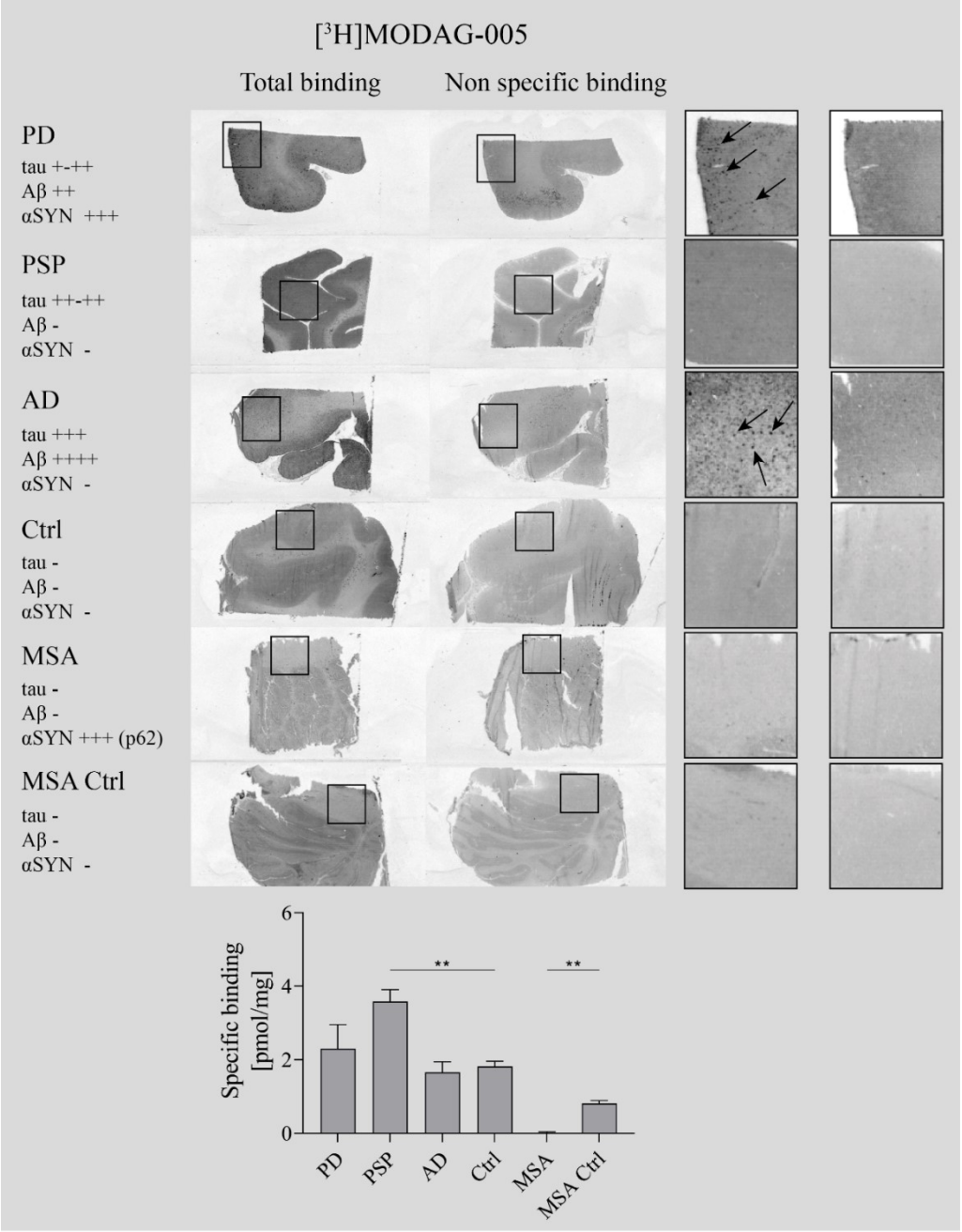

Figure 25: ***In vitro*** **autoradiography on human brain sections of different proteinopathy cases for [^{3}H]MODAG-005.**

Images show total and non-specific binding of [^{3}H]MODAG-005 in brain sections of Parkinson's disease (PD), progressive supranuclear palsy (PSP), Alzheimer's disease (AD), multiple system atrophy (MSA), and respective healthy controls (Ctrl). The bar graph illustrates the quantification of specific tracer binding in respective brain sections in pmol/mg. ** = $p<0.001$, black arrows indicate plaques

4.2 Part II: A multimodal imaging approach to link protein aggregation to molecular and functional neuronal changes in an animal model of α-synuclein overexpression

In the second part of this dissertation, the impact of αSYN pathology on dopamine release dynamics after *d*-amphetamine was investigated in an AAV-αSYN overexpression rat model using a simultaneous [^{11}C]raclopride-PET/BOLD-fMRI approach. For this purpose, test-retest experiments were performed to validate the newly established measurement protocols and then applied in an animal model.

The results of these experiments have already been compiled in a draft for publication.

4.2.1 Evaluation of the Variability and Reliability of a Simultaneous [^{11}C]Raclopride-PET/BOLD-fMRI Approach

The following subchapters present a detailed evaluation of the PET/fMRI protocol used in this dissertation.

4.2.1.1 Time-Activity Curves and Binding Potential

In Figure 26 a and b, the [^{11}C]raclopride mean decay-corrected TACs of the CPu and the Cer after injection with the bolus plus constant infusion protocol and the corresponding BP_{ND}s over time are presented for the test (n = 7) and the retest (n = 8) group. Only seven rats were included in the test group since the infusion pump of the tracer stopped 20 minutes before the end of the PET acquisition in one rat. [^{11}C]Raclopride TACs of both groups constantly increased over 100 minutes. The BP_{ND} curves became noisier in later time intervals due to the short half-life of [^{11}C]raclopride. Equilibrium between the target (CPu) and reference (Cer) region was reached between 31-40 minutes (T_{base}) in the test and retest group (1.8 ± 0.2 and 1.6 ± 0.1, respectively). Calculating the percent change of BP_{ND} values for T_1, T_2, T_3, T_4, and T_5 to each group's baseline (Figure 26 c) revealed no significant decrease between the test and retest groups in any time interval. After performing the one-sample t-test to zero, the test group indicated a significant reduction in T_4 ($p = 0.04$), and the retest group in T_2, T_3, and T_5 ($p = 0.01$, $p = 0.01$, $p = 0.02$, respectively).

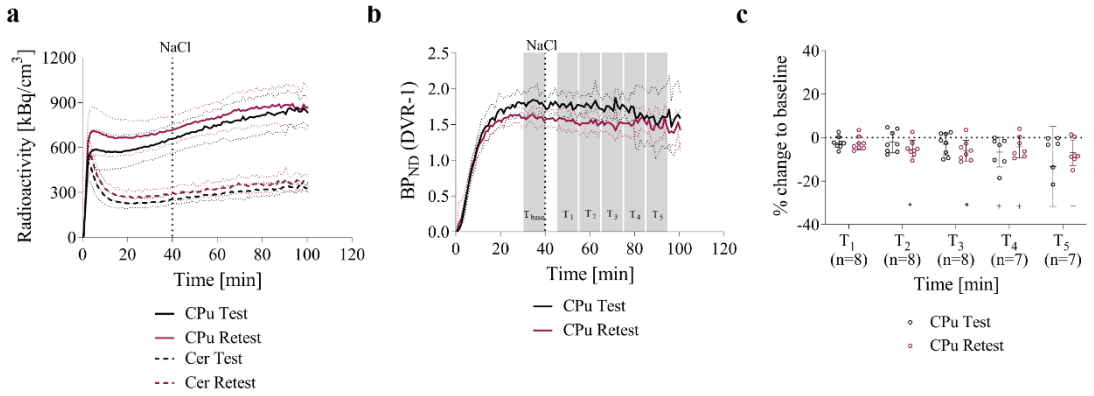

Figure 26: [^{11}C]Raclopride test-retest experiments using a bolus plus constant infusion protocol.
(a) The mean decay corrected time activity curves of the test and retest group are plotted over time for the caudate putamen and the cerebellum. (b) Corresponding binding potentials with the caudate putamen as target region and the cerebellum as reference region calculated as DVR-1 over time are shown for the baseline and five post NaCl time intervals. (c) The percent change to baseline T_{base} in the caudate putamen of the time intervals T_1, T_2, T_3, T_4 and T_5 after the NaCl stimulation are shown for the test and retest group. Abbreviations: CPu = caudate putamen, Cer = cerebellum, BP_{ND} = binding potential non displaceable, DVR-1 = distribution volume ratio minus one, T_{base} = 31-40 minutes, T_1 = 46-55 minutes, T_2 = 56-65 minutes, T_3 = 66-75 minutes, T_4 = 56-65 minutes, T_5 = 66-75 minutes, + = $p<0.05$, * = $p<0.01$

4.2.1.2 Test-Retest Variability and Reliability – Between Scans

The PET test–retest variability and reliability values of [^{11}C]raclopride, as well as the fMRI reliability were determined from eight healthy rats scanned twice four months apart. The variability of the mean CPu BP_{ND} values of six different time intervals (T_{base}, T_1, T_2, T_3, T_4, and T_5) between the scans are summarized in Table 10 a.

The test–retest variability of the mean CPu BP_{ND} values between the scans was 13.0 ± 6.3% at T_{base} increasing up to 20.8 ± 14.2% at T_5. Variability between test-retest scans for T_4 and T_5 was determined in only seven animals because the infusion pump of the tracer stopped 20 minutes before the end of the PET acquisition in one rat. PET reliability was zero because the mean sum square between subjects was smaller than the mean sum square within subjects. This is the result of the different molar activities between the test (106.5 ± 35.2 GBq/µmol) and retest (86.5 ± 25.5 GBq/µmol) measurement, leading to lower binding values in the retest scans.

For fMRI, the Pearson's r of whole-brain group-mean matrices were generated for each time interval T_1, T_2, T_3, T_4, and T_5 and compared to T_{base}. Table 11 a shows the test-retest fMRI reliability results obtained using Pearson's r resulting in moderate correlations for all time intervals.

Table 10: [^{11}C]Raclopride variability in percent between test-retest scans (a) and within scans (b).
Abbreviations: T_{base} = 31-40 minutes, T_1 = 46-55minutes, T_2 = 56-65minutes, T_3 = 66-75minutes, T_4 = 76-85minutes and T_5 = 86-95minutes

a	CPu variability between test-retest scans	b	CPu variability within scans
T_1	13.9 ± 9.4 % (n=8)	T_{base} vs. T_2	5.4 ± 2.5 % (n=16)
T_3	13.6 ± 9.7 % (n=8)	T_{base} vs. T_4	6.2 ± 5.5 % (n=15)
T_5	20.8 ± 14.2 % (n=7)		

4.2.1.3 Test-Retest Variability and Reliability – Within Scans

To assess PET CPu variability and fMRI reliability, we combined the test-retest scans, resulting in 16 total scans. The mean CPu BP_{ND} values of T_1, T_2, T_3, T_4, and T_5 time intervals were compared to the mean CPu BP_{ND} values of the baseline time interval T_{base}. The PET test–retest CPu variability within scans was 3.4 ± 1.7% between T_{base} and T_1, increasing to 11.4 ± 17.1% between T_{base} and T_5. The CPu variability within scans of all five time intervals compared to T_{base} is listed in Table 10 b.

For fMRI, the Pearson's r of whole-brain group-mean matrices were generated for each time interval T_1, T_2, T_3, T_4, and T_5 and compared to T_{base}. The Pearson's r of each time interval is listed in Table 11 b. The quantification of the within-scan fMRI reliability showed good correlations with a Pearson's r value of 0.8 ± 0.1 between T_{base} and T_1 and the lowest Pearson's r value of 0.7 ± 0.2 between T_{base} and T_4.

Table 11: **BOLD-fMRI reliability represented as the Pearson's r between (a) and within test-retest scans (b).**

Abbreviations: T_{base} = 31-40 minutes, T_1 = 46-55 minutes, T_2 = 56-65 minutes, T_3 = 66-75 minutes, T_4 = 76-85 minutes and T_5 = 86-95 minutes

a	Reliability between test-retest scans	b	Reliability within scans
T_1	0.5 ± 0.1 (n=8)	T_{base} vs. T_2	0.7 ± 0.1 (n=16)
T_3	0.6 ±0.2 (n=8)	T_{base} vs. T_4	0.7 ± 0.2 (n=16)
T_5	0.5 ± 0.1 (n=8)		

4.2.2 Investigation of Molecular and Functional Changes in an α-synuclein Rat Model of Parkinson's disease

The following subchapters describe the results of the simultaneous [^{11}C]raclopride-PET/phMRI study investigating dopamine modulation induced by *d*-amphetamine and its impact on functional connectivity in healthy rats and in a rat model of PD. In particular, the dopaminergic network, including the four different dopaminergic pathways and the default-mode network, were explored.

4.2.2.1 *D*-Amphetamine Decreases [^{11}C]Raclopride Binding in the Caudate Putamen and Cerebellum

In Figure 27 a and b, the [^{11}C]raclopride mean decay-corrected TACs of the CPu (target region with high dopamine concentrations) and the Cer (reference region) and the corresponding BP_{ND}s over time are presented for the CoNaCl (n = 8) and the Control (n = 10) group. [^{11}C]RAC TACs of the CoNaCl group showed a constant increase over the whole time of 80 minutes, whereas the Control group showed a decrease of the [^{11}C]raclopride activity in the CPu and Cer five minutes after the *d*-amphetamine (0.5 mg/kg) stimulation. The decrease in [^{11}C]raclopride activity was also observed in other dopamine-rich regions, such as the thalamus or the amygdala (data not shown) in the *d*-amphetamine-stimulated control group. Equilibrium of the BP_{ND} was reached between 31-40 minutes (T_{base}) in the CoNaCl and Control group (1.6 ± 0.4 and 1.3 ± 0.1, respectively) (Figure 27 b). The BP_{ND}*s* after *d*-amphetamine stimulation of the Control group decreased within the time intervals T_1 (46-55 minutes), T_2 (56-65 minutes), and T_3 (66-75 minutes). However, this decrease was only significant at the last time point when compared to the NaCl stimulated Control group (-3.4 ± 4.0% and -9.4 ± 4.3%, respectively, p = 0.008) (Figure 27 c). When calculating D2 receptor binding in the CPu, we normalized to the cerebellum as a reference region under the assumption that it is free of D_2 receptors. However, our data clearly show decreased cerebellar TAC after the *d*-amphetamine challenge. Thus, receptor binding in the cerebellum is overestimated if the cerebellum is used as a reference region, reducing the sensitivity to quantify small changes in dopamine release. Furthermore, the determination of the molar activity of the tracer showed that the *d*-amphetamine-stimulated rats had been injected with the tracer at an average lower molar activity (Table 7). This leads to a higher occupancy of unlabeled [^{11}C]raclopride at the receptors and reduced binding, as shown in Figure 27 b. This leads to an underestimation of baseline binding and reduced sensitivity to detect small changes in dopamine release.

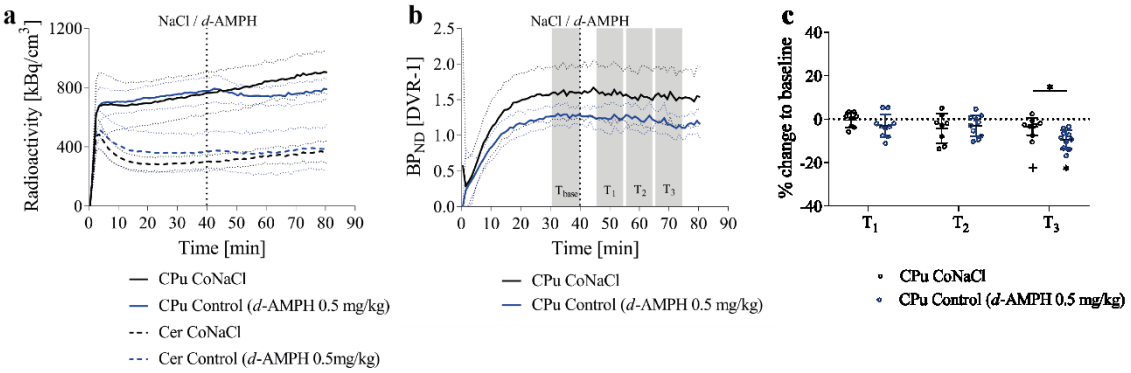

Figure 27: Effect of *d*-amphetamine stimulation on [^{11}C]raclopride PET.

(a) The mean decay corrected time-activity curves of the CoNaCl and Control group are plotted over time for the caudate putamen and the cerebellum. (b) Corresponding binding potentials with the caudate putamen as target region and the cerebellum as reference region calculated as distribution volume ratio-1 over time are shown for the baseline and three post-stimulation time intervals. (c) The percent change to baseline T_{base} in the caudate putamen of the time intervals T_1, T_2, and T_3 after the *d*-amphetamine stimulation are shown for the CoNaCl and Control group. Abbreviations: DVR-1 = distribution volume ratio-1, CPu = caudate putamen, Cer = cerebellum, Co = Control, *d*-AMPH = *d*-amphetamine, BP_{ND} = binding potential non-displaceable, DVR-1 = distribution volume ratio minus one, T_{base} = 31-40 minutes, T_1 = 46-55 minutes, T_2 = 56-65 minutes, T_3 = 66-75 minutes, + = $p<0.05$, * = $p<0.01$

4.2.2.2 [^{11}C]Raclopride Binding Revealed D_2 Receptor Occupancy Changes in AAV-αSYN Rats Compared to AAV-GFP Rats

After injection of [^{11}C]raclopride, the decay-corrected TAC and the dynamic BP_{ND} of the AAV-αSYN group showed an increase in [^{11}C]raclopride binding in the right AAV-αSYN-injected CPu (1.9 ± 0.05) compared to the left non-injected CPu (1.5 ± 0.03) (Figure 28 a, b). The equilibrium between the left CPu and cerebellum was reached after 31 minutes (1.5 ± 0.03), similar to the CoNaCl group, whereas the right αSYN-injected CPu did not reach equilibrium before *d*-amphetamine injection for a reliable receptor quantification (Figure 28 b). Therefore, no statistical analysis of the effects of *d*-amphetamine could be performed for this group (Figure 28 c). In the AAV-GFP group (Figure 28 d, e), no left-right differences could be observed in the TACs and the BP_{ND} of the CPu. The BP_{ND} reached equilibrium after 31 minutes (left non-injected CPu: 1.5 ± 0.02, right AAV-GFP injected CPu 1.5 ± 0.02). One-sample t-tests of the BP_{ND} values to zero indicated significant decreases in the non-injected CPu of the AAV-GFP group at T_2 (-2.8 ± 4.3%, $p = 0.04$) and T_3 (-4.8 ± 4.7%, $p = 0.003$). The right GFP-injected CPu showed a significant decrease in T_3 (-4.9 ± 6.1%, $p = 0.01$) (Figure 28 f).

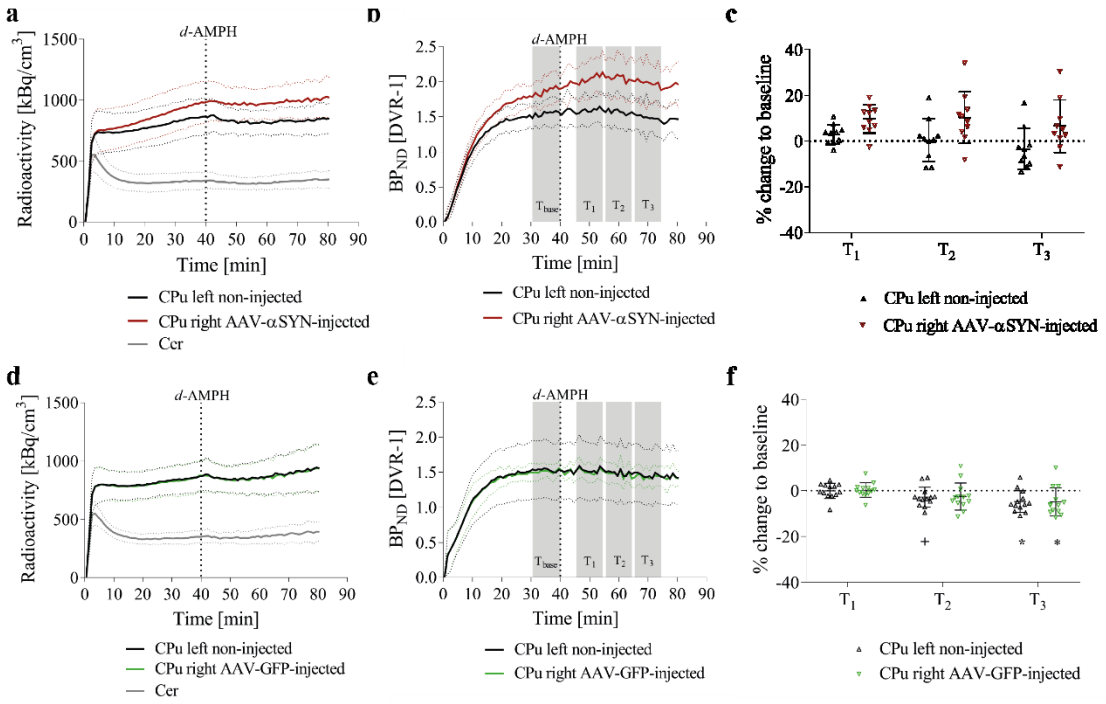

Figure 28: Effect of *d*-amphetamine stimulation on [^{11}C]raclopride PET for the AAV-αSYN and AAV-GFP group.

Mean decay corrected [^{11}C]raclopride time-activity curves of the AAV-αSYN (a) and AAV-GFP (d) group are plotted over time for the non-injected, the injected caudate putamen, and the cerebellum. (b, e) Corresponding binding potentials with the caudate putamen as target region and the cerebellum as reference region calculated as distribution volume ratio-1 over time are shown for the baseline and three post-stimulation time intervals. The percent change in the non-injected and injected caudate putamen of time intervals T_1, T_2, and T_3 after the *d*-amphetamine stimulation compared to baseline T_{base} are shown for the AAV-αSYN (c) and AAV-GFP (f) group. Abbreviations: DVR-1 = distribution volume ratio-1, CPu = caudate putamen, Cer = cerebellum, Co = control, *d*-AMPH = *d*-amphetamine, BP_{ND} = binding potential non displaceable, AAV = adeno-associated virus, αSYN = α-synuclein, GFP = green fluorescent protein, DVR-1 = distribution volume ratio minus one, T_{base} = 31-40 minutes, T_1 = 46-55 minutes, T_2 = 56-65 minutes, T_3 = 66-75minutes, + = p<0.05, * = p<0.01

4.2.2.3 Overexpression of pathology has no impact on resting-state functional connectivity

To assess the impact of pathology on resting-state functional connectivity of the dopaminergic and default-mode networks, we compared the ten-minute baseline interval before *d*-amphetamine stimulation among the Control, AAV-αSYN, and AAV-GFP cohorts (Figure 29). In the AAV-GFP group, a slight decrease in the connectivity strength could be detected in the dopaminergic network and the default-mode network indicated by yellow edges compared to the AAV-αSYN and Control group. Further, the change quantity shows an increasing trend in the AAV-GFP group, demonstrated by thinner edges.

However, no significant differences in the connectivity strength of the three groups were observed in the dopaminergic network and the default-mode network.

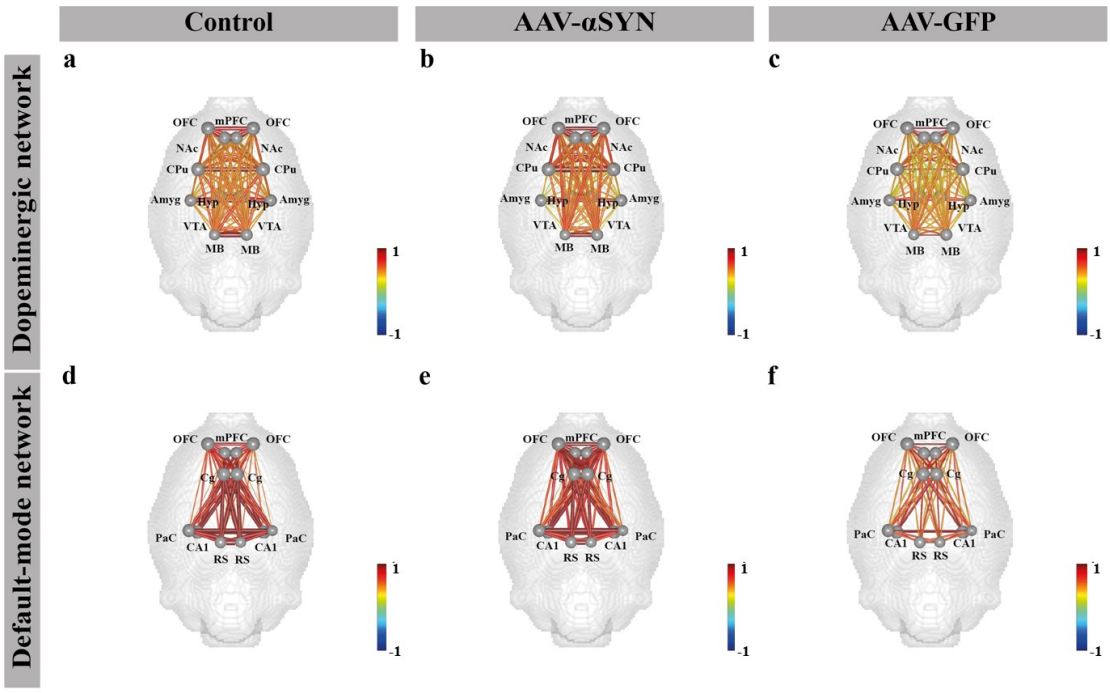

Figure 29: Effect of the pathology on resting-state functional connectivity in the dopaminergic network and the default-mode network.

The change in connectivity strength is shown as BrainMaps for all three groups in the dopaminergic network (a-c) and the default-mode network (d-f). The thickness of the nodes and the edges indicate the quantity of change. Abbreviations: AAV = adeno-associated virus, αSYN = α-synuclein, GFP = green fluorescent protein, Cg = cingulate cortex, mPFC = medial prefrontal cortex, OFC = orbitofrontal cortex, PaC = parietal cortex, RS = retrosplenial cortex, CA1 = hippocampus, NAc = nucleus accumbens, Amyg = amygdala, CPu = caudate putamen, Hyp = hypothalamus, MB = midbrain, VTA = ventral tegmental area

4.2.2.4 *D*-Amphetamine Stimulation Reduces Functional Connectivity in the Dopaminergic Network and the Default-mode Network in Healthy Rats

Group-level correlation matrices of the dopaminergic network showed a significant reduction in functional connectivity after *d*-amphetamine stimulation (Figure 30 d, e, f) compared to the animals stimulated with NaCl (Figure 30 a, b, c), with the most substantial effect in time interval T_3 (Figure 30 c). Significant decreases in functional connectivity occurred between the Amyg and the CPu (-63%, $p = 0.02$), the MB (-66%, $p = 0.01$), and the VTA (-50%, $p = 0.01$). Furthermore, a reduction in functional connectivity was observed between the mPFC and the Hyp (-95%, $p = 0.004$), the MB (-58%, $p < 0.02$), and the VTA (-67%, $p = 0.02$). However, none of the p-values survived multiple comparison correction.

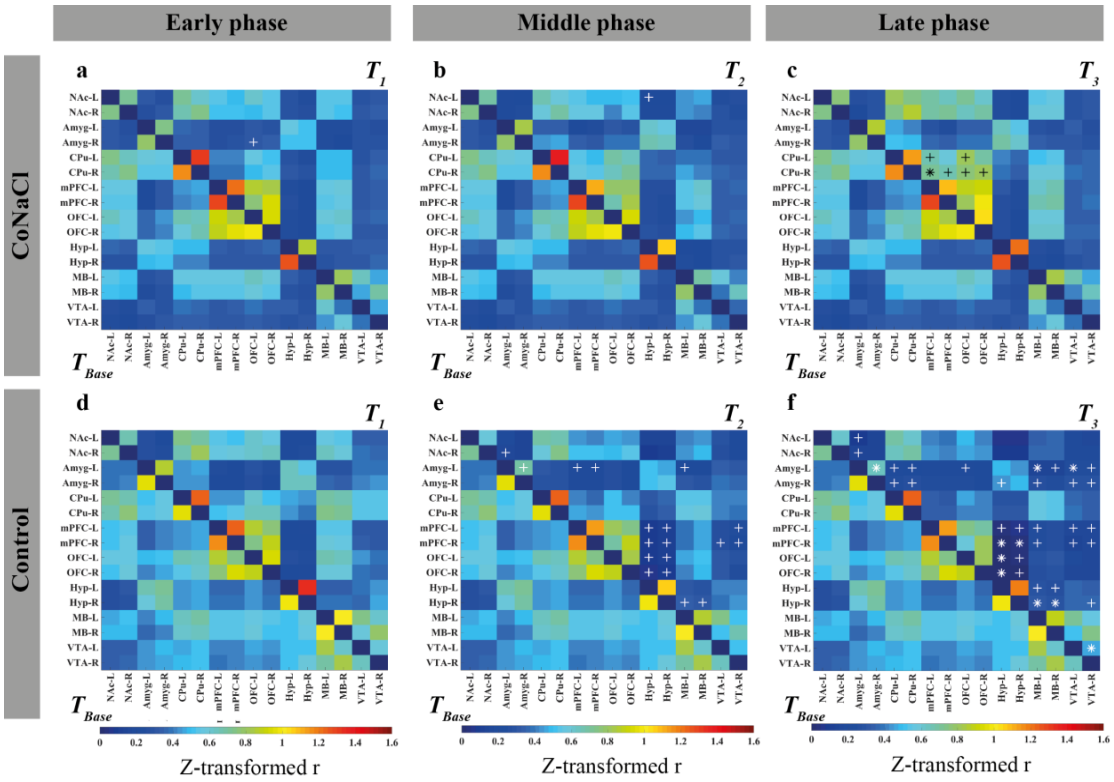

Figure 30: Effect of NaCl stimulation and *d*-amphetamine challenge on functional connectivity in the dopaminergic network in the CoNaCl and Control group during early, middle and late phase.

(a-c) Functional connectivity in the dopaminergic network is illustrated as mean-group correlation matrices for an early, middle, and late phase (upper diagonal matrices) after the NaCl stimulation and compared to baseline (lower diagonal matrices) for the CoNaCl group. (d-f) Functional connectivity in the dopaminergic network is illustrated as mean-group correlation matrices for an early, middle, and late phase (upper diagonal matrices) after the *d*-amphetamine challenge and compared to baseline (lower diagonal matrices) for the Control group. Abbreviations: T_{base} = 31-40 minutes, T_1 = 46-55 minutes, T_2 = 56-65 minutes and T_3 = 66-75 minutes, Cg = cingulate cortex, mPFC = medial prefrontal cortex, OFC = orbitofrontal cortex, PaC = parietal cortex, RS = retrosplenial cortex, CA1 = hippocampus, NAc = nucleus accumbens, Amyg = amygdala, CPu = caudate putamen, Hyp = hypothalamus, MB = midbrain and VTA = ventral tegmental area, L = left, R = right, + = $p<0.05$, * = $p<0.01$. None of the p-values survived multiple comparison correction

Significant reductions in functional connectivity after *d*-amphetamine stimulation in the default-mode network (Figure 31 d-f) were mainly seen between the mPFC and the PaC (-81%, p = 0.001) and between the Cg and the mPFC (-46%, p = 0.0008) which were also observable after multiple comparison correction in time interval T_2 and T_3. The time interval with the most substantial reduction in the functional connectivity was again T_3, in line with the temporal dynamics indicated by the [^{11}C]raclopride PET readout.

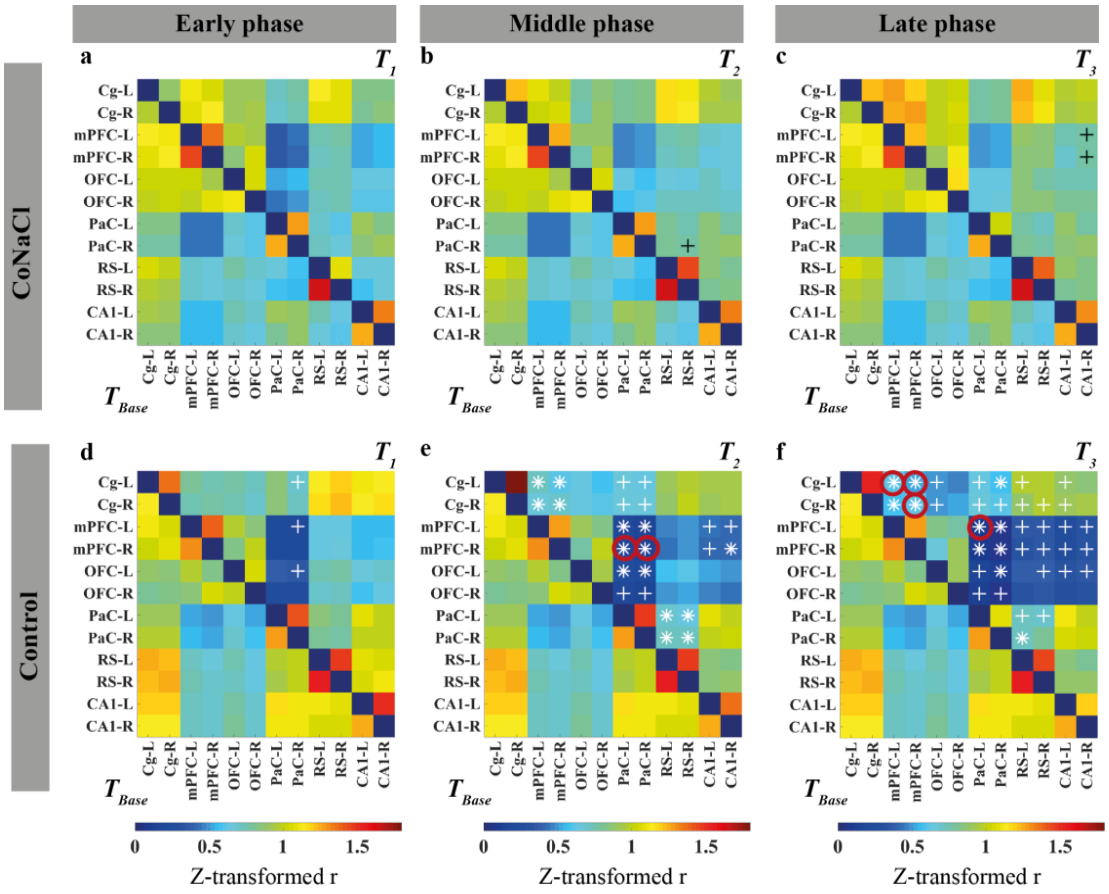

Figure 31: Effect of NaCl stimulation and *d*-amphetamine challenge on functional connectivity in the default-mode network in the CoNaCl and Control group during early, middle and late phase.

(a-c) Functional connectivity in the default-mode network is illustrated as mean-group correlation matrices for an early, middle, and late phase (upper diagonal matrices) after the NaCl stimulation and compared to baseline (lower diagonal matrices) for the CoNaCl group. (d-f) Functional connectivity in the default-mode network is illustrated as mean-group correlation matrices for an early, middle, and late phase (upper diagonal matrices) after the *d*-amphetamine challenge and compared to baseline (lower diagonal matrices) for the Control group. Abbreviations: T_{base} = 31-40 minutes, T_1 = 46-55 minutes, T_2 = 56-65 minutes and T_3 = 66-75 minutes, Cg = cingulate cortex, mPFC = medial prefrontal cortex, OFC = orbitofrontal cortex, PaC = parietal cortex, RS = retrosplenial cortex, CA1 = hippocampus, NAc = nucleus accumbens, Amyg = amygdala, CPu = caudate putamen, Hyp = hypothalamus, MB = midbrain and VTA = ventral tegmental area, L = left, R = right, + = $p<0.05$, * = $p<0.01$, red circle = corrected for multiple comparison

The sliding window approach was used to elucidate the dynamic changes in functional connectivity induced by the *d*-amphetamine stimulation on a higher temporal resolution. Therefore, the length and magnitude of alterations in the connectivity strengths of the dopaminergic network and default-mode network and changes in the nodal strengths of their corresponding regions were calculated (Figure 32). During the investigation of the changes in the dopaminergic network, it was observed that the connection strength of the Control group decreased consistently (Figure 32 c), while the CoNaCl group (Figure

32 a) showed no such decrease. The strongest effect was observed in the Hyp, where the decrease reached 61% compared to the baseline. On the network level, no significant reduction in connection strength was seen.

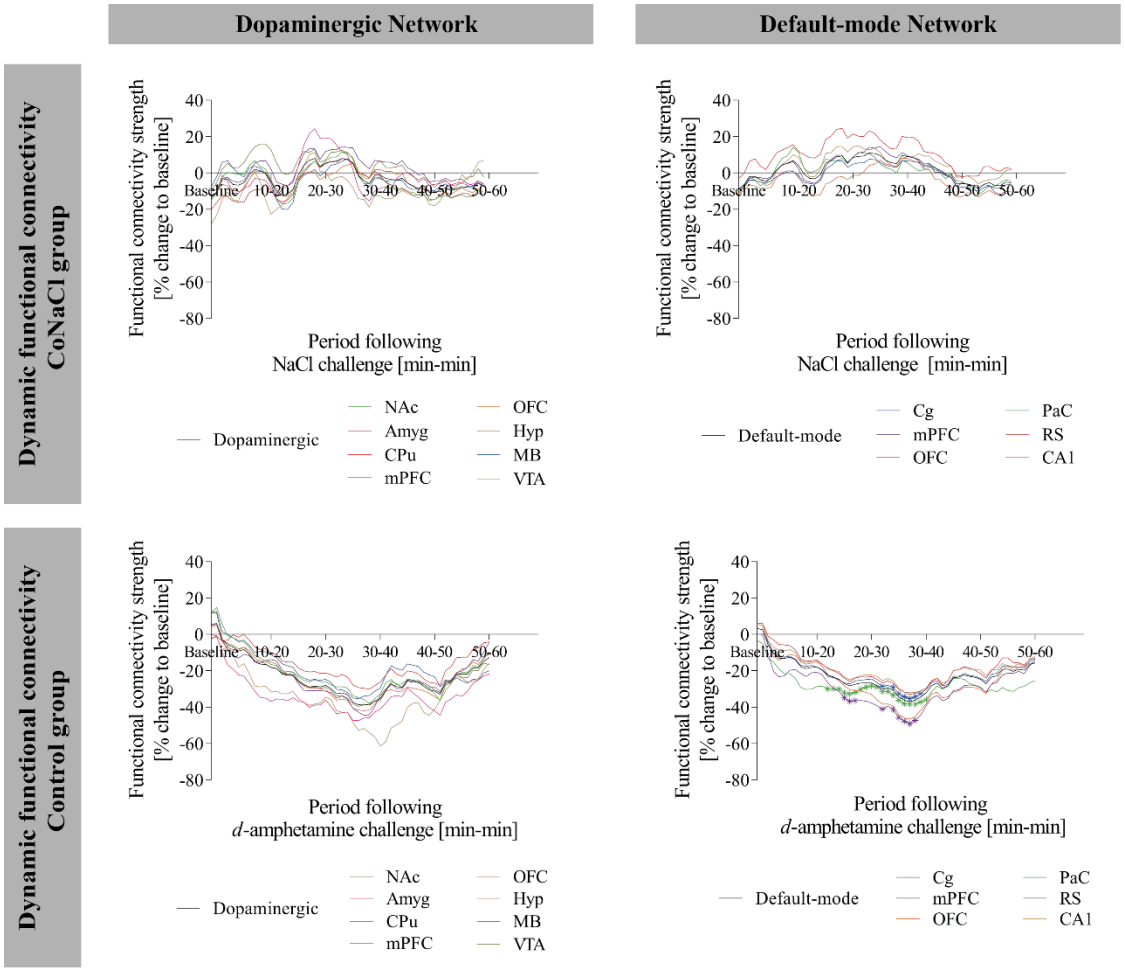

Figure 32: Effect of NaCl and *d*-amphetamine stimulation on dynamic functional connectivity in the dopaminergic network and the Default-mode in the CoNaCl and Control group.

(a, b) Changes in dynamic functional connectivity on regional and network levels were calculated minute-to-minute compared to baseline for regions of the dopaminergic and the Default-mode network in the CoNaCl group. (c, d). Changes in dynamic functional connectivity on regional and network levels were calculated minute-to-minute compared to baseline for regions of the dopaminergic and the Default-mode network in the Control group. Abbreviations: Cg = cingulate cortex, mPFC = medial prefrontal cortex, OFC = orbitofrontal cortex, PaC = parietal cortex, RS = retrosplenial cortex, CA1 = hippocampus, NAc = nucleus accumbens, Amyg = amygdala, CPu = caudate putamen, Hyp = hypothalamus, MB = midbrain and VTA = ventral tegmental area, * = $p<0.05$ corrected for multiple comparison

Compared to the CoNaCl group (Figure 32 b), the Control group stimulated with *d*-amphetamine (Figure 32 d) showed significant (corrected for multiple comparison) alterations in the node strengths of the Cg, mPFC and PaC comprising the default-mode network. The mPFC and the PaC revealed the earliest effect with significantly decreased

connection strengths for 5 and 19 consecutive time windows starting 13 minutes after the *d*-amphetamine stimulation, reaching a peak decrease of 49% and 38% to baseline, respectively. The Cg revealed significantly reduced connection strengths between 25 and 30 minutes, with a peak decrease of 35%. On the network level, a decrease in functional connectivity strength was observed 2 minutes after injection, with a peak drop of 40% compared to baseline.

4.2.2.5 Presynaptic Dysfunction Affects *d*-Amphetamine Induced Functional Connectivity Alterations

The group-average dopaminergic network functional connectivity matrices in the Control, AAV-αSYN, and AAV-GFP group during the early, middle, and late phases after *d*-amphetamine stimulation are illustrated in Figure 33. Paired t-tests were performed for all three time intervals, T_1, T_2, and T_3, and compared to T_{base} in all three groups. In the AAV-αSYN group, only the connections between the right Amyg with the right MB (-64%, $p = 0.04$) and right VTA (-43%, $p = 0.01$), as well as the Hyp and right MB (-76%, $p = 0.001$) decreased significantly in the late phase (Figure 33 g). The AAV-GFP group showed significant reductions in the connections in the late phase between the NAc and the CPu (- 25%, $p = 0.005$) and between the mPFC and the OFC (-21%, $p = 0.01$). A significant connection reduction between Amyg and the MB (-66%, $p = 0.02$) (Figure 33 k) was observed. The percent change in network strength of the dopaminergic network showed the strongest percent change in the Control group (35%) compared to the AAV-αSYN (15%) and the AAV-GFP (17%) group during the late phase (Figure 33 d, h, l). On node level, the strongest changes in the Control group occurred in the Amyg and the Hyp, with respective decreases of 47% and 43% (Figure 33 d). The smallest change was observed in the CPu (21%), which was even smaller in the AAV-αSYN (6%) (Figure 33 h) and AAV-GFP group (8%) (Figure 33 l). In the AAV-αSYN (Figure 33 h), the biggest percent change in connectivity strength was observed in the Hyp with 28%. The AAV-GFP group (Figure 33 l) revealed the biggest alteration in the NAc and Amyg, both with 25%.

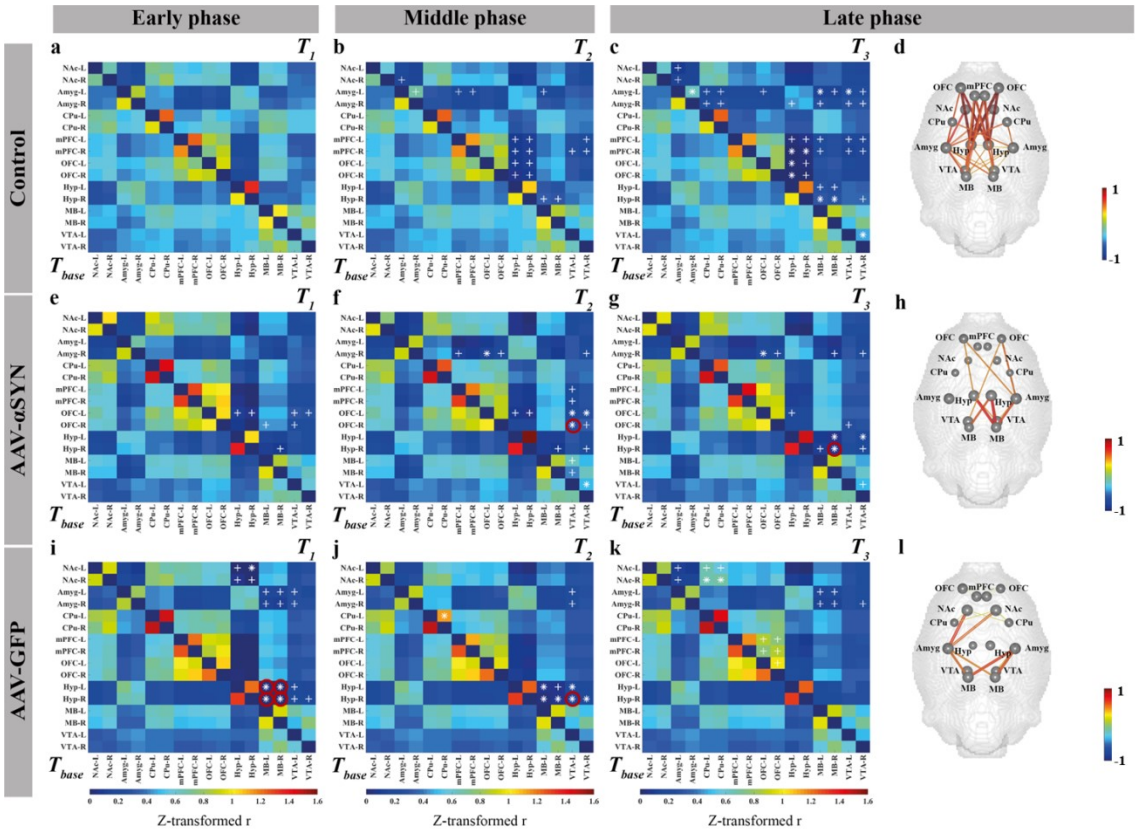

Figure 33: Comparison of the *d*-amphetamine stimulation effect on functional connectivity in the dopaminergic network between the Control, AAV-αSYN and AAV-GFP group during early, middle and late phase.

Functional connectivity in the dopaminergic network is illustrated as mean-group correlation matrices for the early, middle and late phase (upper diagonal matrices) after the *d*-amphetamine stimulation and compared to baseline (lower diagonal matrices) for the Control (a-c), AAV-αSYN (e-g) and AAV-GFP (i-k) group. The change in connectivity strength is shown as BrainMaps for all three groups during late phase (d, h, l). The thickness of the nodes and the edges indicates the quantity of change. Grey nodes refer to positive changes. Abbreviations: AAV = adeno-associated virus, αSYN = α-synuclein, GFP = green fluorescent protein, T_{base} = 31-40 minutes, T_1 = 46-55 minutes, T_2 = 56-65 minutes and T_3 = 66-75 minutes, NAc = nucleus accumbens, Amyg = amygdala, CPu = caudate putamen, mPFC = medial prefrontal cortex, OFC = orbitofrontal cortex, Hyp = hypothalamus, MB = midbrain, VTA = ventral tegmental area, L = left, R = right, + = p<0.05, * = p<0.01, red circle = corrected for multiple comparison

No significant asymmetry in the functional connectivity of right and left hemispheres of the dopaminergic network was detected for the AAV-αSYN group in any of the three time intervals (Figure 34). In the middle phase, a significant difference in the network strength was observed for the left hemisphere between T_{base} and T_2 (19%, p = 0.02). The left OFC (29%, p = 0.004), MB (14%, p = 0.04), and VTA (26%, p = 0.02) change significantly, and also the right Amyg (25%, p = 0.03) and VTA (21%, p = 0.01). The late phase revealed a significant difference in the network strength for the right hemisphere (20% p = 0.02), including significant changes in the right Amyg (37%, p = 0.01) and right

Hyp (41%, p = 0.01). However, the p-values did not survive multiple comparison correction.

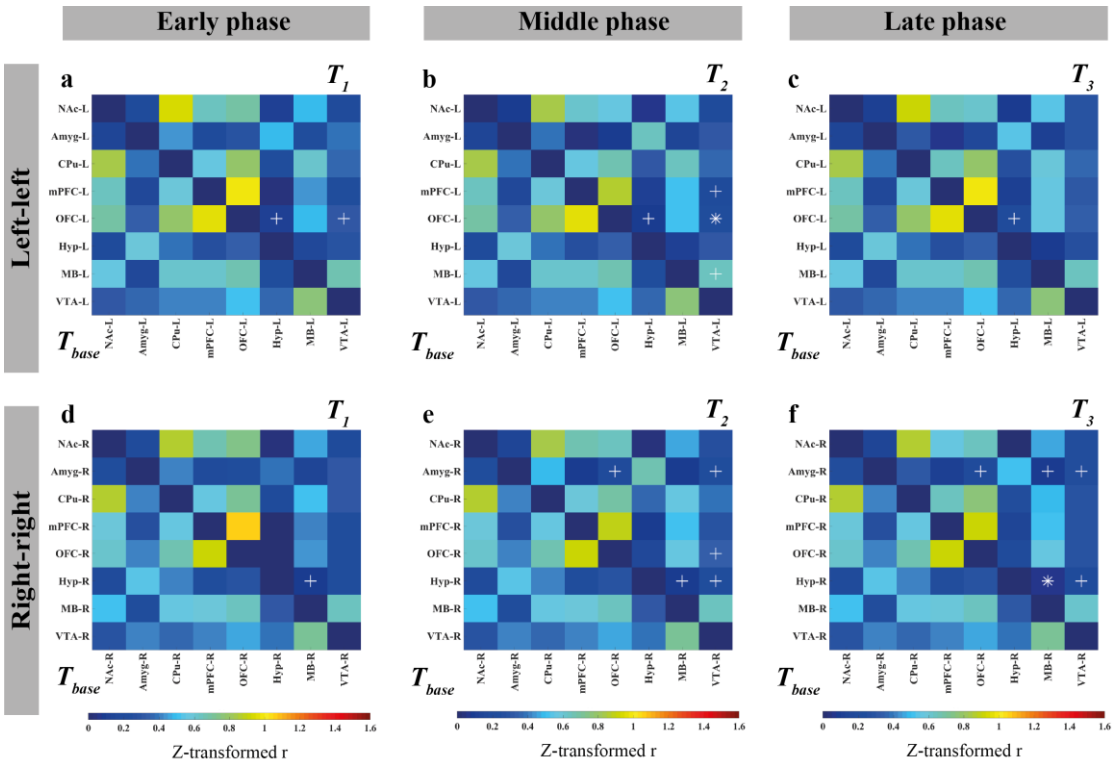

Figure 34: Comparison of the functional connectivity and network and node strength in the dopaminergic network between left and right hemisphere of the AVV-αSYN group during early, middle and late phase after *d*-amphetamine stimulation.

Functional connectivity in the dopaminergic network is illustrated as mean-group correlation matrices for the early, middle and late phase (upper diagonal matrices) after the *d*-amphetamine stimulation and compared to baseline (lower diagonal matrices) between the left non-injected hemisphere (a-c) and the right AAV-αSYN-injected hemisphere (d-e). Abbreviations: AAV = adeno-associated virus, αSYN = α-synuclein, T_{base} = 31-40 minutes, T_1 = 46-55 minutes, T_2 = 56-65 minutes and T_3 = 66-75 minutes, NAc = nucleus accumbens, Amyg = amygdala, CPu = caudate putamen, mPFC = medial prefrontal cortex, OFC = orbitofrontal cortex, Hyp = hypothalamus, MB = midbrain, VTA = ventral tegmental area, FC = functional connectivity, L = left, R = right, + = p<0.05, * = p<0.01

In the default-mode network (Figure 35), paired t-tests indicated reduced functional connectivity in T_1, T_2, and T_3 after the stimulation for all three groups. The decreases in functional connectivity observed in both AAV-αSYN (Figure 35 e-g) and AAV-GFP groups (Figure 35 i-k) were less distinct and significant compared to the Control group (Figure 35 a-c). In T_3, significantly reduced functional connectivity was detected between the OFC and the PaC (-36%, p = 0.004) and CA1 (-30%, p = 0.03) for the AAV-αSYN group (Figure 35 g). The AAV-GFP group showed significantly reduced functional connectivity between the Cg and the CA1 (-31%, p = 0.006) and additionally between the

mPFC and the OFC (-21%, p = 0.01) (Figure 35 k). The percent change of the overall network connectivity strength in the default-mode network was reduced to a higher extent in the Control group (32%) (Figure 35 d) compared to the AAV-αSYN (12%) (Figure 35 h) and AAV-GFP (15%) group (Figure 35 l).

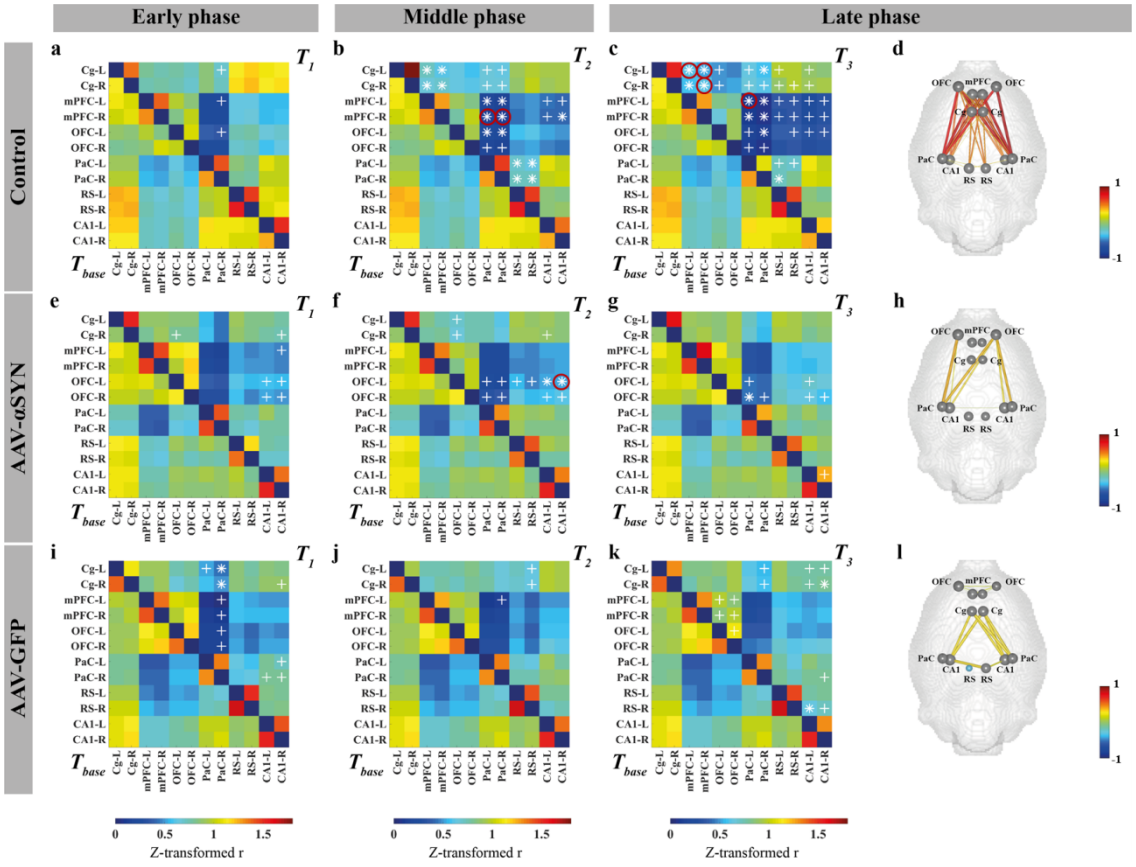

Figure 35: Comparison of the *d*-amphetamine stimulation effect on functional connectivity in the default-mode network between the Control, AAV-αSYN and AAV-GFP group during early, middle and late phase.

Functional connectivity is illustrated as mean-group correlation matrices for the early, middle and late phase (upper diagonal matric) after the *d*-amphetamine stimulation and compared to baseline (lower diagonal matric) in the default-mode network for Control (a-c), AAV-αSYN (d-f) and AAV-GFP (g-h) group. The change in connectivity strength is shown as BrainMaps for all three groups during late phase (d, h, l). The thickness of the nodes and the edges indicate the quantity of change. Abbreviations: AAV = adeno-associated virus, αSYN = α-synuclein, GFP = green fluorescent protein, T_{base} = 31-40 minutes, T_1 = 46-55 minutes, T_2 = 56-65 minutes and T_3 = 66-75 minutes, Cg = cingulate cortex, mPFC = medial prefrontal cortex, OFC = orbitofrontal cortex, PaC = parietal cortex, RS = retrosplenial cortex, CA1 = hippocampus, L = left, R = right, + = p<0.05, * = p<0.01, red circle = corrected for multiple comparison

In the Control group, the mPFC and the OFC revealed the strongest changes in connectivity strength in T_3, with respective decreases of 40% and 41% (Figure 35 d). Compared to the AAV-αSYN (Figure 35 h) and the AAV-GFP group (Figure 35 l), the mPFC

showed a less prominent decrease of around 9% and 13%, respectively. However, the p-values did not survive multiple comparison correction.

Furthermore, the left-right difference of the AAV-αSYN observed in the [^{11}C]raclopride PET BP_{NDS} did not translate into asymmetric functional connectivity between the right and left hemispheres in the default-mode network (Figure 36). No significant differences were revealed in the network strength in all three time phases. On node level, the left hemisphere revealed significant differences in the Cg (21%, p = 0.04) and the OFC (36%, p = 0.01) during the middle phase (Figure 36 b, e). However, the p-values did not survive multiple comparison correction.

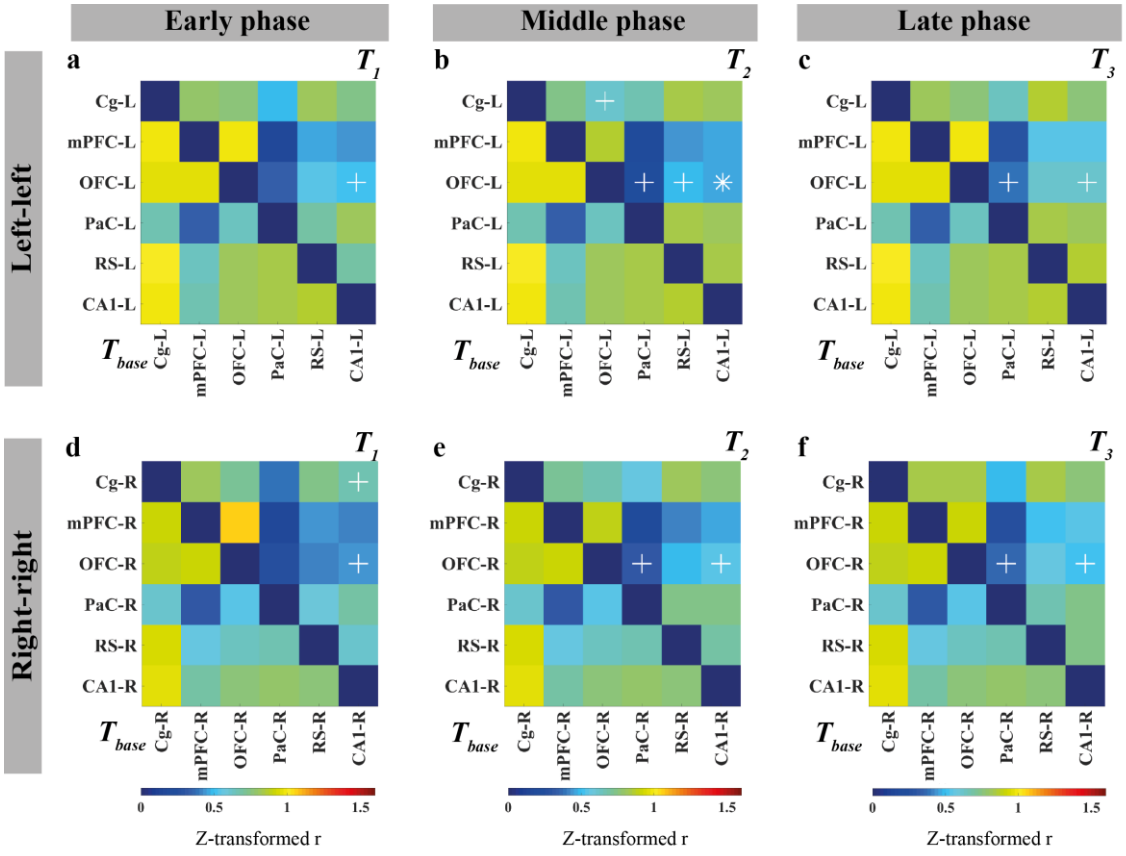

Figure 36: Comparison of the functional connectivity and network and node strength in the Default-mode network between left and right hemisphere of the AVV-αSYN group during early, middle and late phase after *d*-amphetamine stimulation.

Functional connectivity is illustrated as mean-group correlation matrices for the early, middle and late phase (upper diagonal matrices) after the *d*-amphetamine stimulation and compared to baseline (lower diagonal matrices) in the default-mode network between the left non-injected hemisphere (a-c) and the right AAV-αSYN-injected hemisphere (d-e). Abbreviations: AAV = adeno-associated virus, T_{base} = 31-40 minutes, T_1 = 46-55 minutes, T_2 = 56-65 minutes and T_3 = 66-75 minutes, Cg = cingulate cortex, mPFC = medial prefrontal cortex, OFC = orbitofrontal cortex, PaC = parietal cortex, RS = retrosplenial cortex, CA1 = hippocampus, FC = functional connectivity, L = left, R = right, + = p<0.05, * = p<0.01.

5 Discussion

5.1 Part I: *In vitro* evaluation of the binding affinity and selectivity of anle138b derivatives to α-synuclein aggregates

The molecular pathogenesis of all common neurodegenerative diseases is associated with the disease-specific aggregation of misfolded proteins. Aggregation of αSYN has been shown to play a crucial role in the pathogenesis of PD (19), LBD, and MSA (107, 108). Since its discovery in 1997, much research on αSYN has been conducted, revealing that the aggregation of αSYN seems to be the central driver of the pathogenesis of synucleinopathies; however, the relationship between αSYN misfolding and cellular dysfunction or cell death is far from being fully understood. Noninvasive imaging technologies such as MRI and PET could serve as valuable tools for the early and differential diagnosis of neurodegenerative diseases. Furthermore, they would allow for monitoring of disease progression and therapy control. Although PET imaging of Aβ in AD is well established (109-111), PET tracers to detect pathologically aggregated αSYN in synucleinopathies are still missing despite intensive research (112). An αSYN PET tracer would unquestionably be highly important and a game-changing tool for diagnosis and therapy development.

This work aimed to develop a PET tracer starting from the lead structure anle138b, a compound that has been shown to have therapeutic activity in animal models of PD (53, 54) and MSA (50) based on specific structure-dependent binding to aggregated αSYN (113). However, anle138b has a very high logP value (logP > 5.54); therefore, it does not meet the criteria of a potential CNS PET tracer. Anle253b, a derivative of anle138b, was the first compound that underwent carbon-11 labeling and showed high affinity towards αSYN aggregates *in vitro*; however, it showed suboptimal pharmacokinetics *in vivo* (114). Therefore, the chemical structure of anle253b was modified by our collaborators (MODAG GmbH) to improve the pharmacokinetic properties. It led to the development of four new compounds: MODAG-001, anle2F4CP, sery383, and sery512a.

These compounds were tested in saturation binding experiments towards their affinity to human recombinant αSYN fibrils. [^{3}H]MODAG-001 showed high affinity to recombinant αSYN fibrils in saturation binding assays *in vitro*, with a K_d value of 5.5 ± 2.1 nM followed by [^{3}H]anle24FCP with a K_d value of 8.9 ± 2.1 nM. The specific binding curve

of [^{3}H]MODAG-001 indicates a clear binding of the compound to the αSYN fibrils reaching saturation towards a higher concentration of [^{3}H]MODAG-001. However, low B_{max} values obtained for all the compounds suggest that the number of binding sites is low. After the αSYN fibrils were incubated on the plates overnight, several washing steps were performed, potentially resulting in the removal of αSYN. The performance of an assay that includes multiple washing steps can be variable, as it is impossible to know how many binding sites will remain at the end of the experiment. To improve the assay, future experiments could use a Filtermat system, which separates unbound compounds from bound compounds after transferring αSYN fibrils to a filter. Another approach to increase the availability of binding sites could be the sonication of the αSYN fibrils, which has already been tested in subsequent experiments in our laboratory, showing an increase in the amount of available binding sites (89).

Various compounds were developed and investigated in the last decades as potential αSYN PET ligands (53, 55, 89, 114-141). The research group of Fodero-Tavoletti and colleagues studied [^{18}F]BF227 and showed a 3-fold higher binding affinity for αSYN fibrils *in vitro* (K_d = 9.6 nM) compared to [^{3}H]MODAG-001 and a very high affinity to Aβ fibrils (K_d = 1.3 nM). Therefore, it failed to display a binding in Aβ-free human brain homogenates with LBs (120). In these experiments, a filter binding assay was used to separate bound from free radioactivity by filtration. *In vivo*, [^{11}C]BF227 revealed a higher signal in MSA patients in GCI-rich brain regions compared to age-matched controls. However, the individual values varied and overlapped with patients and healthy controls (126). Further, Verdurand *et al.* examined the previously published [^{18}F]BF227 in medulla sections obtained from MSA patients and revealed no binding to cytoplasmic glial inclusions (132). Kaide *et al.* identified a bisquinoline scaffold as a promising structure for targeting αSYN aggregates and designed two derivatives, BQ1 and BQ2 (125). Both derivatives showed sufficient affinity for αSYN aggregates, with a K_i of 17.0 ± 3.5 nM for BQ1 and a K_i of 11.6 ± 2.6 nM for BQ2 after the performance of inhibition assays. Further, αSYN aggregates were detected with both derivatives in a medulla oblongata section from a PD patient and confirmed by immunohistological staining of the same section with antibodies against αSYN. However, the pharmacokinetics of [^{18}F]BQ2 in healthy mice were unsatisfactory (125). Akasaka *et al.* synthesized and investigated radioionated phenylbenzofuranone derivatives, which showed high binding affinity to recombinant αSYN aggregates in an inhibition assay, but achieved insufficient brain uptake (140). New chalcone analogs for the detection of αSYN were evaluated by Kaide *et al.*

(141). PHNP-3 showed promising *in vitro* characteristics but moderate brain penetration (141). More recently, a study by Xiang et al. tested F0502B, a benzothiazole-ethenylphenol derivative, on human brain homogenates (136). The K_d for aggregated αSYN in PD was 3.68 nM and 6.23 nM for aggregated αSYN in LBD. In comparison, the K_d for Aβ fibrils was 151.20 nM, and the K_d for tau fibrils was 151.20 nM in AD, suggesting a selective binding of F0502B to αSYN (136).

Further, the binding of [^{3}H]anle138b, [^{3}H]MODAG-001, [^{3}H]anle2F4CP, [^{3}H]sery383, and [^{3}H]sery512a to Aβ aggregates was tested in autoradiography experiments using mouse and human brain sections and compared to [^{3}H]PIB, the gold standard for imaging Aβ pathology in the brain. The results revealed an up to 15-fold higher binding of [^{3}H]PIB to Aβ plaques. The specific binding corresponding to the distribution of Aβ plaques was observed in the mouse brain tissue sections for all compounds. All compounds except [^{3}H]sery512a revealed binding to Aβ aggregates at a much lower degree than [^{3}H]PIB. It shows that the tested compounds are not fully selective towards αSYN fibrillar structures.

Since [^{3}H]MODAG-001 showed the highest binding affinity and acceptable selectivity over Aβ, the binding specificity was tested in autoradiography experiments on human brain sections of different proteinopathies (PD, PSP, AD, MSA, and control cases). Clear binding of [^{3}H]MODAG-001 was observed in PD and AD brain sections. However, a quantitative analysis did not show significant differences between the PD and the Ctrl case or between the AD and Ctrl case. The PSP case revealed a significant difference ($p < 0.05$) compared to the Ctrl case. Since both PD and AD tissues show co-pathology with αSYN, Aβ, and Tau aggregates, it is challenging to state which aggregate [^{3}H]MODAG 001 is binding to. The MSA Ctrl case displayed a significantly higher binding of [^{3}H]MODAG-001 than the MSA case. The low binding in the MSA case results from the low amount of pathology in the tissue. More intense binding was observed in the cortical grey matter compared to the white matter, which the unlabeled compound could block. Nevertheless, this difference was also observed in controls and is related to blocking non-specific binding. Future studies should include screening against Aβ and tau aggregates since most neurodegenerative diseases show mixed pathology using immunofluorescence as cross-validation. For achieving an accurate colocalization of tracer binding with histopathology at a high resolution, the technique of microautoradiography should be employed.

Another essential aspect in performing autoradiography experiments is the incubation buffer. To block the nonspecific binding sites, 0.1% BSA was added in the autoradiography experiments. However, as it may also block the few αSYN binding sites on human PD tissue, this concentration may have been too high. Ethanol and tween could be added to the washing buffer to reduce non-specific binding in the autoradiography experiments further. However, as the actual binding of the compound to the target protein can also be washed away, only low concentrations are tolerable. Verdurand *et al.* examined the previously published [^{18}F]BF227 and compared it to their newly developed compounds [^{18}F]2FBox and [^{18}F]4FBox using *in vitro* autoradiography in transgenic mouse models of AD and PD, fibril inoculated rats, as well as human PD and MSA sections (133). The authors could successfully detect injected αSYN fibrils in rats; however, they failed to detect αSYN or Aβ in mouse models, as well as αSYN aggregates in LBs or GCI in human cases (133). Compared to our study, they used only PBS as an incubation buffer and three different ethanol concentrations for their washing steps. More recently, the derivative of PBB3, C05-01, revealed a K_d of 24 nM in a saturation assay with human αSYN fibrils, which is compared to [^{3}H]MODAG-001 2-fold higher (130). C05-01 was tested in fluorescence and autoradiography experiments in fresh frozen human tissue sections. Three different brain regions (amygdala, cingulate cortex, and substantia nigra) with αSYN pathology were evaluated in one PD case, one AD case, and one control case. Furthermore, they tested C05-01 in tissue microarrays containing brain homogenates of MSA, PD, AD, Pick's disease, vascular dementia, and control tissue. The experiments revealed a binding to αSYN in PD and MSA tissue. However, binding was also observed in tissue from AD and Pick's disease, pointing towards an Aβ and tau binding (130). Endo *et al.* published another PPB3 derivative, C05-05 (118). After testing the binding of C05-05 *in vitro* to αSYN pathologies, the compound was labeled with fluorine-18 and tested in αSYN mice and marmosets as well as on human tissue with αSYN pathologies revealing binding to αSYN. The application of [^{18}F]C05-05 in patients with LBD showed enhanced retention of [^{18}F]C05-05 in the midbrain of LBD cases compared to controls. MSA patients displayed higher retentions of [^{18}F]C05-05 in the putamen. Another promising compound ACI-12589 was published from Smith *et al*. (142) this year. They performed AR experiments on PD and MSA cases revealing a K_d of 17 nM and 28 nM, respectively. Further, they showed an extensive overlap of immunohistochemistry staining and high-resolution autoradiography on the same tissue section. After confirming selectivity of the compound as well as a clean off-target profile, the authors evaluated the *in vivo* performance in

different patient groups. [^{18}F]ACI-12589 revealed clear binding in brain areas with high αSYN pathology of MSA cases (142). These paper shows the importance of cross-validation with immunofluorescence in the same human brain section used for autoradiography to ensure accurate colocalization of aggregated protein with radioligand binding. Since αSYN aggregates are very small (1-10 µm) it will be impossible to make a colocalization on a consecutive section. In future studies, cross-validation of radioligand binding to immunohistochemical stainings must be performed to confirm the possible binding of the PET tracer to αSYN pathology in microautoradiography experiments.

Another point is the structural differences between the αSYN fibrils used in the screening assays and those in human brain tissue. Literature demonstrated structural differences between recombinant fibrils obtained *in vitro* and fibrils in patients, which may also account for the different binding behaviors of [^{3}H]MODAG-001. The study by Strohaker *et al.* identified structural differences in αSYN fibrils from LBD patients by amplifying aggregates from patient samples by protein misfolding cyclic amplification (143). They also revealed the heterogeneity of αSYN fibrils in different synucleinopathies using solution-state NMR spectroscopy and fluorescent probes. Other studies compared artificially produced Tau fibrils with Tau extracted from AD or Pick's disease patients carrying Tau pathology and observed structural differences in cryo-electron microscopy experiments (144-147). Despite these structural differences between recombinant fibrils and those found in human brain slices, recombinant fibrils remain a widely used screening tool for the preselection of compounds before PET radiolabeling because the availability of brain homogenates or αSYN brain extracts is limited.

Next, the pharmacokinetic properties and metabolism of [^{11}C]MODAG-001 were investigated in healthy mice. The pharmacokinetic profile of [^{11}C]MODAG-001 revealed a good blood-brain barrier penetration, showing a high uptake into the brain (SUV = 1.3) and a fast clearance from the brain. The metabolite analysis of [^{11}C]MODAG revealed one metabolite in the brain, the demethylated precursor MODAG-005.

PET imaging was further performed in the A30P transgenic mouse model of Parkinson's disease with intracellular αSYN pathology in the midbrain and brainstem and compared to young and healthy age-matched control mice (35, 36). However, no difference could be observed between regions with expected pathology, such as the brainstem, thalamus, and hippocampus, and areas without pathology, such as the cortex. Also, no difference between old A30P mice and age-matched controls was seen due to the high non-specific

binding of [^{11}C]MODAG-001, leading to a high background signal causing small differences in specific binding to be undetected. According to the literature, the A30P transgenic mice show pathology at 12 months, which increases with time (35, 36). Therefore, the PET experiments were performed at around 75 weeks. However, immunohistological staining of A30P transgenic mouse brains performed at our institute has shown that pathology can vary significantly between animals, which may also explain why no specific binding could be detected in the animals. Therefore, in future studies, the time of the imaging experiment should be determined based on of the phenotype (appearance of the imbalance), as this correlates strongly with the pathology in the brainstem and midbrain. However, as mice can die within a few days of the onset of the phenotype, this requires daily monitoring of the animals.

After titration of demethylated precursor MODAG-005, autoradiography binding experiments were performed on human brain sections of different proteinopathies to determine the binding specificity and selectivity. Clear binding of [^{3}H]MODAG-005 was observed in PD and AD brain sections, which need to be cross-validated using immunofluorescence and colocalized with the tracer binding in microautoradiography experiments. Quantitative analysis shows no significant differences between PD and Ctrl and AD and Ctrl. Again, the PSP case revealed a significant difference ($p < 0.001$) compared to the Ctrl case. Since both PD and AD tissues show co-pathology with αSYN, Aβ, and Tau aggregates, it is challenging to state which aggregate [^{3}H]MODAG-005 is binding to. The MSA Ctrl case displayed a significantly higher binding of [^{3}H]MODAG-005 than the MSA case, indicating low pathology in the MAS case. In all cases, grey matter showed more intense binding than white matter, which the nonlabeled compound could block.

Determining the αSYN fibril binding sites of novel compounds is another essential evaluation point that needs to be considered for PET tracer development. Using a combination of *in silico* docking, photoaffinity labeling, and radiotracer binding studies, Hsieh and Ferrie *et al.* published three putative binding sites for fibrillar αSYN (122). They identified that styrene and piperazine-based analogs preferred binding sites 2 and 9, whereas tricyclic compounds and an indolinone diene analog preferred binding site 3/13. Another aspect regarding the development of radiotracers is considering the structure of αSYN fibrils. Tracer binding sites for fibrils are usually located on the outside. However, αSYN fibrils and other amyloid fibrils have long tubular hollows, which could also be proposed as internal binding sites. The location of anle138b in αSYN fibrils was investigated using nuclear magnetic resonance spectroscopy, which revealed interactions between anle138b

and the inside of the tubular cavity of the fibrils (48). Since [^{3}H]MODAG-001 and [^{3}H]MODAG-005 are chemical derivatives of anle138b, we hypothesize that these compounds behave similarly, binding on the tubular cavity of fibrils.

During the last years, various compounds have been published as potential αSYN-specific PET tracers (53, 55, 89, 114-141). However, developing an appropriate PET tracer remains challenging due to the low abundance of αSYN inclusions and the structural similarity of αSYN to Aβ and tau proteins, which are simultaneously present in pathological brain regions (148, 149). To achieve higher signal-to-noise ratio in human tissue with αSYN pathology, the nonspecific binding of MODAG-001 must be reduced. This could be achieved by a change in the chemical structure (removal of a methyl group), which increases the hydrophilicity of the molecule and decreases the non-specific binding in white matter brain structures (150). The demethylated form of MODAG-001, MODAG-005, needs further cross-validation to immunofluorescence and microautoradiography to colocalize and quantify the αSYN pathology and the radioligand binding. Determining the αSYN fibril binding site using cryo-electron microscopy is another step that could be considered in future experiments.

5.2 Part II: A multimodal imaging approach to link protein aggregation to molecular and functional neuronal changes in an animal model of α-synuclein overexpression

5.2.1 Evaluation of the Variability and Reliability of a Simultaneous [^{11}C]Raclopride-PET/BOLD-fMRI Approach

Combining phMRI with PET offers excellent potential to investigate brain network modulations from different neurotransmitter systems and provides information about biological and molecular neurotransmitter-receptor interactions *in vivo*. To ensure that the changes detected are due to the applied pharmacological stimulation, it is necessary to investigate the test-retest variability and reliability of the measurements. The picomolar sensitivity of PET (151) enables imaging of the distribution of various molecular targets and related biological processes in the brain. The combination of both imaging modalities may provide a deeper insight into the coupling of molecular and functional neural mechanisms underlying specific processes in the healthy and in the diseased brain (152, 153).

5.2.1.1 Within and between [^{11}C]Raclopride-PET Variability and Reliability

To compare molecular changes after a pharmacological stimulation to baseline within the same animal and scan, a bolus plus constant infusion protocol of [^{11}C]raclopride was established. After 40 minutes of baseline measurement, a NaCl stimulation was performed, and measurements were taken for an additional 60 minutes. This NaCl stimulation was used to exclude any perfusion effects from the injection of the solution.

Next, the [^{11}C]raclopride binding variability in the CPu within and between scans was investigated. The CPu variability of [^{11}C]raclopride within scans was calculated, revealing a variability of around 4% in early time intervals, increasing to 11% in later time intervals post NaCl stimulation. This means that changes below 11% cannot be reliably detected with this [^{11}C]raclopride bolus infusion protocol. In our study, the DVR-1 was decreasing over time. This could be related to the infusion of high amounts of [^{11}C]raclopride, resulting in the infusion of high quantities of unlabeled raclopride. This could also have the effect of occupying the D_2 receptors, with the result of less [^{11}C]raclopride binding and a decrease in DVR-1. In addition, by the end of the 100-minute scan,

[^{11}C]raclopride had decayed by five half-lives, which means that the time-activity curves are noisier because of the lower activity.

In longitudinal PET studies, for example, animals must be measured multiple times to follow up disease progression in animal models. Therefore, test-retest variability needs to be low to detect disease-specific differences. In our study, the CPu variability between scans for [^{11}C]raclopride was 13%, reaching 20% in later time intervals post NaCl stimulation between test and retest scans. This difference is relatively high compared to previous studies in mice in our lab (154), and consistently lower in the second scan. This relates to the consistently lower molar activity of [^{11}C]raclopride in the second scan (Table 5) resulting in a lower tracer binding due to increased occupancy of unlabeled raclopride at the D_2 receptor. Therefore, keeping the molar activity constant in all measurements is crucial to compare different animals. Fischer *et al.* quantified the CPu variability in eight mice using a [^{11}C]raclopride bolus protocol on Inveon Siemens dedicated small animal PET scanners, revealing a test-retest variability of around 8% (154) being lower than the CPu variability in the early time intervals after NaCl stimulation in this work. Another study from Alexoff *et al.* used the MicroPET R4 tomograph (Concorde Microsystems) for performing test-retest scans in the rat brain and calculated a coefficient of variation for the CPu of 18% (155). Further, biological factors such as physiological differences in the animals (breathing, heart rate, temperature) and also the differences in D_2 receptor density and affinity (156) may cause discrepancies in the variability of [^{11}C]raclopride-PET scans.

Human test-retest studies are primarily carried out with a bolus protocol of [^{11}C]raclopride. Volkow *et al*. published 1993 a study that analyzed the reproducibility of repetitive 60-minute scans of [^{11}C]raclopride binding. The authors revealed an intra-subject variability of 4%–9% and an intersubject variability of 13%–43% in humans (157). These numbers agree with our results for within and between variability. Hietala *et al.* studied short and long-term stability of measurements for D_2 dopamine receptor density, affinity, and binding potential with [^{11}C]raclopride in eight healthy humans using a whole-body PET scanner (ECAT 931108-12, CTI, Nashville, TN, USA). Therefore, four subjects were scanned for 49 minutes during two test-retest intervals: 3 to 7 weeks (short-term) and 6 to 11 months (long-term). The results of the short-term measurements revealed an absolute variability of 12.5 ± 5.5%, 7.3 ± 3.8%, and 5.5± 3.4% for B_{max}, K_d, and the binding potential, respectively. The variability of the long-term measurements was higher, with 16.5 ±11.3%, 9.6 ± 6.6%, and 10.4± 2.8% for B_{max}, K_d, and the binding potential,

respectively (158). This reveals a higher variability if the test-retest interval is longer. In our study, the test-retest interval was also long, with 4 months, which could further influence the variability between scans. A study from the Turku group published in 2015 examined the long-term reliability of striatal and extrastriatal dopamine D_2 receptors with [^{11}C]raclopride using the ECAT high-resolution PET scanner (HRRT; Siemens Medical Solutions, Knoxville, TN, USA) in seven healthy subjects with a 5-week test-retest interval. The authors used a bolus plus constant infusion [^{11}C]raclopride protocol. However, only the acquired data from the first 55 minutes were analyzed for the test-retest absolute variability. To quantify the binding potential, the SRTM was used. Low absolute variability was indicated for the caudate nucleus (4.5%), putamen (3.9%), and ventral striatum (3.9%) as well as for the thalamus (3.7%). Cortical regions revealed higher variability from 6.1% to 13.1% (159). Karalija *et al.* tested seven-month test-retest reliability for extrastriatal [^{11}C]raclopride binding in 27 older adults revealing low absolute variability across all analyzed structures (160). Both human studies show lower variability values for the CPu compared to our study. The PET reliability in our study was zero because of the different molar activities between the test (106.5 ± 35.2 GBq/µmol) and retest (86.5 ± 25.5 GBq/µmol) measurements, leading to lower binding values in the retest scans.

5.2.1.2 Within and between Reliability of BOLD-fMRI Scans

Cognitive research application and drug development using BOLD-fMRI require generating stable and reliable signal changes in preclinical and clinical settings. Since there is increasing interest in the potential application of fMRI as an imaging biomarker to study therapeutic interventions and individualized therapy, maximizing confidence in the chosen intervention and experimental design is necessary. Test-retest reliability of BOLD-fMRI scans is essential in selecting reliable measures. Statistical reliability describes the temporal or within-subject stability, and test-retest reliability represents the between-scan stability of an index across a group.

This work investigated the within and between reliability of 100-minute BOLD-fMRI scans, including a NaCl stimulation after 40 minutes in healthy rats. BOLD-fMRI reliability was analyzed using Pearson's correlation coefficient r. Pearson's r for 52 brain regions was calculated for 15-minute intervals after the NaCl stimulation and compared to 15-minute baseline measures before the NaCl stimulation. The results revealed a moderate correlation (r = 0.5-0.6) between scans and a good correlation within scans (r = 0.7-

0.8). To my knowledge, no test-retest study was performed in animals using BOLD-fMRI. However, the test-retest reliability of resting-state functional connectivity was investigated in humans, reporting ICC values of 0.5 (161) to 0.6 (162), pointing to a modest test-retest reliability. The moderate test-retest reliability comes mainly from the noise in the data after preprocessing. Further, scanner artifacts, subject motions, and physiological parameters such as breathing and heartbeat can influence the reliability between scans.

Grandjean *et al.* published a consensus rat functional magnetic resonance imaging acquisition protocol (StandardRat) (163). They identified experimental parameters associated with a robust and reliable detection of high levels of functional connectivity, such as breathing rate and cortical temporal signal-to-noise ratio. Further, their protocol relies on mild sedation of the animals (163). In our study, the animals breathed freely under anesthesia (80-135 breaths per minute), which is in the suggested range from Grandjean *et al.* of 84 to 114 breaths per minute. Further, we used mild anesthesia with 1.3% isoflurane. However, isoflurane is known to affect functional connectivity (for further discussion, see 5.2.2.2).

Since fMRI-based functional connectivity has become a primary tool in neuroscience, many test-retest reliability studies in humans have been published. On network level, the frontoparietal, default-mode networks, visual and sensorimotor networks are considered to be the most reliable regarding test-retest reliability (164-166). Subcortical networks are the least reliable networks (165, 167). Test-retest reliability of functional connectivity can be influenced by different factors such as age (168), physiological noise (respiration, cardiac processes) (169), head motion (170), and scan duration (171). Furthermore, repeated measurements acquired over shorter test-retest intervals are more reliable than those over longer (165). Preprocessing steps to reduce the contribution of noise, such as the regression of head motion, global brain signal, and white matter, tend to decrease reliability (172, 173).

5.2.2 Investigation of Molecular and Functional Changes in an α-synuclein Rat Model of Parkinson disease

Studying the link between molecular neurotransmitter-receptor interactions and functional neural mechanisms using a pharmacological intervention contributes to understanding the drug mechanism in healthy and diseased brains. Here, we show that presynaptic dysfunction impacts functional connectivity in dopamine-rich, subcortical, and cortical regions after amphetamine-induced dopamine release.

5.2.2.1 [^{11}C]Raclopride Binding Reveals a Decrease post *d*-Amphetamine Stimulation and D_2 Receptor Occupancy Changes in the AAV- αSYN Rats

Previous studies showed that changes in neurotransmitter concentrations can be measured with PET using the principle of competition between the endogenous neurotransmitter and the radioligand by applying a pharmacological stimulation (66, 68). This technique has been primarily applied to the dopaminergic system using the D_2 receptor tracer [^{11}C]raclopride (174, 175) but was also applied to other neurotransmitter systems such as 5-HT receptor radioligands (176, 177) or norepinephrine (178, 179). Our study used *d*-amphetamine to modulate the dopamine concentration in healthy rats and in a rat model overexpressing αSYN. The αSYN overexpressing model has been previously investigated in a longitudinal multitracer PET imaging study to analyze pre- and postsynaptic changes [unpublished data]. The study showed that postsynaptic D_2 receptor occupancy changes provided the most reliable imaging readout for the αSYN pathology since [^{11}C]raclopride binding was consistently increased in AAV-αSYN rats but unaffected in AAV-GFP rats, which could be replicated in our study.

In the present study, the TACs of the CoNaCl group show no alteration after the application of NaCl compared to the Control group, which shows a reduction in the [^{11}C]raclopride binding in the CPu as well as in the cerebellum after *d*-amphetamine application. To explain changes in synaptic neurotransmission, literature describes two theoretical models: the competition and internalization model (66, 68). The competition model describes that after increasing the synaptic dopamine concentration, the occupancy of the D_2 receptor increases, resulting in a decreased D_2 receptor availability for the radioligand and *vice versa*. The internalization model modulates the cell surface expression of G protein-coupled receptors by agonist-induced challenges resulting in externalized or internalized receptors on the plasma membrane. Under stimulated conditions, the increased neurotransmitter release will trigger receptor internalization, leading to decreased

radioligand binding due to the reduced affinity for the internalized receptor, reduced available binding sites, or both (66, 68). Our [^{11}C]raclopride PET data shows a clear molecular modulation due to amphetamine-induced dopamine release in healthy rats, leading to reduced radioligand binding. The reduction could originate from decreased D_2 receptor availability or agonist-induced internalization. However, the DVR-1 in the Control group showed only a significant decrease in the time interval T_3, which was also seen in the CoNaCl group. We hypothesized that the reduction in the DVR-1 in the Control group would be higher. Since not only the TACs of the CPu showed a decrease of [^{11}C]raclopride binding but also the cerebellum, the effect of *d*-amphetamine cancels out after the calculation of the DVR-1 leading to an underestimation of the specific binding. In rats (155, 180), non-human primates (181, 182), and humans (183, 184), the cerebellum has been used as a reference region. No [^{11}C]raclopride binding to D_2 receptors in the cerebellum was observed in any of these studies. However, this may vary depending on the species used. Despite the low *d*-amphetamine concentration, some animals needed to be excluded from the study due to motion during the acquisition, reducing the number of animals. Further, since the cerebellum also showed a reduction in [^{11}C]raclopride binding after the *d*-amphetamine application in this model, it is not an ideal reference region for the calculation of the DVR-1 and to see changes in dopamine release. Other analysis methods and models independent of a reference region should be considered in future studies to analyze changes in dopamine release. For example, Lippert *et al.* developed a novel approach to analyze temporal fluctuations of extrasynaptic dopamine release using [^{11}C]raclopride in striatal and extrastriatal brain regions (185). They revealed that dopamine release on the synapse induces low frequency differences of extrasynaptic extracellular dopamine levels, which can be detected in the [^{11}C]raclopride signal.

Further, the DVR-1 curve of the CoNaCl group was higher than the DVR-1 curve of the Control group, which was related to the difference in the [^{11}C]raclopride molar activity of both groups: 108.0 ± 22.6 GBq/µmol for the CoNaCl group and 75.3 ± 19.8 GBq/µmol for the Control group. The molar activity of the Control group was lower, meaning more unlabeled raclopride could occupy the D_2 receptors, decreasing the sensitivity of dopamine.

In the AAV-αSYN-injected CPu, dopamine release after the *d*-amphetamine stimulation was not quantifiable because no equilibrium was reached in the DVR-1 during baseline. However, similar to the Control group, no changes in [^{11}C]raclopride binding could be observed in the non-injected CPu. To analyze the percentage changes of the BP_{ND} values

after stimulation compared to baseline, the BP_{ND} is required to reach equilibrium. However, in the AAV-αSYN injected CPu, the equilibrium was not reached before the pharmacological stimulation. We hypothesize that unilateral dopaminergic degeneration leads to dopamine depletion, decreased dopamine occupancy, and increased binding site availability, causing [^{11}C]raclopride binding to require more time to reach its equilibrium. Although the short half-life of the carbon-11 isotope hindered longer acquisitions due to a PET signal-to-noise ratio decrease at later time points, applying the *d*-amphetamine stimulation later in the scan could have been a potential solution. Further work is necessary to optimize bolus plus constant infusion protocols and find suitable parameters that enable early tracer equilibrium for both healthy and diseased cohorts and thus evaluate a pharmacological stimulation for all cohorts under the same protocol. The AAV-GFP group showed a reduction in [^{11}C]raclopride binding evaluated for both CPus, which was significant at T_3 due to amphetamine-induced dopamine release, in agreement with the Control group. This indicates that overexpression of GFP did not lead to increased D2 receptor expression on the post-synaptic membrane.

In our study, we observed a consistent increase in [^{11}C]raclopride binding in the AAV-αSYN injected CPu as in our previous study, pointing to a D_2 receptor occupancy change or an upregulation of the D_2 receptors. Two rats showed less than 10% change between the injected and non-injected CPu and were excluded from the study. The reason for this could be that the αSYN virus was not injected directly in the substantia nigra and therefore was not overexpressed. The other rats in the study showed a change of 20.5 ± 3.8 % between the injected and non-injected CPu.

This is in line with previous studies using the 6-hydroxydopamine (6-OHDA) model, which is a toxin-induced rat model of PD by unilateral injection of the neurotoxin 6-OHDA into the substantia nigra resulting in dopamine depletion (186, 187). The consequence is an increased dopamine receptor availability to compensate for the decreased dopamine concentration, resulting in an increased [^{11}C]raclopride binding on the lesioned side (186-188). In the study from Ngyuen *et al.*, 6-OHDA lesioned rats were measured using [^{11}C]raclopride-PET. The authors observed 19-20 % increased binding on the lesioned side, confirming a loss of presynaptic dopamine terminals causing upregulation of D_2 receptors in the CPu on the lesioned side (189).

5.2.2.2 Reduced Functional Connectivity in the Dopaminergic and Default-mode Network after Application of *d*-Amphetamine

Functional connectivity in the dopaminergic network and the default-mode network during three time phases post *d*-amphetamine stimulation was investigated to elucidate amphetamine-induced network-level changes The extracellular dopamine release may affect the nigrostriatal, mesolimbic, mesocortical, and tuberoinfundibular pathways. Our study confirmed this by revealing a reduction in functional connectivity between all four pathways after the application of *d*-amphetamine, which was accentuated in later time phases. The same finding could be observed in the default-mode network; in particular, the functional connectivity between the prefrontal, frontal, and dorsolateral cortical regions was reduced. The CPu neurons project directly or indirectly to the substantia nigra and the VTA, having dopaminergic projections to the prefrontal cortex (190). Dopamine is essential in modulating these connections (191, 192). Since the mPFC contains many dopamine receptors, it is susceptible to the dopaminergic environment (193). After applying multiple comparison correction, the default-mode network reveals less significant reduced functional connectivity. However, there is still a significant reduction in the functional connectivity between the mPFC and Cg and between the mPFC and the PaC of the default-mode network. Several potential reasons exist for the small changes in functional connectivity observed in this model. First, anesthesia has been shown to influence functional connectivity (194-196). Due to its vasodilatory effect, high levels of isoflurane suppress neural activity. However, low isoflurane levels (1-1.5%) are feasible for functional connectivity acquisition in macaques (197). Furthermore, it has been reported that functional connectivity is preserved under low doses for mice (198) and rats (199) and enables stable physiological readouts (100). Therefore, we kept the isoflurane level at 1.3% during all measurements. Additionally, α-chloralose, a widely used anesthetic agent for terminal fMRI experiments, has been shown to inhibit dopamine release in dopaminergic neurons (200). Therefore, we refrained from using α-chloralose in favor of isoflurane. However, anesthesia effects on our functional connectivity analysis cannot be completely excluded from this study. Finding a suitable anesthesia protocol for simultaneous PET/fMRI experiments, which has a minor impact on functional connectivity, as well as on the pharmacokinetics of the used PET tracer, represents one of the major methodological challenges for future studies with similar designs. Further, the BOLD signal is influenced by cerebral blood flow, cerebral blood volume, and blood oxygenation. *D*-amphetamine has a vasoconstrictive effect via dopamine receptors on the microvessels in the

brain (201), which could lead to vascular contributions in our study. Furthermore, *d*-amphetamine can induce vascular effects, e.g., increased blood pressure (202), which could also affect the neuronal response. However, to avoid/overcome these issues, we excluded the five minutes directly after the *d*-amphetamine stimulation from our analysis. Additionally, previous studies, such as Ren *et al.* published in 2009, indicated that *d*-amphetamine concentrations up to 1 mg/kg do not alter blood pressure (203), which is an indication of the mainly neuronal substrate of the effects reported in our study. Last, due to the exclusion of several animals, the number of animals in the Control group was only ten, based on the test-retest data too low to achieve reliable results.

The human trial of Schrantee *et al.* is in line with the results of our study. They reported that acute *d*-amphetamine administration reduces functional connectivity in the cortico-striatal-thalamic network and the default-mode network, which aligns with our examination (204). Studies on the neuronal effects of *d*-amphetamine in animals are sparse. However, alterations of neural activity reported previously (189, 205-208) comprised similar areas to the effects on functional connectivity as in the present study, including dopamine-rich, subcortical, and cortical regions. Chen *et al.* examined the utility of phMRI to investigate neurotransmitter-induced activation in rats with 3 mg/kg *d*-amphetamine by measuring signal intensity in gradient echo images using a contrast agent (208). The results showed increased signal intensity post *d*-amphetamine stimulation in brain areas with high dopamine receptor density, such as the frontal cortex, CPu, cingulate cortex, and parietal cortex (208). The animal study from Schwarz *et al.* examined functional connectivity patterns underlying the cerebral blood volume response to *d*-amphetamine (1 mg/kg) stimulation in rats (206). They analyzed intersubject correlations of the *d*-amphetamine response and performed cluster analysis revealing different networks which show strongly connected responses: connections between the CPu and the MB, including VTA and substantia nigra and between frontal cortical regions to the basal ganglia regions and midbrain (206). Through the employed methodology, our study adds important complementary insight into the effects of *d*-amphetamine. We showed that in addition to the activity changes shown previously, the integrity of the functional connectome is strongly affected by *d*-amphetamine in rats. Remarkably, these changes already occur at considerably lower physiological doses of *d*-amphetamine (0.5 mg/kg) compared to the previous reports (e.g. 3 mg/kg (208)), thus elucidating the acute effects of *d*-amphetamine not only as an illegal drug but also as a therapeutic agent given in attention deficit disorder (ADHD) and other diseases such as narcolepsy (209) and depression (210). Further, the

applied dosage in our study is in the recommended dosage range (0.3-1.5 mg/kg) for ADHD patients (211). Another medication recommended for the treatment of ADHD is methylphenidate, which has comparable pharmacological effects to *d*-amphetamine (212). One hallmark of ADHD is increased activity in the default-mode network during cognitive tasks compared to healthy controls (213) which can be suppressed, particularly between frontoparietal areas, by applying methylphenidate (214). Since *d*-amphetamine also affects other neurotransmitter systems, such as norepinephrine or serotonin, additional neurotransmitter-releasing drugs or reuptake blockers can be discussed in this context. 3,4-methylenedioxymethamphetamine (MDMA), a serotonin-norepinephrin-dopamine releasing agent, decreases functional connectivity in the visual, default-mode, and sensorimotor network (214). Ketamine, a dopamine-noradrenalin reuptake inhibitor, used as a treatment option for depression, decreases the activity in the default-mode network, which is pathologically increased in patients with depression (215). All these studies are in strong agreement with our results showing a reduction in functional connectivity after amphetamine-induced dopamine release in the default-mode network, in particular between the mPFC, the Cg, and the OFC and also between the mPFC, the Amyg, and Hyp in healthy rats.

5.2.2.3 Presynaptic Dysfunction Reduces Effects of *d*-Amphetamine in the AAV-αSYN Parkinson's Disease Model

In our study, the effects of *d*-amphetamine in connection strengths between the mPFC and the nigrostriatal, mesolimbic, and tuberoinfundibular pathways and between the mPFC, Cg, and OFC in the default-mode network reported for the healthy Control cohort could not be observed in the AAV-αSYN lesioned rats. While our data indicate a functional connectivity decrease between the mPFC and the OFC in the AAV-αSYN cohort, it was less prominent than in the Control rats. Our results reveal a weaker reduction of functional connectivity in the AAV-αSYN cohort. We hypothesize that due to the dopaminergic degeneration of the presynapse, less dopamine is released into the synaptic cleft and, therefore, lower dopamine changes in the CPu leading to lower alteration in the prefrontal cortex. However, the AAV-GFP group also displays a weaker decrease in functional connectivity compared to the Control rats despite no change in [^{11}C]raclopride binding. A longitudinal multitracer PET imaging study also investigated presynaptic changes, showing decreased dopamine transporter and vesicular monoamine transporter 2 [unpublished data], suggesting only a presynaptic effect of GFP overexpression. It

remains unexplained and requires further investigation as to why we have dopamine release despite the presynaptic dysfunction but still have reduced functional connectivity.

Several other fMRI studies on the 6-OHDA model reveal a loss in cortical response of the lesioned side after *d*-amphetamine stimulation, indicating dependence between cortical hemodynamic response and striatal dopamine activity (208, 216). Interestingly, the amphetamine-induced reduction of functional connectivity in the AAV-αSYN group was symmetrical, indicating the pronounced functional integration of the two hemispheres, despite the molecular-level asymmetry confirmed by the left-right difference observed in [^{11}C]raclopride-PET binding.

Until today, several studies characterized the 6-OHDA model using resting-state functional connectivity (217-219), indicating contradicting results. Monnot *et al.* found a functional asynchrony between the intact and the lesioned CPu due to asymmetric degeneration of the nigrostriatal dopamine pathway and increased synchrony between the lesioned CPu and sensorimotor cortices of both hemispheres (217). Another study by Westphal *et al.* performed graph theoretical analysis observing no significant regional differences in the global network measures in the 6-OHDA. This observation might be related to the unilateral nature of this model leading to compensatory mechanisms in the non-lesioned/contralateral hemisphere, which may cancel any change in functional connectivity in the ipsilateral hemisphere (218). However, analysis of local functional changes revealed that the 6-OHDA rats are characterized by a predominantly reduced functional connectivity in the cortex on the lesioned side and increased functional connectivity in the ipsilateral and contralateral subcortical areas (218). Perlbarg *et al.* observed increased functional connectivity in ipsilateral- and contralateral-lesioned regions of the cortico-basal ganglia network pathway, including the motor cortex, globus pallidus, and the CPu (219). Our data complement the findings of these studies by revealing the functional connectivity response in a model involving a unilateral dopaminergic lesion and *d*-amphetamine as a dopamine-releasing agent.

5.2.2.4 Nigrostriatal Dopaminergic Integrity is essential for Cortical Connectivity Modulation by *d*-Amphetamine

Our study revealed that presynaptic dysfunction reduces network-level functional responses to a potent dopamine-releasing agent, particularly in frontal cortical areas. In healthy controls, the dopamine release detected with [^{11}C]raclopride following *d*-amphetamine stimulation was complemented by strong functional connectivity reductions

between all four dopaminergic pathways, as well as between the mPFC and all other frontal cortical regions in the default-mode network revealed by fMRI. In contrast, no dopamine release could be detected in the AAV-αSYN cohort, which also translated into the minor effects observed in the functional connectivity of prefrontal regions. However, AAV-GFP also showed minor effects in the functional connectivity despite dopamine release detected with [^{11}C]raclopride. Previous rat studies indicated decreased cortical activity induced by dopamine depletion (189, 208, 216). The spatial extent of the observed changes agrees with our study. Additionally, our study demonstrates that functional connectivity after *d*-amphetamine administration is also affected by dopamine depletion, giving us complementary insight into the effects of unilateral nigrostriatal dopamine depletion.

In humans, it has been reported that PD patients show a functional disconnection of the striato-thalamo-frontal loop, resulting in impaired modulation of frontal cortical activity. In 1989, Albin *et al.* proposed the hypothesis that excessive inhibitory output from basal ganglia to cortex via the thalamus was responsible for both bradykinesia and cortical hypoactivity (220). Another study described a dysfunction of the default-mode network in PD patients compared to healthy subjects between the medial prefrontal cortex and the rostral ventromedial caudate nucleus, which may be related to dopamine depletion (82). Monchi *et al.* have investigated the relationship between cortical activation and the CPu. They revealed that PD patients have decreased cortical activation while performing a task involving the caudate nucleus compared to healthy subjects (221), implying that the nigrostriatal and mesocortical pathways are involved.

Besides classical motor symptoms, PD patients also suffer from neuropsychological and emotional deficits. The Amyg is the brain area responsible for emotional processing and is stimulated by dopamine. Our study observed a clear reduction of functional connectivity for the Amyg post *d*-amphetamine stimulation in the healthy Control cohort, pointing to a clear modulation of the Amyg by dopamine. Interestingly, only minor effects on the functional connectivity in the Amyg could be observed in the AAV-αSYN cohort. The study of Tessitore *et al.* investigated the response of the Amyg to dopaminergic therapy, comparing healthy controls and PD patients (222). In the hypodopaminergic state, no response of the Amyg was seen in PD while performing an emotional task compared to healthy controls (222). This perfectly agrees with our study, revealing a less functional connectivity effect on the Amyg after dopamine depletion in the AAV-αSYN cohort. We

complement Tessitore et al.'s findings by clearly showing that nigrostriatal dopamine depletion nearly abolishes the effects of *d*-amphetamine on the connectivity of the Amyg.

6 Conclusion

This work aimed to use different non-invasive imaging methods to detect the underlying cellular pathology of synucleinopathies to enable differential diagnosis and monitoring of disease progression or disease-modifying treatments. Since a specific PET tracer to detect αSYN pathology at an early disease stage is still missing, and no systemic *in vivo* work has been carried out to link the synaptic dysfunctions induced by the pathology to functional changes, we pursued two objectives with this work:

1. Evaluating the binding affinity of four different chemical compounds to αSYN pathology *in vitro* in binding experiments and the *in vivo* evaluation of one compound, MODAG-001, to αSYN aggregates.
2. Studying the link between molecular neurotransmitter-receptor interactions and functional neural mechanisms in a rat model overexpressing αSYN pathology using a pharmacological intervention.

After screening different chemical compounds, MODAG-001 fulfilled several essential criteria for a CNS PET tracer targeting αSYN. It revealed high binding to αSYN fibrils, good pharmacokinetics, and good brain penetration in healthy mice. However, MODAG-001 showed high non-specific binding. In the metabolite analysis of [^{11}C]MODAGA-001, its precursor, MODAG-005, was observed to cross the blood-brain barrier. MODAG-005 was therefore tested on human brain sections to investigate the binding properties displaying binding to aggregates in PD and AD cases. To further investigate the binding of MODAG-005 to pathological aggregates, a cross-validation to immunofluorescence stained consecutive sections and microautoradiography needs to be performed in future studies.

Over the past years, many attempts to develop an αSYN specific PET tracer have been made. Since there is a low abundance of αSYN inclusions in brain regions, mixed pathology, and high similarity to structurally related proteins present in pathological brain regions, the discovery of a PET tracer for αSYN is very challenging. The results of this work show the importance of a good workflow to evaluate promising candidates as PET tracers targeting αSYN starting from *in vitro* binding assays, *in vivo* pharmacokinetic and metabolite analysis in mice, as well as screening of the binding to different proteinopathies containing αSYN pathology.

To enable the understanding of dopamine depletion caused by αSYN overexpressing and then link molecular neurotransmitter-receptor interactions to functional neural

mechanisms, an indirect simultaneous multimodal imaging approach using [^{11}C]raclopride-PET/BOLD-fMRI together with a pharmacological *d*-amphetamine stimulation was used to investigate an αSYN overexpressing rat model. The results indicate that nigrostriatal dopamine depletion impacts functional connectivity in dopamine-rich, subcortical, and cortical regions after amphetamine-induced dopamine release.

This simultaneous multimodal imaging approach reliably provides *in vivo* molecular-level information on neurotransmitter-receptor interactions and their influence on functional connectivity by modulating the neurotransmitter dopamine. This is the first study investigating a rat model of Parkinson's disease with the simultaneous [^{11}C]raclopride-PET/BOLD-phMRI method applying a pharmacological stimulation using *d*-amphetamine within the same measurement. The results indicate that nigrostriatal dopamine depletion leads to a reduced response in functional connectivity in dopamine-rich and cortical areas in a rat model of Parkinson's disease.

Our research demonstrates that there is a decrease in functional connectivity within the default-mode network after dopamine release induced by *d*-amphetamine. This has been observed in humans for *d*-amphetamine and for other drugs that have a similar pharmacological effect, such as methylphenidate or drugs that affect the same neurotransmitter system, such as MDM. Further, nigrostriatal dopamine depletion caused by the overexpression of αSYN in our study reveals a decreased response in functional connectivity, which is in line with other unilateral Parkinson's disease rat models such as the 6-OHDA model. Interestingly, this amphetamine-induced reduction was observed in both hemispheres despite the unilateral injection of the AAV- αSYN virus and the molecular-level asymmetry found by [^{11}C]raclopride-PET. This elucidates the tremendous benefit of combining these two imaging modalities. Using simultaneous [^{11}C]raclopride-PET/BOLD-fMRI, it is possible to investigate the brain on functional and on molecular-level revealing complementary information.

7 Contributions

All the experiments of this thesis were carried out in the Department of Preclinical Imaging and Radiopharmacy at the University in Tübingen under the supervision of Prof. Dr. Kristina Herfert. The experiments of the binding experiments on αSYN fibrils as well as the autoradiography experiments on mouse and human brain sections in part one of this thesis were designed, performed and evaluated by me after consultation with Prof. Dr. Kristina Herfert as described under "Material and Methods". The pharmacokinetic and metabolite study was planned, conducted and analyzed by Sabrina Haas as part of her master's thesis under my supervision, after consultation with Prof. Dr. Kristina Herfert as described under "Material and Methods". The experiment on the A30P mice was planned, carried out by and analyzed by Sabrina Haas as part of her master's thesis under my supervision. All *in vivo* experiments in part two of this thesis were planned and prepared by me after consultation with Prof. Dr. Kristina Herfert as described under "Material and Methods" as well as performed by me with the temporary support of Sabrina Haas, Linda Schramm and Maren Harant. The evaluation and analysis of the *in vivo* experiments were carried out by me with MATLAB programs, which were provided by Dr. Tudor Ionescu.

The lead compound anle138b and its chemical derivates anle2F4CP, sery383, sery512a, MODAG-001, and MODAG-005 were kindly provided from our cooperation partners Dr. Sergey Ryazanov and Dr. Andrei Leonov of the Department of NMR-based Structural Biology at the Max Planck Institute for Biophysical Chemistry in Göttingen, Germany. Further, these compounds were tritiated from RC Tritec (Teufen, Switzerland).

The αSYN fibrils kindly provided by our cooperation partner Dr. Felix Schmidt from MODAG GmbH in Wendelsheim, Germany.

The human brain sections were kindly provided by Neurobiobank Munich, Germany.

The synthesis of [^{11}C]MODAG-001 and [^{11}C]raclopride were performed and provided by the Imaging Probe Development Group (Dr. Andreas Maurer) of the Werner Siemens Imaging Center

8 Publications

[1] Kuebler L.*, Buss, S.*, Leonov A.*, Ryazanov S.*, Schmidt F.*, Mauer A., Weckbecker D., Landau A.M., Lillethrorup T.P., Bleher D., Saw R.S., Pichler B.J., Griesinger C., Giese A., Herfert K. [^{11}C]MODAG-001 – Towards a PET Tracer Targeting α-Synuclein Aggregates. EJNMMI 2020. Dec 28 doi: 10.1007/s00259-020-05133-x.

*equally contributed

[2] Maurer A., Leonov A., Ryazanov S., Herfert K., Kuebler L., Buss S., Schmidt F., Weckbecker D., Linder R., Bender D., Giese A., Pichler B.J., Griesinger C. 11C Radiolabeling of anle253b: A Putative PET Tracer for Parkinson´s Disease That Binds to α-synuclein fibrils in vitro and Crosses the Blood-Brain Barrier. ChemMedChem. 2020. March; 15(5):411-415.

[3] Herfert K., Mannheim J.G., Kuebler L., Marciano S., Amend M., Parl C., Napieczynska H., Maier F.M., Vega S.C., Pichler B.J. Quantitative Rodent Brain Receptor Imaging. Mol Imaging Biol. 2020 Apr;22(2):223-244.

Book chapter:

Herfert K., Marciano S., Kuebler L., Buss S., Landeck N., Mannheim J.G., Napieczynska H. Chapter 34: Preclinical Experimentation (Neurology). Radiopharmaceutical Chemistry. Eds: Lewis JS, Windhorst AD, Zeglis BM. Springer International Publishing; ISBN 978-3-319-98947-1, 2019.

9 References

1. Kandel ER, Schwartz JH, Jessell TH, Siegelbaum SA, Hudspeth AJ. Prinicple of neural science. 5th ed: The McGraw-Hill Companies; 2013. 1706 p.

2. Lanciego JL, Luquin N, Obeso JA. Functional neuroanatomy of the basal ganglia. Cold Spring Harb Perspect Med. 2012;2(12):a009621.

3. Bridi JC, Hirth F. Mechanisms of alpha-Synuclein Induced Synaptopathy in Parkinson's Disease. Front Neurosci. 2018;12:80.

4. Alafuzoff I, Hartikainen P. Alpha-synucleinopathies. Handb Clin Neurol. 2017;145:339-53.

5. Nelson AB, Kreitzer AC. Reassessing models of basal ganglia function and dysfunction. Annu Rev Neurosci. 2014;37:117-35.

6. Grillner S, Robertson B. The Basal Ganglia Over 500 Million Years. Curr Biol. 2016;26(20):R1088-R100.

7. Carlsson A, Lindqvist M, Magnusson T. 3,4-Dihydroxyphenylalanine and 5-hydroxytryptophan as reserpine antagonists. Nature. 1957;180(4596):1200.

8. Beaulieu JM, Gainetdinov RR. The physiology, signaling, and pharmacology of dopamine receptors. Pharmacol Rev. 2011;63(1):182-217.

9. Elsworth JD, Roth RH. Dopamine synthesis, uptake, metabolism, and receptors: relevance to gene therapy of Parkinson's disease. Exp Neurol. 1997;144(1):4-9.

10. Jackson DM, Westlind-Danielsson A. Dopamine receptors: molecular biology, biochemistry and behavioural aspects. Pharmacol Ther. 1994;64(2):291-370.

11. Kuebler L. Imaging Synucleinopathies – An In Vivo and In Vitro Evaluation of Potential New PET Tracers [Master thesis]2016.

12. Eriksen J, Jorgensen TN, Gether U. Regulation of dopamine transporter function by protein-protein interactions: new discoveries and methodological challenges. J Neurochem. 2010;113(1):27-41.

13. Parkinson J. An essay on the shaking palsy. 1817. J Neuropsychiatry Clin Neurosci. 2002;14(2):223-36; discussion 2.

14. Dauer W, Przedborski S. Parkinson's disease: mechanisms and models. Neuron. 2003;39(6):889-909.

15. Henderson MX, Trojanowski JQ, Lee VM. alpha-Synuclein pathology in Parkinson's disease and related alpha-synucleinopathies. Neurosci Lett. 2019;709:134316.

16. Irwin DJ, Lee VM, Trojanowski JQ. Parkinson's disease dementia: convergence of alpha-synuclein, tau and amyloid-beta pathologies. Nat Rev Neurosci. 2013;14(9):626-36.

17. Lewy FH. Paralysis agitans. Part I: Pathologische Anatomie. Handbuch der Neurologie III: Springer, Berlin; 1912. p. 920-33.

18. Jellinger KA, Korczyn AD. Are dementia with Lewy bodies and Parkinson's disease dementia the same disease? BMC Med. 2018;16(1):34.

19. Spillantini MG, Goedert M. The alpha-synucleinopathies: Parkinson's disease, dementia with Lewy bodies, and multiple system atrophy. Ann N Y Acad Sci. 2006;920:16-27.

20. Yang W, Yu S. Synucleinopathies: common features and hippocampal manifestations. Cell Mol Life Sci. 2017;74(8):1485-501.

21. Twohig D, Nielsen HM. alpha-synuclein in the pathophysiology of Alzheimer's disease. Mol Neurodegener. 2019;14(1):23.

22. Chung DC, Roemer S, Petrucelli L, Dickson DW. Cellular and pathological heterogeneity of primary tauopathies. Mol Neurodegener. 2021;16(1):57.

23. Moussaud S, Jones DR, Moussaud-Lamodiere EL, Delenclos M, Ross OA, McLean PJ. Alpha-synuclein and tau: teammates in neurodegeneration? Mol Neurodegener. 2014;9:43.

24. Bourdenx M, Koulakiotis NS, Sanoudou D, Bezard E, Dehay B, Tsarbopoulos A. Protein aggregation and neurodegeneration in prototypical neurodegenerative diseases: Examples of amyloidopathies, tauopathies and synucleinopathies. Prog Neurobiol. 2017;155:171-93.

25. Burre J, Sharma M, Tsetsenis T, Buchman V, Etherton MR, Sudhof TC. Alpha-synuclein promotes SNARE-complex assembly in vivo and in vitro. Science. 2010;329(5999):1663-7.

26. Tyedmers J, Mogk A, Bukau B. Cellular strategies for controlling protein aggregation. Nat Rev Mol Cell Biol. 2010;11(11):777-88.

27. Olanow CW, Perl DP, DeMartino GN, McNaught KS. Lewy-body formation is an aggresome-related process: a hypothesis. Lancet Neurol. 2004;3(8):496-503.

28. Shahmoradian SH, Lewis AJ, Genoud C, Hench J, Moors TE, Navarro PP, et al. Lewy pathology in Parkinson's disease consists of crowded organelles and lipid membranes. Nat Neurosci. 2019;22(7):1099-109.

29. Kruger R, Kuhn W, Muller T, Woitalla D, Graeber M, Kosel S, et al. Ala30Pro mutation in the gene encoding alpha-synuclein in Parkinson's disease. Nat Genet. 1998;18(2):106-8.

30. Polymeropoulos MH, Lavedan C, Leroy E, Ide SE, Dehejia A, Dutra A, et al. Mutation in the alpha-synuclein gene identified in families with Parkinson's disease. Science. 1997;276(5321):2045-7.

31. Zarranz JJ, Alegre J, Gomez-Esteban JC, Lezcano E, Ros R, Ampuero I, et al. The new mutation, E46K, of alpha-synuclein causes Parkinson and Lewy body dementia. Ann Neurol. 2004;55(2):164-73.

32. Martin LJ, Pan Y, Price AC, Sterling W, Copeland NG, Jenkins NA, et al. Parkinson's disease alpha-synuclein transgenic mice develop neuronal mitochondrial degeneration and cell death. J Neurosci. 2006;26(1):41-50.

33. Taguchi T, Ikuno M, Hondo M, Parajuli LK, Taguchi K, Ueda J, et al. alpha-Synuclein BAC transgenic mice exhibit RBD-like behaviour and hyposmia: a prodromal Parkinson's disease model. Brain. 2020;143(1):249-65.

34. Wakamatsu M, Ishii A, Iwata S, Sakagami J, Ukai Y, Ono M, et al. Selective loss of nigral dopamine neurons induced by overexpression of truncated human alpha-synuclein in mice. Neurobiol Aging. 2008;29(4):574-85.

35. Freichel C, Neumann M, Ballard T, Muller V, Woolley M, Ozmen L, et al. Age-dependent cognitive decline and amygdala pathology in alpha-synuclein transgenic mice. Neurobiol Aging. 2007;28(9):1421-35.

36. Neumann M, Kahle PJ, Giasson BI, Ozmen L, Borroni E, Spooren W, et al. Misfolded proteinase K-resistant hyperphosphorylated alpha-synuclein in aged transgenic mice with locomotor deterioration and in human alpha-synucleinopathies. J Clin Invest. 2002;110(10):1429-39.

37. Kirik D, Rosenblad C, Burger C, Lundberg C, Johansen TE, Muzyczka N, et al. Parkinson-like neurodegeneration induced by targeted overexpression of alpha-synuclein in the nigrostriatal system. J Neurosci. 2002;22(7):2780-91.

38. Ulusoy A, Sahin G, Bjorklund T, Aebischer P, Kirik D. Dose optimization for long-term rAAV-mediated RNA interference in the nigrostriatal projection neurons. Mol Ther. 2009;17(9):1574-84.

39. Kirik D, Annett LE, Burger C, Muzyczka N, Mandel RJ, Bjorklund A. Nigrostriatal alpha-synucleinopathy induced by viral vector-mediated overexpression of human alpha-synuclein: a new primate model of Parkinson's disease. Proc Natl Acad Sci U S A. 2003;100(5):2884-9.

40. Chung HK, Ho HA, Perez-Acuna D, Lee SJ. Modeling alpha-Synuclein Propagation with Preformed Fibril Injections. J Mov Disord. 2019;12(3):139-51.

41. Yuan H, Zhang ZW, Liang LW, Shen Q, Wang XD, Ren SM, et al. Treatment strategies for Parkinson's disease. Neurosci Bull. 2010;26(1):66-76.

42. Birkmayer W, Hornykiewicz O. [The L-3,4-dioxyphenylalanine (DOPA)-effect in Parkinson-akinesia]. Wien Klin Wochenschr. 1961;73:787-8.

43. Factor SA. Current status of symptomatic medical therapy in Parkinson's disease. Neurotherapeutics. 2008;5(2):164-80.

44. Faggiani E, Benazzouz A. Deep brain stimulation of the subthalamic nucleus in Parkinson's disease: From history to the interaction with the monoaminergic systems. Prog Neurobiol. 2017;151:139-56.

45. Mandler M, Valera E, Rockenstein E, Weninger H, Patrick C, Adame A, et al. Next-generation active immunization approach for synucleinopathies: implications for Parkinson's disease clinical trials. Acta Neuropathol. 2014;127(6):861-79.

46. Masliah E, Rockenstein E, Mante M, Crews L, Spencer B, Adame A, et al. Passive immunization reduces behavioral and neuropathological deficits in an alpha-synuclein transgenic model of Lewy body disease. PLoS One. 2011;6(4):e19338.

47. Pena-Diaz S, Garcia-Pardo J, Ventura S. Development of Small Molecules Targeting alpha-Synuclein Aggregation: A Promising Strategy to Treat Parkinson's Disease. Pharmaceutics. 2023;15(3).

48. Antonschmidt L, Matthes D, Dervisoglu R, Frieg B, Dienemann C, Leonov A, et al. The clinical drug candidate anle138b binds in a cavity of lipidic alpha-synuclein fibrils. Nat Commun. 2022;13(1):5385.

49. Fellner L, Kuzdas-Wood D, Levin J, Ryazanov S, Leonov A, Griesinger C, et al. Anle138b Partly Ameliorates Motor Deficits Despite Failure of Neuroprotection in a Model of Advanced Multiple System Atrophy. Front Neurosci. 2016;10:99.

50. Heras-Garvin A, Weckbecker D, Ryazanov S, Leonov A, Griesinger C, Giese A, et al. Anle138b modulates alpha-synuclein oligomerization and prevents motor decline and neurodegeneration in a mouse model of multiple system atrophy. Mov Disord. 2019;34(2):255-63.

51. Levin J, Schmidt F, Boehm C, Prix C, Botzel K, Ryazanov S, et al. The oligomer modulator anle138b inhibits disease progression in a Parkinson mouse model even with treatment started after disease onset. Acta Neuropathol. 2014;127(5):779-80.

52. Qin K, Zhao L, Solanki A, Busch C, Mastrianni J. Anle138b prevents PrP plaque accumulation in Tg(PrP-A116V) mice but does not mitigate clinical disease. J Gen Virol. 2019;100(6):1027-37.

53. Wagner J, Ryazanov S, Leonov A, Levin J, Shi S, Schmidt F, et al. Anle138b: a novel oligomer modulator for disease-modifying therapy of neurodegenerative diseases such as prion and Parkinson's disease. Acta Neuropathol. 2013;125(6):795-813.

54. Wegrzynowicz M, Bar-On D, Calo L, Anichtchik O, Iovino M, Xia J, et al. Depopulation of dense alpha-synuclein aggregates is associated with rescue of dopamine neuron dysfunction and death in a new Parkinson's disease model. Acta Neuropathol. 2019;138(4):575-95.

55. Deeg AA, Reiner AM, Schmidt F, Schueder F, Ryazanov S, Ruf VC, et al. Anle138b and related compounds are aggregation specific fluorescence markers and reveal high affinity binding to alpha-synuclein aggregates. Biochim Biophys Acta. 2015;1850(9):1884-90.

56. Orlovskaya VV, Fedorova OS, Viktorov NB, Vaulina DD, Krasikova RN. One-Pot Radiosynthesis of [(18)F]Anle138b-5-(3-Bromophenyl)-3-(6-[(18)F]fluoro-benzo[d][1,3]dioxol-5-yl)-1H-pyrazole-A Potential PET Radiotracer Targeting alpha-Synuclein Aggregates. Molecules. 2023;28(6).

57. Herfert KM, S. Kuebler, L. Buss, S. Landeck, N. Mannheim, J. G. Napieczynska, H. Preclinical Experimentation in Neurology. In: Lewis JS, Windhorst AD, Zeglis BM, editors. Radiopharmaceutical Chemistry: Springer Nature Switzerland; 2019. p. 583-606.

58. Griem-Krey N, Klein AB, Herth M, Wellendorph P. Autoradiography as a Simple and Powerful Method for Visualization and Characterization of Pharmacological Targets. J Vis Exp. 2019(145).

59. Johnström PB, J. L. Davenport, A. P. Quantitative Phosphor Imaging Autoradiography of Radioligand for Positron Emission Tomography. In: Davenport AP, editor. Receptor Binding Techniques: Springer Science+Business Media; 2012. p. 205-20.

60. Cherry SRD, M. PET: Physics, Instrumentation, and Scanners. In: Phelps ME, editor. PET - Molecular Imaging and Its Biological Application: Springer New York; 2004. p. 1-124.

61. Cherry SR, Gambhir SS. Use of positron emission tomography in animal research. ILAR J. 2001;42(3):219-32.

62. Bailey DL, Townsend DW, Valk PE, Maisey MN. Positron Emission Tomography: Springer London Limited; 2005.

63. Pichler BJ, Wehrl HF, Judenhofer MS. Latest advances in molecular imaging instrumentation. J Nucl Med. 2008;49 Suppl 2:5S-23S.

64. Innis RB, Cunningham VJ, Delforge J, Fujita M, Gjedde A, Gunn RN, et al. Consensus nomenclature for in vivo imaging of reversibly binding radioligands. J Cereb Blood Flow Metab. 2007;27(9):1533-9.

65. Slifstein M, Laruelle M. Models and methods for derivation of in vivo neuroreceptor parameters with PET and SPECT reversible radiotracers. Nucl Med Biol. 2001;28(5):595-608.

66. Laruelle M. Imaging synaptic neurotransmission with in vivo binding competition techniques: a critical review. J Cereb Blood Flow Metab. 2000;20(3):423-51.

67. Sulzer D, Chen TK, Lau YY, Kristensen H, Rayport S, Ewing A. Amphetamine redistributes dopamine from synaptic vesicles to the cytosol and promotes reverse transport. J Neurosci. 1995;15(5 Pt 2):4102-8.

68. Paterson LM, Tyacke RJ, Nutt DJ, Knudsen GM. Measuring endogenous 5-HT release by emission tomography: promises and pitfalls. J Cereb Blood Flow Metab. 2010;30(10):1682-706.

69. Patel S, Gibson R. In vivo site-directed radiotracers: a mini-review. Nucl Med Biol. 2008;35(8):805-15.

70. Zhang L, Villalobos A, Beck EM, Bocan T, Chappie TA, Chen L, et al. Design and selection parameters to accelerate the discovery of novel central nervous system positron emission tomography (PET) ligands and their application in the development of a novel phosphodiesterase 2A PET ligand. J Med Chem. 2013;56(11):4568-79.

71. Weishaupt D, Koechli VD, Marincek B. Wie funktioniert MRI? - Eine Einführung in Physik und Funktionsweise der Magnetreonsanzbildgebung: Springer-VErlag BErlin Heidelberg; 2014.

72. Markl M, Leupold J. Gradient echo imaging. J Magn Reson Imaging. 2012;35(6):1274-89.

73. Ogawa S, Lee TM. Magnetic resonance imaging of blood vessels at high fields: in vivo and in vitro measurements and image simulation. Magnetic resonance in medicine. 1990;16(1):9-18.

74. Ogawa S, Lee TM, Kay AR, Tank DW. Brain magnetic resonance imaging with contrast dependent on blood oxygenation. Proc Natl Acad Sci U S A. 1990;87(24):9868-72.

75. Ogawa S, Lee TM, Nayak AS, Glynn P. Oxygenation-sensitive contrast in magnetic resonance image of rodent brain at high magnetic fields. Magnetic resonance in medicine. 1990;14(1):68-78.

76. Pauling L, Coryell CD. The Magnetic Properties and Structure of Hemoglobin, Oxyhemoglobin and Carbonmonoxyhemoglobin. Proc Natl Acad Sci U S A. 1936;22(4):210-6.

77. Buxton RB. Dynamic models of BOLD contrast. Neuroimage. 2012;62(2):953-61.

78. Jonckers E, Shah D, Hamaide J, Verhoye M, Van der Linden A. The power of using functional fMRI on small rodents to study brain pharmacology and disease. Front Pharmacol. 2015;6:231.

79. Biswal B, Yetkin FZ, Haughton VM, Hyde JS. Functional connectivity in the motor cortex of resting human brain using echo-planar MRI. Magnetic resonance in medicine. 1995;34(4):537-41.

80. Tahmasian M, Bettray LM, van Eimeren T, Drzezga A, Timmermann L, Eickhoff CR, et al. A systematic review on the applications of resting-state fMRI in Parkinson's disease: Does dopamine replacement therapy play a role? Cortex. 2015;73:80-105.

81. Raichle ME, MacLeod AM, Snyder AZ, Powers WJ, Gusnard DA, Shulman GL. A default mode of brain function. Proc Natl Acad Sci U S A. 2001;98(2):676-82.

82. van Eimeren T, Monchi O, Ballanger B, Strafella AP. Dysfunction of the default mode network in Parkinson disease: a functional magnetic resonance imaging study. Arch Neurol. 2009;66(7):877-83.

83. Delaveau P, Salgado-Pineda P, Fossati P, Witjas T, Azulay JP, Blin O. Dopaminergic modulation of the default mode network in Parkinson's disease. Eur Neuropsychopharmacol. 2010;20(11):784-92.

84. Krajcovicova L, Mikl M, Marecek R, Rektorova I. The default mode network integrity in patients with Parkinson's disease is levodopa equivalent dose-dependent. J Neural Transm (Vienna). 2012;119(4):443-54.

85. Cole MW, Ito T, Cocuzza C, Sanchez-Romero R. The Functional Relevance of Task-State Functional Connectivity. J Neurosci. 2021;41(12):2684-702.

86. Biswal BB, Ulmer JL. Blind source separation of multiple signal sources of fMRI data sets using independent component analysis. J Comput Assist Tomogr. 1999;23(2):265-71.

87. Wang J, Zuo X, He Y. Graph-based network analysis of resting-state functional MRI. Front Syst Neurosci. 2010;4:16.

88. Kelly C, de Zubicaray G, Di Martino A, Copland DA, Reiss PT, Klein DF, et al. L-dopa modulates functional connectivity in striatal cognitive and motor networks: a double-blind placebo-controlled study. J Neurosci. 2009;29(22):7364-78.

89. Kuebler L, Buss S, Leonov A, Ryazanov S, Schmidt F, Maurer A, et al. [(11)C]MODAG-001-towards a PET tracer targeting alpha-synuclein aggregates. Eur J Nucl Med Mol Imaging. 2020.

90. Maier FC. Multiparametrische in vivo PET/MRT Untersuchungen zur longitudinalen Darstellung der beta-Amyloid-Ablagerungs- und rCBF-Dynamik - Bestimmung eines kausalen Zusammenhangs zwischen vaskulärer beta-Amyloidose und quantitativem rCBF-Verlust [Dissertation]2015.

91. Radde R, Bolmont T, Kaeser SA, Coomaraswamy J, Lindau D, Stoltze L, et al. Abeta42-driven cerebral amyloidosis in transgenic mice reveals early and robust pathology. EMBO Rep. 2006;7(9):940-6.

92. Sturchler-Pierrat C, Abramowski D, Duke M, Wiederhold KH, Mistl C, Rothacher S, et al. Two amyloid precursor protein transgenic mouse models with Alzheimer disease-like pathology. Proc Natl Acad Sci U S A. 1997;94(24):13287-92.

93. Mirrione MM, Schiffer WK, Fowler JS, Alexoff DL, Dewey SL, Tsirka SE. A novel approach for imaging brain-behavior relationships in mice reveals unexpected metabolic patterns during seizures in the absence of tissue plasminogen activator. Neuroimage. 2007;38(1):34-42.

94. Langer O, Nagren K, Dollé F, Lundkvist C, Sandell J, Swahn C, et al. Precursor synthesis and radiolabelling of the dopamine D2 receptor ligand (11C)raclopride from (11C)methyl triflate. Journal of Labelled Compounds and Radiopharmaceuticals. 1999;42:1183-93.

95. Van Laeken N, Kersemans K, De Meestere D, Goethals I, De Vos F. Improved HPLC purification strategy for [11C]raclopride and [11C]DASB leading to high radiochemical yields and more practical high quality radiopharmaceutical formulations. Appl Radiat Isot. 2013;78:62-7.

96. Wehrl HF, Hossain M, Lankes K, Liu CC, Bezrukov I, Martirosian P, et al. Simultaneous PET-MRI reveals brain function in activated and resting state on metabolic, hemodynamic and multiple temporal scales. Nat Med. 2013;19(9):1184-9.

97. Ionescu TM, Amend M, Hafiz R, Biswal B, Maurer A, Pichler BJ, et al. Striatal and prefrontal D2R and SERT distributions contrastingly correlate with default-mode connectivity. bioRxiv 2021.

98. Chuang KH, Lee HL, Li Z, Chang WT, Nasrallah FA, Yeow LY, et al. Evaluation of nuisance removal for functional MRI of rodent brain. Neuroimage. 2019;188:694-709.

99. Schiffer WK, Mirrione MM, Biegon A, Alexoff DL, Patel V, Dewey SL. Serial microPET measures of the metabolic reaction to a microdialysis probe implant. J Neurosci Methods. 2006;155(2):272-84.

100. Ionescu TM, Amend M, Hafiz R, Biswal B, Wehrl HF, Herfert K, et al. Elucidating the complementarity of metabolic and hemodynamic resting-state networks with simultaneous small-animal PET/MRI. Neuroimage (eingereicht, noch nicht veröffentlicht). 2020.

101. Brett M, Anton J, Valabregue R, Poline J. Region of interest analysis using an SPM toolbox [abstract] Presented at the 8th International Conference on Functional Mapping of the Human Brain, June 2-6, 2002, Sendai, Japan. Available on CD-ROM in NeuroImage, Vol 16, No 2.

102. Hume SP, Myers R, Bloomfield PM, Opacka-Juffry J, Cremer JE, Ahier RG, et al. Quantitation of carbon-11-labeled raclopride in rat striatum using positron emission tomography. Synapse. 1992;12(1):47-54.

103. Fischer K, Sossi V, von Ameln-Mayerhofer A, Reischl G, Pichler BJ. In vivo quantification of dopamine transporters in mice with unilateral 6-OHDA lesions using [C-11]methylphenidate and PET. Neuroimage. 2012;59(3):2413-22.

104. Paxinos G, Watson C. The Rat Brain in Stereotaxic Coordinates.: Academic Press, San Diego; 1998.

105. Hutchison RM, Womelsdorf T, Allen EA, Bandettini PA, Calhoun VD, Corbetta M, et al. Dynamic functional connectivity: promise, issues, and interpretations. Neuroimage. 2013;80:360-78.

106. Xia M, Wang J, He Y. BrainNet Viewer: a network visualization tool for human brain connectomics. PLoS One. 2013;8(7):e68910.

107. Fanciulli A, Wenning GK. Multiple-system atrophy. N Engl J Med. 2015;372(14):1375-6.

108. Graham JG, Oppenheimer DR. Orthostatic hypotension and nicotine sensitivity in a case of multiple system atrophy. J Neurol Neurosurg Psychiatry. 1969;32(1):28-34.

109. Clark CM, Schneider JA, Bedell BJ, Beach TG, Bilker WB, Mintun MA, et al. Use of florbetapir-PET for imaging beta-amyloid pathology. JAMA. 2011;305(3):275-83.

110. Klunk WE, Engler H, Nordberg A, Wang Y, Blomqvist G, Holt DP, et al. Imaging brain amyloid in Alzheimer's disease with Pittsburgh Compound-B. Ann Neurol. 2004;55(3):306-19.

111. Villemagne VL, Ong K, Mulligan RS, Holl G, Pejoska S, Jones G, et al. Amyloid imaging with (18)F-florbetaben in Alzheimer disease and other dementias. J Nucl Med. 2011;52(8):1210-7.

112. Korat S, Bidesi NSR, Bonanno F, Di Nanni A, Hoang ANN, Herfert K, et al. Alpha-Synuclein PET Tracer Development-An Overview about Current Efforts. Pharmaceuticals (Basel). 2021;14(9).

113. Reiner AM, Schmidt F, Ryazanov S, Leonov A, Weckbecker D, Deeg AA, et al. Photophysics of diphenyl-pyrazole compounds in solutions and alpha-synuclein aggregates. Biochim Biophys Acta Gen Subj. 2018;1862(4):800-7.

114. Maurer A, Leonov A, Ryazanov S, Herfert K, Kuebler L, Buss S, et al. (11) C Radiolabeling of anle253b: a Putative PET Tracer for Parkinson's Disease That Binds to alpha-Synuclein Fibrils in vitro and Crosses the Blood-Brain Barrier. ChemMedChem. 2019.

115. Bagchi DP, Yu L, Perlmutter JS, Xu J, Mach RH, Tu Z, et al. Binding of the radioligand SIL23 to alpha-synuclein fibrils in Parkinson disease brain tissue establishes feasibility and screening approaches for developing a Parkinson disease imaging agent. PLoS One. 2013;8(2):e55031.

116. Chen YF, Bian J, Zhang P, Bu LL, Shen Y, Yu WB, et al. Design, synthesis and identification of N, N-dibenzylcinnamamide (DBC) derivatives as novel ligands for alpha-synuclein fibrils by SPR evaluation system. Bioorg Med Chem. 2020;28(7):115358.

117. Chu W, Zhou D, Gaba V, Liu J, Li S, Peng X, et al. Design, Synthesis, and Characterization of 3-(Benzylidene)indolin-2-one Derivatives as Ligands for alpha-Synuclein Fibrils. J Med Chem. 2015;58(15):6002-17.

118. Endo H, Ono M, Takado Y, Matsuoka K, Takahashi M, Tagai K, et al. Imaging α-synuclein pathologies in animal models and patients with Parkinson’s and related diseases. 2023:2020.10.23.349860.

119. Ferrie JJ, Lengyel-Zhand Z, Janssen B, Lougee MG, Giannakoulias S, Hsieh CJ, et al. Identification of a nanomolar affinity alpha-synuclein fibril imaging probe by ultra-high throughput in silico screening. Chem Sci. 2020;11(47):12746-54.

120. Fodero-Tavoletti MT, Mulligan RS, Okamura N, Furumoto S, Rowe CC, Kudo Y, et al. In vitro characterisation of BF227 binding to alpha-synuclein/Lewy bodies. Eur J Pharmacol. 2009;617(1-3):54-8.

121. Gaur P, Galkin M, Kurochka A, Ghosh S, Yushchenko DA, Shvadchak VV. Fluorescent Probe for Selective Imaging of alpha-Synuclein Fibrils in Living Cells. ACS Chem Neurosci. 2021;12(8):1293-8.

122. Hsieh CJ, Ferrie JJ, Xu K, Lee I, Graham TJA, Tu Z, et al. Alpha Synuclein Fibrils Contain Multiple Binding Sites for Small Molecules. ACS Chem Neurosci. 2018;9(11):2521-7.

123. Hsieh CJ, Xu K, Lee I, Graham TJA, Tu Z, Dhavale D, et al. Chalcones and Five-Membered Heterocyclic Isosteres Bind to Alpha Synuclein Fibrils in Vitro. ACS Omega. 2018;3(4):4486-93.

124. Josephson L, Stratman N, Liu Y, Qian F, Liang SH, Vasdev N, et al. The Binding of BF-227-Like Benzoxazoles to Human alpha-Synuclein and Amyloid beta Peptide Fibrils. Mol Imaging. 2018;17:1536012118796297.

125. Kaide S, Watanabe H, Shimizu Y, Iikuni S, Nakamoto Y, Hasegawa M, et al. Identification and Evaluation of Bisquinoline Scaffold as a New Candidate for alpha-Synuclein-PET Imaging. ACS Chem Neurosci. 2020;11(24):4254-61.

126. Kikuchi A, Takeda A, Okamura N, Tashiro M, Hasegawa T, Furumoto S, et al. In vivo visualization of alpha-synuclein deposition by carbon-11-labelled 2-[2-(2-dimethylaminothiazol-5-yl)ethenyl]-6-[2-(fluoro)ethoxy]benzoxazole positron emission tomography in multiple system atrophy. Brain. 2010;133(Pt 6):1772-8.

127. Koga S, Ono M, Sahara N, Higuchi M, Dickson DW. Fluorescence and autoradiographic evaluation of tau PET ligand PBB3 to alpha-synuclein pathology. Mov Disord. 2017;32(6):884-92.

128. Lengyel-Zhand Z, Ferrie JJ, Janssen B, Hsieh CJ, Graham T, Xu KY, et al. Synthesis and characterization of high affinity fluorogenic alpha-synuclein probes. Chem Commun (Camb). 2020;56(24):3567-70.

129. Levigoureux E, Lancelot S, Bouillot C, Chauveau F, Verdurand M, Verchere J, et al. Binding of the PET radiotracer [(1)(8)F]BF227 does not reflect the presence of alpha-synuclein aggregates in transgenic mice. Curr Alzheimer Res. 2014;11(10):955-60.

130. Miranda-Azpiazu P, Svedberg M, Higuchi M, Ono M, Jia Z, Sunnemark D, et al. Identification and in vitro characterization of C05-01, a PBB3 derivative with improved affinity for alpha-synuclein. Brain Res. 2020;1749:147131.

131. Ryan P, Xu M, Jahan K, Davey AK, Bharatam PV, Anoopkumar-Dukie S, et al. Novel Furan-2-yl-1H-pyrazoles Possess Inhibitory Activity against alpha-Synuclein Aggregation. ACS Chem Neurosci. 2020;11(15):2303-15.

132. Verdurand M, Levigoureux E, Lancelot S, Zeinyeh W, Billard T, Quadrio I, et al. Amyloid-Beta Radiotracer [(18)F]BF-227 Does Not Bind to Cytoplasmic Glial Inclusions of Postmortem Multiple System Atrophy Brain Tissue. Contrast Media Mol Imaging. 2018;2018:9165458.

133. Verdurand M, Levigoureux E, Zeinyeh W, Berthier L, Mendjel-Herda M, Cadarossanesaib F, et al. In Silico, in Vitro, and in Vivo Evaluation of New Candidates for alpha-Synuclein PET Imaging. Mol Pharm. 2018;15(8):3153-66.

134. Watanabe H, Ariyoshi T, Ozaki A, Ihara M, Ono M, Saji H. Synthesis and biological evaluation of novel radioiodinated benzimidazole derivatives for imaging alpha-synuclein aggregates. Bioorg Med Chem. 2017;25(24):6398-403.

135. Watanabe H, Ono M, Ariyoshi T, Katayanagi R, Saji H. Novel Benzothiazole Derivatives as Fluorescent Probes for Detection of beta-Amyloid and alpha-Synuclein Aggregates. ACS Chem Neurosci. 2017;8(8):1656-62.

136. Xiang J, Tao Y, Xia Y, Luo S, Zhao Q, Li B, et al. Development of an alpha-synuclein positron emission tomography tracer for imaging synucleinopathies. Cell. 2023;186(16):3350-67 e19.

137. Xu M, Loa-Kum-Cheung W, Zhang H, Quinn RJ, Mellick GD. Identification of a New alpha-Synuclein Aggregation Inhibitor via Mass Spectrometry Based Screening. ACS Chem Neurosci. 2019;10(6):2683-91.

138. Yue X, Dhavale DD, Li J, Luo Z, Liu J, Yang H, et al. Design, synthesis, and in vitro evaluation of quinolinyl analogues for alpha-synuclein aggregation. Bioorg Med Chem Lett. 2018;28(6):1011-9.

139. Zhang X, Jin H, Padakanti PK, Li J, Yang H, Fan J, et al. Radiosynthesis and in Vivo Evaluation of Two PET Radioligands for Imaging alpha-Synuclein. Appl Sci (Basel). 2014;4(1):66-78.

140. Akasaka T, Watanabe H, Kaide S, Iikuni S, Hasegawa M, Ono M. Synthesis and evaluation of novel radioiodinated phenylbenzofuranone derivatives as alpha-synuclein imaging probes. Bioorg Med Chem Lett. 2022;64:128679.

141. Kaide S, Watanabe H, Iikuni S, Hasegawa M, Itoh K, Ono M. Chalcone Analogue as New Candidate for Selective Detection of alpha-Synuclein Pathology. ACS Chem Neurosci. 2022;13(1):16-26.

142. Smith R, Capotosti F, Schain M, Ohlsson T, Vokali E, Molette J, et al. The α-synuclein PET tracer [18F] ACI-12589 distinguishes multiple system atrophy from other neurodegenerative diseases. Nature Communications. 2023;14(1):6750.

143. Strohaker T, Jung BC, Liou SH, Fernandez CO, Riedel D, Becker S, et al. Structural heterogeneity of alpha-synuclein fibrils amplified from patient brain extracts. Nat Commun. 2019;10(1):5535.

144. Fitzpatrick AWP, Falcon B, He S, Murzin AG, Murshudov G, Garringer HJ, et al. Cryo-EM structures of tau filaments from Alzheimer's disease. Nature. 2017;547(7662):185-90.

145. Falcon B, Zhang W, Murzin AG, Murshudov G, Garringer HJ, Vidal R, et al. Structures of filaments from Pick's disease reveal a novel tau protein fold. Nature. 2018;561(7721):137-40.

146. Falcon B, Zivanov J, Zhang W, Murzin AG, Garringer HJ, Vidal R, et al. Novel tau filament fold in chronic traumatic encephalopathy encloses hydrophobic molecules. Nature. 2019;568(7752):420-3.

147. Zhang W, Falcon B, Murzin AG, Fan J, Crowther RA, Goedert M, et al. Heparin-induced tau filaments are polymorphic and differ from those in Alzheimer's and Pick's diseases. Elife. 2019;8.

148. Breydo L, Uversky VN. Structural, morphological, and functional diversity of amyloid oligomers. FEBS Lett. 2015;589(19 Pt A):2640-8.

149. Flores-Fernandez JM, Rathod V, Wille H. Comparing the Folds of Prions and Other Pathogenic Amyloids. Pathogens. 2018;7(2).

150. Leung CS, Leung SS, Tirado-Rives J, Jorgensen WL. Methyl effects on protein-ligand binding. J Med Chem. 2012;55(9):4489-500.

151. Judenhofer MS, Wehrl HF, Newport DF, Catana C, Siegel SB, Becker M, et al. Simultaneous PET-MRI: a new approach for functional and morphological imaging. Nat Med. 2008;14(4):459-65.

152. Badhwar A, Tam A, Dansereau C, Orban P, Hoffstaedter F, Bellec P. Resting-state network dysfunction in Alzheimer's disease: A systematic review and meta-analysis. Alzheimers Dement (Amst). 2017;8:73-85.

153. Bassett DS, Bullmore ET. Human brain networks in health and disease. Curr Opin Neurol. 2009;22(4):340-7.

154. Fischer K, Sossi V, Schmid A, Thunemann M, Maier FC, Judenhofer MS, et al. Noninvasive nuclear imaging enables the in vivo quantification of striatal dopamine receptor expression and raclopride affinity in mice. J Nucl Med. 2011;52(7):1133-41.

155. Alexoff DL, Vaska P, Marsteller D, Gerasimov T, Li J, Logan J, et al. Reproducibility of 11C-raclopride binding in the rat brain measured with the microPET R4: effects of scatter correction and tracer specific activity. J Nucl Med. 2003;44(5):815-22.

156. Farde L, Hall H, Pauli S, Halldin C. Variability in D2-dopamine receptor density and affinity: a PET study with [11C]raclopride in man. Synapse. 1995;20(3):200-8.

157. Volkow ND, Fowler JS, Wang GJ, Dewey SL, Schlyer D, MacGregor R, et al. Reproducibility of repeated measures of carbon-11-raclopride binding in the human brain. J Nucl Med. 1993;34(4):609-13.

158. Hietala J, Nagren K, Lehikoinen P, Ruotsalainen U, Syvalahti E. Measurement of striatal D2 dopamine receptor density and affinity with [11C]-raclopride in vivo: a test-retest analysis. J Cereb Blood Flow Metab. 1999;19(2):210-7.

159. Alakurtti K, Johansson JJ, Joutsa J, Laine M, Backman L, Nyberg L, et al. Long-term test-retest reliability of striatal and extrastriatal dopamine D2/3 receptor binding: study with [(11)C]raclopride and high-resolution PET. J Cereb Blood Flow Metab. 2015;35(7):1199-205.

160. Karalija N, Jonassson L, Johansson J, Papenberg G, Salami A, Andersson M, et al. High long-term test-retest reliability for extrastriatal (11)C-raclopride binding in healthy older adults. J Cereb Blood Flow Metab. 2020;40(9):1859-68.

161. Shehzad Z, Kelly AM, Reiss PT, Gee DG, Gotimer K, Uddin LQ, et al. The resting brain: unconstrained yet reliable. Cereb Cortex. 2009;19(10):2209-29.

162. Thomason ME, Dennis EL, Joshi AA, Joshi SH, Dinov ID, Chang C, et al. Resting-state fMRI can reliably map neural networks in children. Neuroimage. 2011;55(1):165-75.

163. Grandjean J, Desrosiers-Gregoire G, Anckaerts C, Angeles-Valdez D, Ayad F, Barriere DA, et al. A consensus protocol for functional connectivity analysis in the rat brain. Nat Neurosci. 2023;26(4):673-81.

164. Blautzik J, Keeser D, Berman A, Paolini M, Kirsch V, Mueller S, et al. Long-term test-retest reliability of resting-state networks in healthy elderly subjects and with amnestic mild cognitive impairment patients. J Alzheimers Dis. 2013;34(3):741-54.

165. Noble S, Spann MN, Tokoglu F, Shen X, Constable RT, Scheinost D. Influences on the Test-Retest Reliability of Functional Connectivity MRI and its Relationship with Behavioral Utility. Cereb Cortex. 2017;27(11):5415-29.

166. Chen B, Xu T, Zhou C, Wang L, Yang N, Wang Z, et al. Individual Variability and Test-Retest Reliability Revealed by Ten Repeated Resting-State Brain Scans over One Month. PLoS One. 2015;10(12):e0144963.

167. Shah LM, Cramer JA, Ferguson MA, Birn RM, Anderson JS. Reliability and reproducibility of individual differences in functional connectivity acquired during task and resting state. Brain Behav. 2016;6(5):e00456.

168. Song J, Desphande AS, Meier TB, Tudorascu DL, Vergun S, Nair VA, et al. Age-related differences in test-retest reliability in resting-state brain functional connectivity. PLoS One. 2012;7(12):e49847.

169. Birn RM. The role of physiological noise in resting-state functional connectivity. Neuroimage. 2012;62(2):864-70.

170. Yan CG, Cheung B, Kelly C, Colcombe S, Craddock RC, Di Martino A, et al. A comprehensive assessment of regional variation in the impact of head micromovements on functional connectomics. Neuroimage. 2013;76:183-201.

171. Zuo XN, Xu T, Jiang L, Yang Z, Cao XY, He Y, et al. Toward reliable characterization of functional homogeneity in the human brain: preprocessing, scan duration, imaging resolution and computational space. Neuroimage. 2013;65:374-86.

172. Parkes L, Fulcher B, Yucel M, Fornito A. An evaluation of the efficacy, reliability, and sensitivity of motion correction strategies for resting-state functional MRI. Neuroimage. 2018;171:415-36.

173. Shirer WR, Jiang H, Price CM, Ng B, Greicius MD. Optimization of rs-fMRI Preprocessing for Enhanced Signal-Noise Separation, Test-Retest Reliability, and Group Discrimination. Neuroimage. 2015;117:67-79.

174. Carson RE, Breier A, de Bartolomeis A, Saunders RC, Su TP, Schmall B, et al. Quantification of amphetamine-induced changes in [11C]raclopride binding with continuous infusion. J Cereb Blood Flow Metab. 1997;17(4):437-47.

175. Houston GC, Hume SP, Hirani E, Goggi JL, Grasby PM. Temporal characterisation of amphetamine-induced dopamine release assessed with [11C]raclopride in anaesthetised rodents. Synapse. 2004;51(3):206-12.

176. Moulin-Sallanon M, Charnay Y, Ginovart N, Perret P, Lanfumey L, Hamon M, et al. Acute and chronic effects of citalopram on 5-HT1A receptor-labeling by [18F]MPPF and -coupling to receptors-G proteins. Synapse. 2009;63(2):106-16.

177. Finnema SJ, Stepanov V, Ettrup A, Nakao R, Amini N, Svedberg M, et al. Characterization of [(11)C]Cimbi-36 as an agonist PET radioligand for the 5-HT(2A) and 5-HT(2C) receptors in the nonhuman primate brain. Neuroimage. 2014;84:342-53.

178. Landau AM, Doudet DJ, Jakobsen S. Amphetamine challenge decreases yohimbine binding to alpha2 adrenoceptors in Landrace pig brain. Psychopharmacology (Berl). 2012;222(1):155-63.

179. Phan JA, Landau AM, Wong DF, Jakobsen S, Nahimi A, Doudet DJ, et al. Quantification of [(11)C]yohimbine binding to alpha2 adrenoceptors in rat brain in vivo. J Cereb Blood Flow Metab. 2015;35(3):501-11.

180. Hoekzema E, Herance R, Rojas S, Pareto D, Abad S, Jimenez X, et al. The effects of aging on dopaminergic neurotransmission: a microPET study of [11C]-raclopride binding in the aged rodent brain. Neuroscience. 2010;171(4):1283-6.

181. Arakawa R, Farde L, Matsumoto J, Kanegawa N, Yakushev I, Yang KC, et al. Potential Effect of Prolonged Sevoflurane Anesthesia on the Kinetics of [(11)C]Raclopride in Non-human Primates. Mol Imaging Biol. 2018;20(2):183-7.

182. Finnema SJ, Halldin C, Bang-Andersen B, Gulyas B, Bundgaard C, Wikstrom HV, et al. Dopamine D(2/3) receptor occupancy of apomorphine in the nonhuman primate brain--a comparative PET study with [11C]raclopride and [11C]MNPA. Synapse. 2009;63(5):378-89.

183. Freiburghaus T, Svensson JE, Matheson GJ, Plaven-Sigray P, Lundberg J, Farde L, et al. Low convergent validity of [(11)C]raclopride binding in extrastriatal brain regions: A PET study of within-subject correlations with [(11)C]FLB 457. Neuroimage. 2021;226:117523.

184. Svensson JE, Schain M, Plaven-Sigray P, Cervenka S, Tiger M, Nord M, et al. Validity and reliability of extrastriatal [(11)C]raclopride binding quantification in the living human brain. Neuroimage. 2019;202:116143.

185. Lippert RN, Cremer AL, Edwin Thanarajah S, Korn C, Jahans-Price T, Burgeno LM, et al. Time-dependent assessment of stimulus-evoked regional dopamine release. Nat Commun. 2019;10(1):336.

186. Ungerstedt U. 6-Hydroxy-dopamine induced degeneration of central monoamine neurons. Eur J Pharmacol. 1968;5(1):107-10.

187. Perese DA, Ulman J, Viola J, Ewing SE, Bankiewicz KS. A 6-hydroxydopamine-induced selective parkinsonian rat model. Brain Res. 1989;494(2):285-93.

188. Hume SP, Opacka-Juffry J, Myers R, Ahier RG, Ashworth S, Brooks DJ, et al. Effect of L-dopa and 6-hydroxydopamine lesioning on [11C]raclopride binding in rat striatum, quantified using PET. Synapse. 1995;21(1):45-53.

189. Nguyen TV, Brownell AL, Iris Chen YC, Livni E, Coyle JT, Rosen BR, et al. Detection of the effects of dopamine receptor supersensitivity using pharmacological MRI and correlations with PET. Synapse. 2000;36(1):57-65.

190. Bunney BS, Aghajanian GK. The precise localization of nigral afferents in the rat as determined by a retrograde tracing technique. Brain Res. 1976;117(3):423-35.

191. Cole DM, Beckmann CF, Oei NY, Both S, van Gerven JM, Rombouts SA. Differential and distributed effects of dopamine neuromodulations on resting-state network connectivity. Neuroimage. 2013;78:59-67.

192. Honey GD, Suckling J, Zelaya F, Long C, Routledge C, Jackson S, et al. Dopaminergic drug effects on physiological connectivity in a human cortico-striato-thalamic system. Brain. 2003;126(Pt 8):1767-81.

193. Bjorklund A, Dunnett SB. Dopamine neuron systems in the brain: an update. Trends Neurosci. 2007;30(5):194-202.

194. Paasonen J, Salo RA, Shatillo A, Forsberg MM, Narvainen J, Huttunen JK, et al. Comparison of seven different anesthesia protocols for nicotine pharmacologic magnetic resonance imaging in rat. Eur Neuropsychopharmacol. 2016;26(3):518-31.

195. Williams KA, Magnuson M, Majeed W, LaConte SM, Peltier SJ, Hu X, et al. Comparison of alpha-chloralose, medetomidine and isoflurane anesthesia for functional connectivity mapping in the rat. Magn Reson Imaging. 2010;28(7):995-1003.

196. Paasonen J, Stenroos P, Salo RA, Kiviniemi V, Grohn O. Functional connectivity under six anesthesia protocols and the awake condition in rat brain. Neuroimage. 2018;172:9-20.

197. Hutchison RM, Hutchison M, Manning KY, Menon RS, Everling S. Isoflurane induces dose-dependent alterations in the cortical connectivity profiles and dynamic properties of the brain's functional architecture. Hum Brain Mapp. 2014;35(12):5754-75.

198. Jonckers E, Delgado y Palacios R, Shah D, Guglielmetti C, Verhoye M, Van der Linden A. Different anesthesia regimes modulate the functional connectivity outcome in mice. Magnetic resonance in medicine. 2014;72(4):1103-12.

199. Wang K, van Meer MP, van der Marel K, van der Toorn A, Xu L, Liu Y, et al. Temporal scaling properties and spatial synchronization of spontaneous blood oxygenation level-dependent (BOLD) signal fluctuations in rat sensorimotor network at different levels of isoflurane anesthesia. NMR Biomed. 2011;24(1):61-7.

200. Nieoullon A, Dusticier N. Effects of alpha-chloralose on the activity of the nigrostriatal dopaminergic system in the cat. Eur J Pharmacol. 1980;65(4):403-10.

201. Choi JK, Chen YI, Hamel E, Jenkins BG. Brain hemodynamic changes mediated by dopamine receptors: Role of the cerebral microvasculature in dopamine-mediated neurovascular coupling. Neuroimage. 2006;30(3):700-12.

202. Iversen L. Speed, ecstasy, ritalin: the science of amphetamines: Oxford: Oxford University Press; 2006.

203. Ren J, Xu H, Choi JK, Jenkins BG, Chen YI. Dopaminergic response to graded dopamine concentration elicited by four amphetamine doses. Synapse. 2009;63(9):764-72.

204. Schrantee A, Ferguson B, Stoffers D, Booij J, Rombouts S, Reneman L. Effects of dexamphetamine-induced dopamine release on resting-state network connectivity in recreational amphetamine users and healthy controls. Brain Imaging Behav. 2016;10(2):548-58.

205. Schwarz AJ, Gozzi A, Reese T, Bifone A. In vivo mapping of functional connectivity in neurotransmitter systems using pharmacological MRI. Neuroimage. 2007;34(4):1627-36.

206. Schwarz AJ, Gozzi A, Reese T, Bifone A. Functional connectivity in the pharmacologically activated brain: resolving networks of correlated responses to d-amphetamine. Magnetic resonance in medicine. 2007;57(4):704-13.

207. Dixon AL, Prior M, Morris PM, Shah YB, Joseph MH, Young AM. Dopamine antagonist modulation of amphetamine response as detected using pharmacological MRI. Neuropharmacology. 2005;48(2):236-45.

208. Chen YC, Galpern WR, Brownell AL, Matthews RT, Bogdanov M, Isacson O, et al. Detection of dopaminergic neurotransmitter activity using pharmacologic MRI: correlation with PET, microdialysis, and behavioral data. Magnetic resonance in medicine. 1997;38(3):389-98.

209. Turner M. The Treatment of Narcolepsy With Amphetamine-Based Stimulant Medications: A Call for Better Understanding. J Clin Sleep Med. 2019;15(5):803-5.

210. Stotz G, Woggon B, Angst J. Psychostimulants in the therapy of treatment-resistant depression Review of the literature and findings from a retrospective study in 65 depressed patients. Dialogues Clin Neurosci. 1999;1(3):165-74.

211. Kolar D, Keller A, Golfinopoulos M, Cumyn L, Syer C, Hechtman L. Treatment of adults with attention-deficit/hyperactivity disorder. Neuropsychiatr Dis Treat. 2008;4(1):107-21.

212. Heal DJ, Smith SL, Gosden J, Nutt DJ. Amphetamine, past and present--a pharmacological and clinical perspective. J Psychopharmacol. 2013;27(6):479-96.

213. Fassbender C, Zhang H, Buzy WM, Cortes CR, Mizuiri D, Beckett L, et al. A lack of default network suppression is linked to increased distractibility in ADHD. Brain Res. 2009;1273:114-28.

214. Silberstein RB, Pipingas A, Farrow M, Levy F, Stough CK. Dopaminergic modulation of default mode network brain functional connectivity in attention deficit hyperactivity disorder. Brain Behav. 2016;6(12):e00582.

215. Scheidegger M, Walter M, Lehmann M, Metzger C, Grimm S, Boeker H, et al. Ketamine decreases resting state functional network connectivity in healthy subjects: implications for antidepressant drug action. PLoS One. 2012;7(9):e44799.

216. Chen YI, Brownell AL, Galpern W, Isacson O, Bogdanov M, Beal MF, et al. Detection of dopaminergic cell loss and neural transplantation using pharmacological MRI, PET and behavioral assessment. Neuroreport. 1999;10(14):2881-6.

217. Monnot C, Zhang X, Nikkhou-Aski S, Damberg P, Svenningsson P. Asymmetric dopaminergic degeneration and levodopa alter functional corticostriatal connectivity bilaterally in experimental parkinsonism. Exp Neurol. 2017;292:11-20.

218. Westphal R, Simmons C, Mesquita MB, Wood TC, Williams SC, Vernon AC, et al. Characterization of the resting-state brain network topology in the 6-hydroxydopamine rat model of Parkinson's disease. PLoS One. 2017;12(3):e0172394.

219. Perlbarg V, Lambert J, Butler B, Felfli M, Valabregue R, Privat AL, et al. Alterations of the nigrostriatal pathway in a 6-OHDA rat model of Parkinson's disease evaluated with multimodal MRI. PLoS One. 2018;13(9):e0202597.

220. Albin RL, Young AB, Penney JB. The functional anatomy of basal ganglia disorders. Trends Neurosci. 1989;12(10):366-75.

221. Monchi O, Petrides M, Mejia-Constain B, Strafella AP. Cortical activity in Parkinson's disease during executive processing depends on striatal involvement. Brain. 2007;130(Pt 1):233-44.

222. Tessitore A, Hariri AR, Fera F, Smith WG, Chase TN, Hyde TM, et al. Dopamine modulates the response of the human amygdala: a study in Parkinson's disease. J Neurosci. 2002;22(20):9099-103.

Acknowledgments

First of all, I would like to thank Prof. Dr. Bernd Pichler for making it possible for me to do my doctoral thesis at the Werner Siemens Imaging Center in Tübingen.

Then, I want to extend my thanks to my first supervisor, Prof. Dr. Kristina Herfert. Her dedication to the pursuit of knowledge and her commitment to excellence have been a constant source of inspiration for me. I am grateful for her invaluable guidance and profound insights that significantly shaped the course of my research. Her expertise and critical feedback were enhancing the quality of this work.

I also extend my sincere appreciation to my second supervisor, Prof. Dr. Steffen Hage, for his supervision and willingness to provide the second opinion for this dissertation.

Furthermore, I would like to acknowledge the participants and individuals who generously shared their time and knowledge, without whom this research would not have been possible. Here I would like to mention Dr. Julia Mannheim, Sabrina Haas and Dr. Tudor Ionescu for their support and encouragement throughout this time. Their unwavering faith in my abilities provided the motivation I needed to persist through the challenges and triumphs of this academic endeavor.

Then, I would like to express my gratitude to the technical assistants of the Werner Siemens Imaging Center for their assistance and resources that were vital to the successful completion of this research: Linda Schramm, Maren Harant, Natalie Hermann, Dennis Haupt, Elena Kimmerle, Johannes Kinzler, und Ramona Stremme.

I would like to express my deep gratitude and appreciation to my mother who has supported me throughout my dissertation journey. Without you, this would have not been possible.

This dissertation is a product of collective effort and would not have been realized without the guidance, collaboration, and support of the aforementioned individuals. I am truly grateful for their contributions to my academic and personal growth.

Declaration of Authorship

„Hiermit erkläre ich, Laura Kübler, an Eides statt, dass ich die vorliegende Doktorarbeit selbstständig verfasst und keine anderen als die angegebenen Quellen und Hilfsmittel benutzt habe.“

Ort, Datum, Unterschrift